On Ultra-High Temperature Metamorphism in the Mid–Lower Crust

Kristin Marie Dorfler

Dissertation submitted to the faculty of the Virginia Polytechnic Institute and State University in partial fulfillment of the requirements for the degree of

Doctor of Philosophy
In
Geosciences

Robert J. Tracy
James S. Beard
Mark J. Caddick
Gary R. Pickrell
Nancy L. Ross

May 2, 2014
Blacksburg, VA

Keywords: Cortlandt Complex, emery, norite, partial melting, pelitic assimilation

On Ultra-High Temperature Metamorphism in the Mid–Lower Crust

Kristin Marie Dorfler

ABSTRACT

The Cortlandt Complex in New York is a composite intrusion of six mafic plutons and contains pelitic xenoliths that experienced extensive interaction with Mg-rich basaltic melt. The complex is an excellent natural example of ultra-high temperature (UHT) metamorphic processes and country rock–magma interaction due to mappable units of hybrid igneous rocks and the presence of large, partially melted, pelitic 'emery' xenoliths. Previous attempts to understand the formation of the UHT xenoliths in the Cortlandt have provided the petrologic foundation for more rigorous thermodynamic modeling to determine the petrogenesis of these materials and to ultimately contribute to the understanding of UHT metamorphism in the Earth's crust.

This work focuses on the development of hybrid monzonorites and emery at Salt Hill, located in the southeasternmost edge of the Cortlandt Complex. First, a thermobarometric study focuses on the *P–T* conditions of the country rock into which the Complex intruded. Pelitic schists from contact aureoles around a nearby pluton chemically and chronologically related to the complex, record high-*P* (~ 0.9 GPa, ~ 32 km depth) crustal conditions during pluton emplacement. This is interpreted to reflect loading due to the emplacement of Taconic allochthons during the waning stages of regional metamorphism before emplacement of the plutons. The second study uses thermodynamic heating calculations of pelitic schist to determine the production of norite and emery. Modeling results produce (i) an initial melt that produces a monzonorite composition when mixed with a mafic melt, (ii) a high-*T* melt that is texturally and compositionally homologous with quartzofeldspathic veins retained in the emery, and (iii) a residual mineral assemblage that, when oxidized, closely resembles the emery assemblage.

Finally, focus is given to understanding the relationship between norite and emery and reflection on the mineralogy and structure of the lower crust–mantle boundary. Density calculations of the emery estimate values comparable to mantle densities, implying that rare exposure of UHT assemblages may be due to the fact the material stays at lower crustal (upper mantle?) depths. Therefore, the less-rare norite and other hybrid igneous rock occurrences may be the traces of deep, unexposed, UHT metamorphic assemblages.

Dedication

This is dedicated to Norman Levi Bowen for giving me silent encouragement before I even knew who he was.

Acknowledgements

There are too many friends and colleagues who have supported and encouraged me over the years, from elementary school up to my defense and even my future colleagues at Oberlin. Therefore I will only have space to name a few people who have seen me at my best and my absolute worst.

First, I want to thank my immediate family, Joe, Lecia, Joey, and Katie Dorfler. Thank you for reminding me that, despite all my peaks and valleys, I'm still your little Rit.

Second, thank you, Brent Owens, for encouraging me to continue my enthusiasm for petrology at Virginia Tech and for being a wonderful mentor since my time at William and Mary. I look forward to working with you in the future.

Third, a special thank you to my primary adviser, Bob Tracy. You've been patient with me and I consider you a very inspirational man. I will always look up to you.

Fourth, I want to thank my adviser and friend, Mark Caddick. You have been helpful and encouraging in several facets in my life and I am grateful you came to Virginia Tech.

Finally, my friends and office mates over the years, Sarah Timm, Liz Krukowski, Victor Guevara, Kristen McCall, and Jen Gorce. You've been there for me even (especially) when I didn't deserve your kindness.

Although there are many more who have not been named, they have certainly not been overlooked.

Attributions

Chapter 2 was published as "Dorfler, K.M., Tracy, R.J., and Caddick, M.J., 2014, Late Stage Orogenic Loading Revealed by Contact Metamorphism in the Northern Appalachians, New York. *Journal of Metamorphic Geology* 32, 113-132". Copyrite permission has been given by John Wiley and Sons to reprint this article. KM Dorfler was responsible for final thermobarometric calculations, drafting all figures and writing the manuscript. RJ Tracy was responsible for project conception, collection of initial microprobe analysis and chemical images, initial thermobarometric calculations, and contributed significantly to petrographic interpretation. MJ Caddick was responsible for assisting in thermobarometric calculations, petrographic and tectonic interpretation. RJ Tracy and MJ Caddick helped clarify the text and figures.

Chapter 3, "Thermodynamic Modeling of Crustal Melting Using Xenolith Analogs from the Cortlandt Complex, New York, USA" will be submitted to *Journal of Petrology* for publication. KM Dorfler was responsible for computer modeling, petrographic and textural interpretation, drafting all figures and writing the manuscript. MJ Caddick developed the fractional crystallization code, assisted in interpreting modeling results and mixing calculations, heat conduction modeling, and clarified portions of the text and figures. RJ Tracy assisted with microprobe data, petrographic interpretations, and clarification of text.

Chapter 4, "The Missing Corundum Conundrum: Is the Presence of Hybrid Rocks Evidence for UHT Metamorphism?" may be submitted to *Geology* for publication. KM Dorfler was responsible for density calculations, writing the manuscript and drafting all figures. JS Beard and RJ Tracy provided stimulus and guidance for project conception and interpretation. MJ Caddick provided support for calculations and interpretation.

Table of Contents

List of Figures

List of Tables

Chapter 1

Introduction

Ultra-high temperature (UHT) metamorphism in the Earth's crust is an important and still-developing topic in metamorphic petrology. UHT processes occur in the crust when thermal conditions reach $T \geq 900$ ˚C and therefore represents one of the most extreme types of metamorphism. However, exposure of samples with UHT metamorphic assemblages such as sapphirine + quartz (e.g., Bose *et al.*, 2000, Caporuscio & Morse, 1978, Dasgupta & Ehl, 1993, Gnos & Kurz, 1994, Guiraud *et al.*, 1996, Podlesskii & Kurdyukov, 1992, Tsunogae & Santosh, 2006), orthopyroxene + sillimanite ± quartz (e.g., Bertrand *et al.*, 1992, Dasgupta *et al.*, 1995, Grew, 1980, Harley & Hensen, 1990, Perchuk *et al.*, 1985, Sarkar *et al.*, 2003), or spinel + quartz (e.g., Caporuscio & Morse, 1978, Clarke *et al.*, 1989, Dasgupta *et al.*, 1995, Vielzeuf, 1983, Waters, 1991), is rare in nature and generally only occurs in Mg-rich pelitic compositions (Ague *et al.*, 2013, Kelsey, 2008).

At the onset of this research in 2009, there existed a little over forty known localities of UHT metamorphism (Kelsey, 2008), most of which occur within ancient cratons like the Napier Complex in Antarctica (e.g., Ellis, 1980, Harley, 1985, Harley, 1986, Harley, 1987, Sandiford & Powell, 1986) or in more recent mobile belts like in the Eastern Ghats Province in India (e.g., Bose *et al.*, 2000, Dasgupta & Ehl, 1993, Sarkar *et al.*, 2003, Sengupta *et al.*, 1999). Regional UHT occurrences are rare in the United States and have been documented in only two locations: Winding Stair Gap, NC (Eckert *et al.*, 1989, El-Shazly *et al.*, 2011) and the Merrimack synclinorium, CT (Ague *et al.*, 2013). Although UHT metamorphism is most common in regional terranes worldwide, they can rarely occur as xenoliths in mafic intrusions, such as the aluminous xenoliths at the Cortlandt Complex, New York. It is likely that UHT metamorphism is much more widespread than is currently recognized and, considering the temperature, pressure and bulk-rock chemistry associated with UHT metamorphism, most of the Earth's lower crust may be composed of UHT assemblages. Therefore, UHT metamorphism has important implications for the development of the lower crust and crust–mantle interaction. The following chapters focus on the formation of UHT aluminous xenoliths in the Cortlandt Complex, the

complex interactions between pelitic rocks and mafic (mantle-derived) melt, and the production of hybrid igneous rocks. The processes that took place between the pelitic xenoliths and mafic melt is analogous to UHT processes that occur on a regional scale, however the relatively small scale (10s of meters as opposed to 100s of meters to kilometers) of this locality and the availability of the protoliths and products of each rock type makes the Cortlandt an ideal 'natural laboratory' to study UHT metamorphism.

Many aspects of the Cortlandt Complex such as the chemical differences between each igneous body, the formations exposed within the complex (e.g. emery), and the overall shape of the series has been studied since the mid 19th-century. One of the most interesting aspects of the Cortlandt is that many of the earlier studies on the series were published by some of the most influential figures in geology. Written descriptions of the Cortlandt Complex from many notable historical figures date as far back to the discovery of the Hudson River in the early 17th century. The first mention of the Cortlandt Complex (specifically emery) dates back to Henry Hudson's third voyage (1608–1609), in which he records trading with Native Americans for a hard stone that can cut steel or iron (Chadwick, 2007, Rogers, 1911).

In the late 19th century, J.D. Dana published a two-series paper on the rocks of Westchester County and is credited with naming the series the Cortlandt (Dana, 1879, Dana, 1880, Dana, 1881, Rogers, 1911). He continued to work in collaboration with other geologists up through 1884 and was the first to establish the Complex as an intrusive suite of rocks emplaced after the formation of the limestone, schist and granite that constitutes the majority of the Manhattan Prong (Dana, 1884, Van Hise & Leith, 1909). G.H. Williams, the first professor to introduce American students to microscopical petrography (Iddings, 1894), recognized the mineralogical and petrographical significance of the Cortlandt. He contributed a five-piece series on the Cortlandt Complex and contact metamorphism associated with it (Williams, 1886, Williams, 1887, Williams, 1888a, Williams, 1888b, Williams, 1888c) and, in particular, wrote in extensive detail on the presence of corundum in the emery at Salt Hill. G.S. Rogers' (1911) manuscript on the geology of the Cortlandt was the first to recognize the importance of the series with respect to magmatic differentiation and included petrographically descriptive analyses of the series with bulk-rock chemical analyses of over a dozen different rock types near the complex. His analyses were referenced later in N.L. Bowen's *The Evolution of the Igneous Rocks* (1928) and used in the forward modeling calculations in chapter three. Norman L. Bowen

recognized the significance of the Cortlandt series in that it had the potential to provide insight on topics such as crustal assimilation and fractional crystallization of mafic magma. After publishing his Reaction Series in the Spring of 1922, he published a manuscript on the behavior of inclusions in igneous magmas in which he specifically describes the effects of assimilation of pelites in a basaltic melt, referencing the Cortlandt Series as an ideal occurrence to study the metamorphic affects (Bowen, 1922).

In chapter two, *"Late Stage Orogenic Loading Revealed by Contact Metamorphism in the Northern Appalachians, New York"*, which was accepted for publication in the Journal of Metamorphic Geology in January 2014, we investigate the regional *P–T* conditions of the Manhattan Prong at the time of pluton emplacement in the late-Ordovician, early-Silurian. Thermobarometric calculations were performed using contact-metamorphosed pelitic schists from the aureole of the Croton Falls pluton, a nearby mafic pluton that is compositionally and temporally related to the Cortlandt Complex. Garnet porphyroblasts from one sample retained earlier regional metamorphic assemblages (and peak *P–T* conditions) in the garnet cores whilst mineral assemblages (and *P–T* conditions) associated with contact metamorphism are preserved in the garnet rims and matrix assemblage. Values from the interior assemblages match well with results from published studies on *P–T* conditions of regional metamorphism in the area. More importantly, high pressures (~ 0.9 GPa) were deduced from the matrix (contact metamorphosed) assemblage. We interpret this to reflect loading due to the emplacement of Taconic allochthons in the northern Appalachians during the waning stages of regional metamorphism and before contact metamorphism. Therefore, the UHT metamorphosed samples from the Cortlandt Complex formed under conditions of high-*T and* high-*P*.

In chapter three, *"Thermodynamic Modeling of Crustal Melting Using Xenolith Analogs from the Cortlandt Complex, New York, USA"*, we focus on the production of the Salt Hill 'emery' xenoliths by simulating the heating and partial melting of a pelite using advanced equilibrium thermodynamic modeling techniques. Using an average composition of the Manhattan Schist and *P–T* conditions as determined in Chapter two, we simulate the heating, melting, crystallization and oxidation of the xenolith samples and produce a calculated bulk-rock assemblage that reflects the textures and compositions in the natural samples. Additionally, we simulate the formation of a hybrid igneous rock using mixing calculations and successfully

produce a bulk-rock chemistry that is homologous to the monzonorite samples found nearby the xenoliths.

Finally, chapter four reflects on the connection between hybrid igneous rocks and UHT metamorphism and pelitic assimilation at Salt Hill. Although UHT metamorphic assemblages in contact settings are incredibly rare, hybrid norites and diorites are commonly associated with crustal assimilation and partial melting by mafic melts. The presence of norite in certain metamorphic settings may be direct evidence of extensive pelite assimilation and production of 'emery' residuum. Chapter four *"The Emery–Norite Conundrum: Is the Presence of Hybrid Igneous Rocks Evidence for UHT Metamorphism?"* uses density values of the UHT products from chapter three to investigate the possibility that emery may be a very common product of mafic melt–pelitic rock interaction and may be a major constituent in the lower crust.

1.1 References

Ague, J. J., Eckert, J., J.O., Chu, X., Baxter, E. F. & Chamberlain, C. P. (2013). Discovery of ultrahigh-temperature metamorphism in the Acadian orogen, Connecticut, USA. *Geology (Boulder)*.

Bertrand, P., Ouzegane, K. & Kienast, J.-R. (1992). *P–T–X* relationships in the Precambrian Al-Mg-rich granulites from In Ouzzal, Hoggar, Algeria. *Journal of Metamorphic Geology* **10**, 17-31.

Bose, S., Fukuoka, M., Sengupta, P. & Dasgupta, S. (2000). Evolution of high-Mg–Al granulites from Sunkarametta, Eastern Ghats, India: evidence for a lower crustal heatin–cooling trajectory. *Journal of Metamorphic Geology* **18**, 223-240.

Bowen, N. L. (1922). The behavior of inclusions in igneous magmas. *The Journal of Geology* **30**, 513-569.

Bowen, N. L. (1928). *The evolution of the igneous rocks*. Princeton: Princeton University Press.

Caporuscio, F. A. & Morse, S. A. (1978). Occurrence of sapphirine plus quartz at Peekskill, New York. *American Journal of Science (1880)* **278**, 1334-1342.

Chadwick, I. (2007). Henry Hudson's Third Voyage 1609: The New World.

Clarke, G. L., Powell, R. & Guiraud, M. (1989). Low-presure granulite facies metapelitic assemblages and corona textures from MacRobertson Land, east Antartica: the importance of Fe2O3 and TiO2 in accounting for spinel-bearing assemblages. *Journal of Metamorphic Geology* **7**, 323-335.

Dana, J. D. (1879). On the Hudson River Age of the Taconic Schists, and on the Dependent Relations of the Dutchess County and Western Connecticut Limestone belts. *American Journal of Science (1880)* **17**, 375.

Dana, J. D. (1880). On the geological relations of the limestone belts of Westchester County, New York. *American Journal of Science (1880)* **20**, 21-32.

Dana, J. D. (1881). The geological realtions of the limestone belts of Westchester County, New York. *American Journal of Science (1880)* **22**, 103-119.

Dana, J. D. (1884). Note on the Corlandt and Stony Point hornblendic and augitic rock [New York]. *American Journal of Science (1880)* **28**, 384-386.

Dasgupta, S. & Ehl, J. (1993). Reaction textures in a spinel-sapphirine granulite from the Eastern Ghats, India, and their implications. *European Journal of Mineralogy (Stuttgart)* **5**, 537-543.

Dasgupta, S., Sengupta, P., Ehl, J., Raith, M. & Bardhan, S. (1995). Reaction textures in a suite of spinel granulites from the Eastern Ghats Belt, India; evidence for polymetamorphism, a partial petrogenetic grid in the system KFMASH and the roles of ZnO and Fe_2O_3. *Journal of Petrology* **36**, 435-461.

Eckert, J., J.O., Hatcher, R. D. & Mohr, D. W. (1989). The Wayah granulite facies metamorphic core, southwestern North Carolina: High-grade culmination of Taconic metamorphism in the southern Blue Ridge. *Geological Society of America Bulletin* **101**, 1434-1447.

El-Shazly, A. K., Loehn, C. & Tracy, R. J. (2011). P-T-t evolution of granulite facies metamorphism and partial melting in the Winding Stair Gap, Central Blue Ridge, North Carolina, USA. *Journal of Metamorphic Geology*.

Ellis, D. J. (1980). Osumilite–sapphirine–quartz granulites from Enderby Land, Antarctica – *P-T* conditions of metamorphism, implications for garnet–cordierite equilibria and the evolution of the deep crust. *Contributions to Mineralogy and Petrology* **74**, 201-210.

Gnos, E. & Kurz, D. (1994). Sapphirine-quartz and sapphirine-corondum assemblages in metamorphic rocks associated with the Semail Ophiolite (United Arab Emirates). *Contributions to Mineralogy and Petrology* **116**, 398-410.

Grew, E. S. (1980). Sapphirine+quartz association from Archean rocks in Enderby Land, Antarctica. *American Mineralogist* **65**, 821-836.

Guiraud, M., Kienast, J.-R. & Rahmani, A. (1996). Petrological study of high-temperature granulites from In Ouzzal, Algeria: some implications on the phase relationships in the FMASTOCr system. *European Journal of Mineralogy (Stuttgart)* **8**, 1375-1390.

Harley, S. L. (1985). Garnet–orthopyroxene bearing granulites from Enderby Land, Antarctica: metamorphic pressure-temperature-time evolution of the Archaean Napier Complex. *Journal of Petrology* **26**, 819-856.

Harley, S. L. (1986). A sapphirine-cordierite-garnet-sillimanite granulite from Enderby Land, Antarctica – implications for FMAS petrogenetic grids in the granulite facies. *Contributions to Mineralogy and Petrology* **94**, 452-460.

Harley, S. L. (1987). A pyroxene-bearing meta-ironstone and other pyroxene–granulites from Tonagh Island, Enderby-Land Antarctica – further evidence for very high-temperature (greater-than 980-degrees-C) Archean regional metamorphism in the Napier complex. *Journal of Metamorphic Geology* **5**, 341-356.

Harley, S. L. & Hensen, B. J. (1990). Graphical analysis of *P-T-X* relations in granulite facies metapelites. In: Ashworth, J. R. & Brown, M. (eds.) *High-temperature metamorphism and crustal anatexis*. Unwin Hyman, London: Mineralogical Society of Great Britain, 19-56.

Iddings, J. P. (1894). George Huntington Williams. *The Journal of Geology* **2**, 759-767.

Kelsey, D. E. (2008). On ultrahigh-temperature crustal metamorphism. *Gondwana research* **13**, 1-29.

Perchuk, A. L., Aranovich, L. Y., Podlesskii, K. K., Lavrant'eva, I. V., Gerasimov, Y. Y., Fed'kin, V. V., Kitsul, V. I., Karsakov, L. P. & Berdnikov, N. V. (1985). Precambrian granulites of the Aldan Shield, eastern Siberia, USSR. *Journal of Metamorphic Geology* **3**, 265-310.

Podlesskii, K. K. & Kurdyukov, E. B. (1992). Sapphirine associating with quartz in Chogar and Sharyzhalgay complexes (the East Siberia). *Izvestiya Akademii Nauk Seriya Geologicheskaya* **5**, 62-67.

Rogers, G. S. (1911). Geology of the Cortlandt Series and it's Emery Deposits. *Annals New York Academy of Science* **21**, 11-86.

Sandiford, M. & Powell, R. (1986). Pyroxene exsolution in granulites from Fyfe Hills, Enderby Land, Antartica: evidence for 1000 C metamorphic temperatures in Archean continental crust. *American Mineralogist* **71**, 946–954.

Sarkar, S., Dasgupta, S. & Fukuoka, M. (2003). Petrological evolution of a suite of spinel granulites from Vizianagram, Eastern Ghats Belt, India, and genesis of sapphirine-bearing assemblages. *Journal of Metamorphic Geology* **21**, 899-913.

Sengupta, P., Sen, J., Dasgupta, S., Raith, M., Bhui, U. K. & Ehl, J. (1999). Ultra-high temperature metamorphism of metapelitic granulites from Kondapalle, Eastern Ghats Belt: implications for the Indo-Antarctic correlation. *Journal of Petrology* **40**, 1065-1087.

Tsunogae, T. & Santosh, M. (2006). Spinel–sapphirine–quartz bearing compositie inclusion within garnet from an ultrahigh-temperature pelitic granulite: implications for metamorphic history and *P–T* path. *Lithos* **92**, 524-536.

Van Hise, C. R. & Leith, C. K. (1909). Pre-Cambrian Geology of North America. In: Department of the Interior, U. (ed.): George Otis Smith.

Vielzeuf, D. (1983). The spinel and quartz associations in high grade xenoliths from Tallante (S.E. Spain) and their potential use in geothermometry and barometry. *Contributions to Mineralogy and Petrology* **82**, 301-311.

Waters, D. J. (1991). Hercynite-quartz granulites: phase relations, and implications for crustal processes. *European Journal of Mineralogy (Stuttgart)* **3**, 367-386.

Williams, G. H. (1886). The peridotites of the Cortlandt series on the Hudson River near Peekskill. *American Journal of Science (1880)* **31**, 26-31.

Williams, G. H. (1887). The norites of the 'Cortlandt Series' on the Hudson River near Peekskill, N.Y. *American Journal of Science, 3d series* **33**, 135-144.

Williams, G. H. (1888a). The contact-metamorphism produced in the adjoining mica schists and limestones by the massive rocks of the "Cortlandt Series" near Peekskill, NY. *American Journal of Science, 3d series* **36**, 254-269.

Williams, G. H. (1888b). The gabbros and diorite of the "Cortlandt series" on the Hudson River near Peekskill, N.Y. *American Journal of Science (1880)* **35**, 438-448.

Williams, G. H. (1888c). The massive rocks and contact phenomena of the Cortlandt series near Peekskill, N.Y. *Johns Hopkins University Circular* **7**, 63-65.

Chapter 2

Late Stage Orogenic Loading Revealed by Contact Metamorphism in the Northern Appalachians, New York

K.M. Dorfler, R.J. Tracy and M.J. Caddick

Department of Geosciences, Virginia Polytechnic Institute and State University, Blacksburg, VA 24061, USA

Published January 2014 in *Journal of Metamorphic Geology*, 32, 113-132

Abstract: Pelitic schists from contact aureoles surrounding mafic–ultramafic plutons in Westchester County, NY record a high-*P* (~ 0.8 GPa) high-*T* (~ 790 °C) contact overprint on a Taconic regional metamorphic assemblage (~ 0.5 GPa). The contact metamorphic assemblage of a pelitic sample in the innermost aureole of the Croton Falls pluton, a small (<10 km^2) gabbroic body, consists of quartz–plagioclase–biotite–garnet–sillimanite–ilmenite–graphite–Zn-rich Al-spinel. Both K-feldspar and muscovite are absent, and abundant biotite, plagioclase, sillimanite, quartz and ilmenite inclusions are found within subhedral garnet crystals. Unusually low bulk-rock Na and K contents imply depletion of alkalic components and silica through anatexis and melt extraction during contact heating relative to typical metapelites outside the aureole. Thermobarometry on nearby samples lacking a contact overprint yields 620–640 °C and 0.5–0.6 GPa. In the aureole sample, WDS X-ray chemical maps show distinct Ca-enriched rims on both garnet and matrix plagioclase. Furthermore, biotite inclusions within garnet have significantly higher Mg concentration than matrix biotite. Thermobarometry using GASP and Garnet–Biotite Mg–Fe exchange equilibria on inclusions and adjacent garnet host interior to the high-Ca rim zone yield $P = \sim 0.5 \pm 0.1$ GPa and $T = \sim 620 \pm 50$ °C. Pairs in the modified garnet rim zone yield $\sim 0.9 \pm 0.1$ GPa and $\sim 790 \pm 50$ °C. THERMOCALC average *P–T* calculations yield similar results for core ($\sim 0.5 \pm \sim 0.1$ GPa, $\sim 640 \pm \sim 80$ °C) and rim ($\sim 0.9 \pm \sim 0.1$ GPa, $\sim 800 \pm \sim 90$ °C) equilibria. The core assemblages are interpreted to record the *P–T* conditions of peak metamorphism during the Taconic regional event whereas the rim compositions and matrix assemblages are interpreted to record the *P–T* conditions during the contact event. The high pressures deduced for this later event are interpreted to reflect loading due to the emplacement of Taconic allochthons in the northern Appalachians during the waning stages of regional metamorphism (after *c*. 465 Ma) and before contact metamorphism (*c*. 435 Ma). In the absence of contact metamorphism-induced recrystallization, it is likely that this regional-scale loading would remain cryptic or unrecorded.

2.1 Introduction

Contact metamorphic aureoles in moderate to high-pressure regional metamorphic terranes could provide important chemical and petrologic constraints for understanding the overall geologic history and evolution of an orogen. Unmodified pre-intrusion mineral assemblages in rocks within an aureole record regional conditions preceding the contact event, whereas compositional modification of key thermobarometric minerals (e.g., garnet, biotite, plagioclase) within reaction textures produced during contact heating yield critical information on the conditions and process of overprinting. This includes constraints on crustal depths at the time of intrusion, yielding multiple pressure–temperature–time constrains on the evolution of a terrane. In such geologic settings where multiple thermal events have occurred, contact aureoles can therefore provide important additional thermobarometric information useful for understanding temperature and pressure evolution of both regional and overprinting events.

The ideal scenario involves contact aureole rocks that preserve evidence of *P* and *T* of the preceding regional event, for example unreacted inclusions armored within garnet porphyroblast interiors, while showing an approach to equilibration at the contact-metamorphic conditions along porphyroblast margins and in the matrix. However, in most cases, the assemblages in contact aureoles at best accurately record only the conditions of contact metamorphism or, more likely, some disequilibrium blend of compositions from the two events: unambiguous thermobarometric information for the preceding regional mineral assemblage may be impossible to recover. Furthermore, the information from overprinting textures is only useful for understanding tectonic processes if the intrusive event is tectonically related (i.e. temporally constrained) to the regional metamorphism.

In this study, we examined the high-*T* contact aureole of a small, deep-crustal gabbro pluton (inner aureole $T \sim 800$ °C at 435–445 Ma) that overprinted older regional metamorphic rocks of upper amphibolite-facies grade ($T \sim 620$–640 °C at 465–470 Ma). Based on magma composition, location and intrusive relationships (Ratcliffe, 1970), the small (<10 km^2) Croton Falls pluton (**Fig. 2.1**) is one of a group of mafic-ultramafic late- to post-orogenic plutons that intruded a classic regional metamorphic terrane of Taconic age in southeastern New York, approximately 85 km north of New York City (Balk, 1927; Whitney *et al*., 1996; Ratcliffe *et al*., 1998). Regional metamorphic grade adjacent to this pluton is upper amphibolite facies (sillimanite+staurolite in pelitic schists). The samples studied here yield both unambiguous quantitative evidence of peak *P*–*T* regional conditions prior to the contact event that are consistent with those in the near vicinity reported previously (e.g. Whitney *et al*., 1996), and clear mineralogical evidence of changing *P* and *T* associated with the contact metamorphic overprint.

This evidence is subtle and includes 1) Diffusional modification of pre-existing garnet porphyroblast rims and new growth of compositionally distinct garnet rims, 2) systematic differences in composition of armored inclusions of plagioclase and biotite within unmodified garnet porphyroblast interiors and the compositions of these same phases within the modified garnet rims and in the reactive matrix of the rock, 3) the presence of zincian aluminous spinel in the matrix and within modified garnet rims, 4) an apparent depletion in bulk alkalis (especially K) and silica that reflects metasomatism through melting and melt extraction during the contact

heating to *T* approaching or exceeding 800 °C at 0.8 GPa, and 5) the presence of rutile after ilmenite in the matrix of the rock.

The purpose of this study was to document the late Ordovician to early Silurian petrologic and tectonic evolution of the area using thin section-scale petrographic observations, chemical mapping of garnets using the electron microprobe, compositional analyses of all relevant phases, and thermobarometric calculations based on those analyzed compositions. This study has significant implications beyond local tectonics and metamorphism in that it both reveals evolving *P–T* conditions immediately following regional metamorphism and during the contact event itself, and also documents a highly unusual case in which higher-*P* contact metamorphism is superimposed on lower-*P* regional metamorphic rocks only slightly older than the contact event. We know of no other studies that have documented such excellent preservation of evidence for metamorphic conditions in both an earlier regional event and subsequent overprinting within an aureole.

With regard to evolution of pressure, a normally expected pattern in regional metamorphism is for cooling following the metamorphic peak to be accompanied by uplift and exhumation, with concomitant decompression (England & Thompson, 1984). We will provide a scenario below that uses available information on northern Appalachian tectonics, particularly emplacement of Taconic allochthons at shallow crustal levels late in the Taconic orogenic cycle, to explain this anomalous pattern for southeastern New York.

2.2 Geologic Setting of Plutons in Northern Westchester County, Southeastern New York

The sample described in this paper was collected from an outcrop less than 10m from the igneous contact of the Croton Falls mafic pluton in the Manhattan Prong of northern Westchester County, New York. The Manhattan Prong is a complex and intensely folded tectonic terrane consisting of older "basement" rocks – the Fordham Gneiss (Grenvillian age – 1000–1100 Ma) and the Yonkers Gneiss (Avalonian age – *c.* 650 Ma) – complexly folded with a cover of Cambrian and Ordovician metasedimentary and volcanic rocks and then intruded by late Ordovician or early Silurian mafic plutons (**Fig. 2.1**). The cover sequence above an angular unconformity includes basal quartzites and marbles (Lowerre and Inwood Formations) and the Manhattan Schist (Hall, 1968). The undated Croton Falls pluton comprises presumed Silurian-age gabbro intruded into the Manhattan Schist Formation. This latter unit is dominated by

aluminous pelitic schists, but also contains amphibolites and some carbonate lenses. Hall (1968) noted that the Manhattan Schist is likely a composite unit, with its uppermost member, Manhattan C, being in thrust rather than conformable contact with the lower parts of the Manhattan. This early Taconic thrust shearing appears to have predated the Taconic regional metamorphism (Hall, 1968).

The Croton Falls pluton and the nearby smaller Peach Lake mafic pluton are lenticular sill-like intrusions assumed to be part of the same Early Silurian magmatic event that produced the larger (roughly 60 km^2) funnel-shaped Cortlandt Complex (Ratcliffe *et al.*, 1982; Henry, 1997). The Cortlandt Complex, located on the Hudson River about 30 km southwest of Croton Falls and about 40 km north of New York City, is a well-known, deep-crustal composite mafic pluton that has been studied since the mid-19th C. (Dana, 1881, 1884; Williams, 1887, 1888; Rogers, 1911; Bowen, 1956; Friedman, 1954, 1956). Previous work conducted in the aureole of the Cortlandt Complex, particularly at its mafic eastern end, showed petrologic evidence of higher-*P* contact metamorphism at *c.* 435 Ma, superimposed on slightly older Taconic regional metamorphism at *c.* 465 Ma (Ratcliffe *et al.*, 1982; Waldron, 1986). Waldron (1986) tentatively suggested a 0.2–0.3 GPa pressure increase recorded for the contact metamorphism 25–30 million years after the regional metamorphic peak, and this has been confirmed and documented in the current work, with obviously significant tectonic implications.

The Cortlandt Complex (and likely the smaller contemporaneous satellite intrusions like Croton Falls and Peach Lake) underwent significant contamination and assimilation through interaction with still-hot country rocks at the deep crustal levels represented by the present erosion level. The short interval for cooling following the peak Taconic regional metamorphism resulted in a high residual *T* of the country rocks at the time of intrusion (probably in excess of 500 °C), which resulted in significantly increased reactivity through both mechanical and geochemical processes (including the likelihood of extensive localized melting) that enhanced magma–country rock interactions. At least one of the later Cortlandt plutons (pluton V) contains large volumes of diorites and norites that resulted from very large-scale lit-par-lit injection of gabbroic magma into country rocks, some of which can be identified within the complex as curtains and screens of variably digested material (Ratcliffe *et al*., 1982; Bender *et al*., 1984).

Intense physical and chemical interaction of magma and country rocks is evident at the southeastern margin of the Cortlandt Complex where the intruding mafic magma has mixed with

granitoid melt extracted from partially melted schists in the aureole. This interaction produced a mappable unit of hybrid monzonorite and monzodiorite along the igneous contact and a zone of migmatitic outcrops with intimately interlayered monzonorite and residual schistose rock. This same lithology is seen on a smaller scale at the Salt Hill xenolith locality rimming large aluminous xenoliths within the mafic to ultramafic rocks of pluton VI (Ratcliffe *et al.*, 1982; Johnson & Tracy, 1998). Here it presumably reflects the mixing of mafic magma with melts extracted from the pelitic schist xenoliths during heating to temperatures likely in excess of 1200 °C (Dorfler *et al*., 2012).

One striking feature of all the contact aureole exposures at both the Cortlandt Complex and the Croton Falls pluton is their narrowness – rarely can a contact-aureole overprint be identified as extending distances more than a hundred meters or so from an exposed or inferred igneous contact. Narrow aureoles are likely due to the dry nature of the parental gabbroic magma and the relatively dehydrated character of the country rocks following the upper-amphibolite facies Taconic metamorphism.

Taconic regional metamorphic isograds in this area of northern Westchester County (Stanley & Ratcliffe, 1985; Sutter *et al.*, 1985) and also Dutchess County to the north (Whitney *et al.*, 1996), assumed to be roughly horizontal or shallowly dipping at the time of their formation (at *c.* 465 Ma), now dip sub-vertically. These dipping surfaces were truncated by pluton contacts in their approximate current orientation at the time of intrusion at 435–440 Ma, indicating that rotation of the regionally metamorphosed country rock isograds must have occurred following the peak of regional metamorphism but before mafic pluton emplacement (Waldron, 1986). This deformation of the country rock is associated with the waning stages of the T_3 Taconic event that occurred after accretion of allochthons and marks the end of the collision of Laurentia with an island or continental arc (Stanley & Ratcliffe, 1985; Sutter *et al.*, 1985; Hames *et al.*, 1991; Ratcliffe *et al.*, 1998). The Cortlandt pluton itself shows only slight deformation along discrete fracture or shear zones and has not been regionally metamorphosed, unlike mafic intrusive rocks of roughly similar age to the east in Massachusetts and Connecticut that fall within the western edge of the Acadian regional overprint at *c.* 390 Ma.

Due to the intense geochemical interactions between the mafic plutons in Westchester County and their country rocks, establishing the age of intrusion has presented long-standing geochronologic difficulties (summarized by Ratcliffe *et al*., 1982). The earliest published

geochronology involved K–Ar data from biotites in the contact aureole rocks from the Cortlandt Complex, and dated the contact event around 435 Ma (Long & Kulp, 1962), similar to subsequent studies yielding ages between 430 and 440 Ma (Dallmeyer, 1975; Bender, 1980; Ratcliffe *et al.*, 1982; Bender *et al.*, 1984). This indicates that the intrusive event postdates Taconic regional metamorphism and deformation of the country rocks (465–470 Ma) by about 25–35 million years (Sutter *et al.*, 1985). Given this relatively brief interval between the Taconic metamorphism (625 °C at *c.* 465 Ma) and the contact event (*c.* 435 Ma), the country rocks are unlikely to have cooled significantly between these events. Assuming an average cooling rate of 3–5 °C/m.y., the ambient temperature at the time of intrusion would have been roughly 475–535 °C.

Previous workers (Ratcliffe *et al.*, 1982; Bender *et al.*, 1984; Tracy & McLellan, 1985; Waldron, 1986; Henry, 1997; Johnson & Tracy, 1998; Johnson & Tracy, 1999) extensively documented the geochemical and petrologic effects of the contact event in both the Cortlandt Complex and the Croton Falls pluton. In the PhD thesis of Waldron (1986), preliminary geobarometric work suggested that Cortlandt Complex emplacement occurred at higher-*P* conditions than the regional event. Her GASP and GRAIL calculations from the contact rocks indicated pressures of 0.7–0.8 GPa, significantly higher than pressure estimates for regional metamorphic rocks outside the thermal aureole (garnet grade through sillimanite–muscovite–staurolite grade, yielding on average 0.4–0.6 GPa). Regional metamorphic conditions of the staurolite zone in Dutchess County, roughly 20 km to the north, were 485–557 °C at 0.3–0.59 GPa (Whitney *et al.*, 1996; Chen, 2009), correlating well with results from the Cortlandt Complex area.

Henry (1997) studied garnet-bearing assemblages in the Manhattan Schist and in the contact aureoles of the Peach Lake and Croton Falls plutons. *P–T* estimates for sample CF-3 in the Croton Falls contact aureole, ~ 15–20 m from the igneous contact, yielded equilibrium conditions of ~700 °C and 0.4 GPa using the garnet–biotite Fe–Mg exchange thermometer (Ferry & Spear, 1978) and the GASP geobarometer of Koziol & Netwton (1988). Sample CF-5, described in detail in this paper, was collected approximately 10 m closer to the igneous contact and thus shows a higher *T* than CF-3 and a resetting of recorded *P* to show values around 0.8 GPa, similar to contact *P–T* values suggested by Waldron at the Cortlandt Complex. Because these two plutons in northern Westchester County are smaller than the Cortlandt and their

aureoles are narrower than the Cortlandt contact aureole, the maximum *T* reached by any rocks not immediately at the igneous contact may not have been sufficient to reset mineral compositions to reflect the new ambient *P*.

2.3 Sample Description of CF-5

The primary sample used in this study, CF-5, was collected less than 10 m from the inferred igneous contact of the Croton Falls pluton and is the highest-grade contact metamorphosed sample collected. The absence of potassic feldspar and muscovite (trace amounts of muscovite are present as inclusions in one garnet porphyroblast), and abundance of sillimanite and aluminous spinel, suggest that CF-5 is deficient in sodium and potassium and enriched in aluminum relative to typical pelitic schists (particularly the Manhattan Schist, which has ubiquitous muscovite and potassic feldspar), implying that melting and melt extraction depleted the rock of alkalic components, probably in the form of an escaped anatectic "granitic" melt. The metamorphic assemblage, which we presume to be the contact-metamorphic assemblage, is quartz (qz)–plagioclase (plg)–biotite (bt)–garnet (grt)–sillimanite (sil)–spinel (spl)–ilmenite–rutile (ilm–rut)–graphite (gr) with trace amounts of muscovite (mu) and no potassium feldspar (kfs). Additionally, abundant biotite, plagioclase, sillimanite, and quartz inclusions occur throughout garnet porphyroblasts (**Fig. 2.2**).

Major and trace-element mineral analyses were obtained using a CAMECA SX-50 electron microprobe at Virginia Tech, which was also used for WDS elemental mapping. Quantitative analysis of major and minor elements used a 15 kV accelerating potential with a beam current of 20 nA. Garnet WDS elemental mapping was typically done at 15 kV with a beam current of 300 nA. Quantitative analyses were performed using a combination of natural and synthetic standards, with ZAF-type matrix corrections performed using the PAP protocol (Pouchou & Pichoir, 1984). Mineral formulas were calculated based on the number of oxygens (anhydrous) per formula unit for each mineral.

2.3.1 Garnet

Although several Croton Falls samples contain garnets that exhibit complex zoning patterns unlikely to have formed in a single thermal event, the porphyroblasts from sample CF-5 have the clearest and most striking near-rim zoning discontinuity (**Fig. 2.3**), in addition to

containing abundant inclusions of biotite, plagioclase, sillimanite, quartz and ilmenite distributed throughout both crystal interiors and rims. In fact, during preliminary examination of this sample, a fundamental clue that there might be preserved interpretable evidence of both regional and contact equilibration of minerals suitable for geothermobarometry came from compositional mapping of these garnets.

Multiple garnets in sample CF-5 were WDS X-ray mapped for Fe, Mg, Ca, and Mn; Ca and Mg maps of several representative crystals are shown in **Fig. 2.3** (relatively small variations in Fe and Mn render these maps less useful). All garnet porphyroblasts examined showed similar abundance and distribution patterns with respect to an abrupt zoning discontinuity with Ca-enriched rim zones. Biotite, plagioclase, sillimanite, quartz, and ilmenite inclusions are abundant in both interiors and rims of the porphyroblasts; in addition, rare inclusions of zincian aluminous spinel occur in the rims of garnets or in the matrix, but never inside the Ca-zoning discontinuity. Quantitative garnet zoning profiles indicate that Fe and Mn contents slightly increase and decrease, respectively, toward the rims of most garnet porphyroblasts. Neither element changes in concentration at the zoning discontinuity indicated by the Ca maps (**Fig. 2.3**).

Tables 2.1–2.3 list the mean compositions of garnets and their respective rim and interior biotite and plagioclase inclusions used in thermobarometric calculations. Non-averaged compositions of each garnet, biotite and plagioclase analysis used for thermobarometric calculations are listed in **Table A1**. Garnet cores are substantially more Mg-rich ($X_{\mathrm{Grt}}^{\mathrm{prp}}$ $X_{Grt}^{\mathrm{Int-Pl}}$ up to 0.24) than rims ($X_{Grt}^{\mathrm{Int-Pl}}$ as low as 0.15) and profiles show a sharp decrease in Mg at the Ca-zoning discontinuity marking the inner edge of the rim zone (**Tables 2.1–2.3** and **Table A1**). The rims of the garnets are strongly and abruptly enriched in Ca at this interface, with X_{Grt}^{grs} varying from 0.03 inside the discontinuity to as high as 0.10 in the outermost rim (shown quantitatively in **Fig. 2.3** and spatially in **Fig. 2.4**). Detailed analytical traverses through the crystal rim shown in **Fig. 2.4** (e.g. **Fig. A5**) highlight the sharp boundary between core and rim, and the almost constant composition over several hundreds of microns within the rim. This implies that the rim records new garnet growth rather than exchange with the matrix and subsequent intracrystalline diffusion. An additional discontinuous, narrow Ca-enriched rim is also seen on the very outermost crystal edge of parts of this garnet.

Ca profiles across adjacent garnet and plagioclase inclusions were generally flat although occasionally 5–10 μm zones of slight garnet modification were apparent next to plagioclase (e.g.

Fig. 2.5D). Garnet compositions adjacent to the biotite inclusions commonly show only a very slight increase in Fe/Mg ratio toward the garnet–biotite boundary (e.g. **Fig. 2.5B**).

2.3.2 Biotite

Biotite is present in both the matrix mineral assemblage and as armored inclusions in garnet porphyroblasts (**Fig. 2.3**). Biotites from the garnet interiors (inside the Ca-zoning discontinuity) and from garnet rim zones were selected and analyzed using traverses perpendicular to the biotite–garnet boundary at 2 micron spacing. Eighteen analytical traverses were done on inclusions in the interiors of three separate garnets (inside the Ca rim discontinuities), and twenty-four analytical traverses were done on biotites in the garnet rim zones or at the garnet–matrix boundary of the same three garnets. Biotite inclusions in garnet interiors have quite different Mg concentrations than biotites in the rim zones or in the matrix. There is no evidence of significant zoning in either Fe or Mg (or in Fe/Fe+Mg) within interior biotite inclusions or within biotites in the Ca-enriched rim zones or matrix. Biotites from the Ca-enriched rim zones or at the garnet–matrix boundary were grouped together into a "rim–matrix biotite" population, because of the strong compositional similarity from both areas of the sample (all cation abundances differed by less than 0.02 on an 11-oxygen equivalent anhydrous formula basis). All analyzed interior biotite inclusion examples (inside the Ca-zoning discontinuity in garnets) were grouped into an "interior biotite" population, and were monitored for diffusional exchange of Fe and Mg with surrounding garnet (**Tables 2.1–2.3** and **Table A1**).

The average Fe^{2+} content (in cations per 11 oxygens) of interior biotites is 0.95 compared to 1.21 in rim–matrix crystals (**Tables 2.1–2.3**). Biotite Ti contents do not vary significantly between the two microenvironments and are 0.18 and 0.19 cpfu in garnet interiors and rims, respectively. The Mg content of rim–matrix biotite is lower than that of the interior inclusions, averaging 1.10 versus 1.40 cations, respectively (see also element maps in **Figs 2.3 and 2.5**). Fe/(Fe+Mg) ratios ranged from 0.34 to 0.46 in interior biotite inclusions and from 0.50 to 0.56 in rim–matrix biotites. The extent of compositional modification of interior or rim–matrix biotite inclusions due to retrograde Fe–Mg exchange with enclosing garnet will be dealt with in the section below on thermobarometry.

2.3.3 Plagioclase

Much like biotite, plagioclase inclusions are prevalent throughout both the interior microenvironment of the garnet porphyroblasts and within the Ca-enriched rim zones. Plagioclase inclusions interior to the Ca-enriched rim zones have lower anorthite content (averaging X_{An}^{Pl} = 0.35, see **Tables 2.1–2.3**) than plagioclase inclusions in the garnet rims and the rims of matrix plagioclase grains (averaging X_{An}^{Pl} = 0.42). We performed twenty-one analytical traverses of plagioclase inclusions in the interiors of three garnets and fifteen analyses of inclusions in the rim zones and garnet rim–matrix boundary of two garnets. Crystals in the matrix show distinctive Ca zoning with anorthite-enriched rims (average is X_{An}^{Pl} = 0.42, maximum is X_{An}^{Pl} = 0.49) on less calcic (as low as X_{An}^{Pl} = 0.31) cores (**Fig. 2.6** and **Table 2.4**). The zones of Ca-enrichment are irregular and can vary from a relatively euhedral to a patchy zoning, as shown in **Fig. 2.6**. They are compositionally similar to crystals along the garnet rim–matrix border and inclusions within the Ca-rich garnet rims (as high as X_{An}^{Pl} = 0.47), which we believe represent a single compositional population, henceforth termed the "rim–matrix plagioclase" population. The interior compositions of matrix plagioclases are extremely similar to the armored inclusions in garnets (X_{An}^{Pl} = 0.33). The majority of these included plagioclases display little to no Ca zoning, and immediately adjacent garnet shows minimal change in Ca content toward the garnet–plagioclase interface (**Fig. 2.5**). In a few instances, minor Ca zoning is present in plagioclase inclusions in garnet interiors and in the adjacent garnet. In those cases, evidence of healed microcracks in the host that propagate from the inclusion to the matrix are clear, rendering these inclusions open to late-stage communication with the matrix and not indicative of any larger-scale diffusion within garnet interiors.

2.3.4 Spinel

Green aluminous spinel occurs both in the matrix and in Ca-enriched rim zones of garnet. It is not present inside the Ca-enriched rims of garnet porphyroblasts and is absent from samples distal to the Croton Falls intrusion that only experienced the regional Taconic event. Crystals are dominantly Fe–Mg aluminous spinel, but with significant Zn, averaging around 0.46–0.50 mole fraction gahnite (gah) and sometimes reaching X_{Sp}^{gah} = 0.66. **Table 2.5** lists the average composition of the six spinels analyzed in the sample. They exhibit no appreciable zoning, either

in the matrix or in the garnet rim zones. **Figure 2.7** shows Al and Ca maps of spinel within the Ca-enriched rim zone in a garnet porphyroblast. The larger crystal has two inclusions: plagioclase and sillimanite. Chemical analysis of the included plagioclase reveals that it is nearly identical to the Ca-enriched rims of matrix plagioclase and plagioclase inclusions in the Ca-enriched garnet rim zones (having X_{Ca}^{plag} = 0.42; **Table 2.5**).

2.3.5 Ilmenite and Rutile

Ilmenite is ubiquitous throughout the thin section, both in the matrix and as inclusions in garnet porphyroblasts. However, many of the crystals in the matrix show replacement by rutile along margins and within cracks. EDS chemical maps show that in addition to rutile in these locations, Mn content of ilmenite increases towards the replacement interfaces (**Fig. 2.8**).

2.4 Pressure-Temperature Calculations

Based on our initial observations of distinct Ca-enriched rim zones in garnets and matrix plagioclase, as well as on previous thermobarometric work conducted on regional metamorphic rocks of similar grade in the area, we conclude that this Ca-enrichment of both garnet and plagioclase records a contact overprint at higher pressure on the original Taconic regional metamorphic assemblage, as represented by garnet interiors with associated mineral inclusions. Compositions of the inclusions of biotite and plagioclase within and around the garnet (in the presence of ubiquitous quartz and sillimanite inclusions) allow for thermobarometric calculations of each microenvironment.

Elemental zoning maps and compositional profiles of garnet porphyroblasts were used to select suitable garnet–inclusion couples for thermobarometry. Microprobe traverses with two-micron spacing documented each garnet–inclusion pair, and appropriate analyses of both the inclusion and the proximal garnet host were chosen to represent equilibrium pairs for thermobarometry. Biotite and plagioclase inclusions, and garnet adjacent to plagioclase, were unzoned regardless of inclusion size, whereas garnet adjacent to biotite showed some degree of localized zoning in the form of a diffusional concentration profile with increased Fe/(Fe+Mg) toward the garnet–biotite boundary, reflecting retrograde cation exchange during cooling (**Figs 2.9 and A1**). Garnet compositions for inclusion garnet–biotite thermometry were carefully selected in each micro-traverse (as in **Figs 2.3 and 2.5**) to be sufficiently far from the boundary

so as to be unaffected by this zoning and to be consistent with overall zoning within garnet interiors away from inclusions. In no case did this require sampling more than 25 microns from a boundary, and typically not more than 10 microns. A majority of analyzed biotite inclusions showed no modification at all of adjacent garnet composition. Average compositions of each phase in the key textural domains are given in **Tables 2.1–2.3** and each garnet–inclusion pair composition analyzed is listed in **Table A1**.

All garnets examined are relatively unzoned within their interiors presumably due to diffusional homogenization during slow cooling from a peak *T* of roughly 650 °C following the Taconian regional metamorphism. Interior garnet–biotite and garnet–plagioclase pair compositions can thus themselves be paired together based on proximity to each other to provide a *P* constraint for garnet–biotite thermometric pairs and a *T* constraint for garnet–plagioclase barometric pairs. This also permitted generation of garnet–biotite–plagioclase assemblages (**Table A1**) which formed the basis of THERMOCALC Average*PT* calculations. *P–T* conditions of the later contact metamorphism were calculated using the compositions of Ca-enriched garnet rims, and both biotite and high-Ca plagioclase inclusions within those rims. Plagioclase within the matrix has Ca-enriched rims that are compositionally equivalent to plagioclase inclusions within garnet rims, so the garnet–rim dataset was supplemented with calculations using the compositions of matrix plagioclase and biotite and the outermost garnet rims.

One potential thermometric concern relates to possible error associated with the compositional reequilibration of biotite inclusions due to Fe–Mg exchange with adjacent garnet during cooling. All analyzed interior biotite inclusions are homogenous, although adjacent garnet (as noted above) can preserve a diffusional exchange profile (**Fig. 2.9**). Biotite homogeneity can be explained by rapid diffusion within biotite during retrograde cation exchange, however this leaves no choice but to use these modified biotite inclusion compositions to calculate temperatures with nearby garnet not affected by diffusional exchange with the inclusion. Temperature calculation using the closest approximation to original garnet at the boundary and the reequilibrated biotite composition will thus produce *T* estimates for the interior assemblage that are slightly lower than the actual original *T*. We therefore emphasize that without correction, some of the thermometric results provide a lower limit for the equilibration temperature of the pre-contact assemblage (i.e., regional metamorphism). We performed mass-balance calculations to determine how much the shift in biotite composition due to minor diffusional exchange in Fe

and Mg (lowering of Fe/Fe+Mg in biotite) could have affected thermometric calculations. In a simple one-dimensional model, integration under concentration profiles in garnet (see **Fig. 2.9**) permits calculation of the extent of change in biotite Fe/(Fe+Mg) based upon a simple assumption of volumetric equivalence (following Spear and Parrish, 1996). Our results indicate that post-growth diffusive exchange and biotite homogenization will produce less than a 30 ˚C lowering of apparent temperature recorded by garnet–biotite couples. On any case, interior garnet–biotite pairs can be assumed to yield a minimum *T* for regional metamorphism.

2.4.1 GASP and Garnet–Biotite Fe–Mg Exchange Equilibria

Temperatures reported here were calculated from garnet–biotite pairs using the Hodges & Spear (1982) thermometric calibration and pressures were derived from Ca partitioning between garnet and plagioclase in the so-called GASP equilibrium calibrated for sillimanite by Koziol (1989). The choice of Hodges and Spear (1982) was prompted largely by examination of results using a variety of garnet–biotite thermometers, including Thompson (1976), Holdaway and Lee (1977), Ferry and Spear (1978), Hodges and Spear (1982), Perchuk and Lavrent'eva (1983), Williams and Grambling (1991) and Perchuk *et al.* (1991). A direct comparison of these various calibrations of the thermometer is shown in **Fig. A2**. Interestingly, the temperature spread amongst all calibrations was much lower (~ 50 °C) for the lower-*T* garnet–core pairs, and higher for the rim–matrix calculations (~ 100–150 °C). The choice of Hodges and Spear (1982) was dictated mostly by two factors: it has produced the most consistent results in previous work we have done and, in this study, temperature calculated using this calibration is most consistent with the THERMOCALC results.

Quartz and sillimanite are ubiquitous throughout all microenvironments (garnet cores, Ca-enriched rim zones and matrix), permitting application of the GASP net-transfer equilibrium to all garnet–plagioclase pairs. Results of coupled garnet–biotite thermometry and GASP barometry are shown for each analyzed garnet–biotite–plagioclase sub-assemblage from three garnet crystals in **Fig. 2.10A**, where arbitrary calibration uncertainties of ± 50 ˚C and ± 1 kbar have been assigned to each analysis. Data fall into two groups, with the compositions of all analyzed garnet interiors and inclusions from within those interiors yielding *T* between 550 and 660 ˚C and *P* between 0.4 and 0.6 GPa. Garnet rims and their inclusions and adjacent matrix phases yield *T* between 725 and 830 ˚C and *P* between 0.72 and 1.10 GPa. Averaging the

inferred pressures and temperatures from interior and rim of each garnet yielded five values (no rim data are available for garnet D rim). Excluding the nominal thermodynamic uncertainty shown in **Fig. 2.10A** (i.e. describing only the standard deviation from *P–T* scatter of analyses) these averages clearly cluster into two populations (**Fig. 2.10B**), with average *P–T* values of ~ 0.5 ± 0.1 GPa and ~ 620 ± 50 °C (for the interior assemblage) and ~ 0.9 ± 0.1 GPa and ~ 790 ± 50°C (for the rim–matrix assemblage). Combining results of all individual garnet–biotite pairs reveals an unambiguous bimodal pattern, with peaks at ~ 600 and 800 °C (**Fig. A3**).

*2.4.2 Average*PT *Calculations from THERMOCALC*

P–T conditions for each garnet–biotite–plagioclase sub-assemblage (with quartz and sillimanite) were also calculated using the Average*PT* method in THERMOCALC 3.33 (Powell & Holland, 1988, 1994, 2008; Powell *et al.*, 1998). This generates an independent set of reactions (see **Fig. A4**) representing all possible equilibria to calculate a single, average *P* and *T*.

Activity calculations used T. Holland's program 'A-X' (http://www.esc.cam.ac.uk/research/research-groups/holland/ax) with the activity models from White *et al*. (2007) for garnet and biotite and from Holland and Powell (2003) for plagioclase. Again, garnets A and C contained sufficient plagioclase and biotite pairs to calculate an interior and rim–matrix *P–T* whilst garnet D contained only enough inclusions for interior values. Average*PT* results yield interior estimates of 563–718 °C and 4.2–6.6 and rim estimates of 741–883 °C and 7.4–10.7 GPa (at 95% confidence, **Fig. A4**). The thermodynamic standard deviation for each interior analysis is ~ ± 130 °C and ± 2.0 GPa and for each rim–matrix analysis ~ ± 180 °C and ± 3.0 GPa. These large uncertainties are primarily due the small assemblage set used in the THERMOCALC calculation, with rare chlorite and muscovite inclusions excluded from calculations because evidence of equilibration with the garnet–biotite–plagioclase triplets is lacking. Uncertainties between *P* and *T* are correlated, so assuming that *T* is known and solving using THERMOCALC solely for *P* can substantially reduce uncertainty. For assumed temperatures from the Average*PT* calculations (i.e. 563–718 ˚C for interior compositions and 741–883 °C for rim compositions), uncertainties on pressure (2σ) are reduced to approximately 0.1 GPa in all cases (**Fig. 2.11A**). Average*PT* results calculated using THERMOCALC from each chemical domain fall in restricted *P–T* ranges, as illustrated by the relatively small standard

deviations of the averages of these populations, shown in **Fig. 2.11B** (which excludes thermodynamic uncertainty).

P–T results from each garnet–biotite–plagioclase triplet are given in **Table A1**, with the average of all garnet interior and garnet rim analyses summarized in **Table 2.6**. It is important to note that the two populations of *P–T* values are unambiguously separated in *P–T* space, supporting the hypothesis that the compositionally different assemblages reflect two separate metamorphic events, with negligible post-peak *P–T* alteration of the regional assemblage.

2.5 Discussion

Thermobarometry results indicate preservation of two separate metamorphic events from two chemically distinct microenvironments in a single sample. The mineral assemblages in the interior of garnet porphyroblasts are interpreted to record a lower-pressure event that represents earlier Taconic regional metamorphism. Previous investigations conducted in the study area and farther north in Dutchess County, NY, record similar *P–T* conditions for this regional event implying that our garnet-interior assemblage does, indeed, record regional Taconic metamorphism (**Table 2.6**; Whitney *et al*., 1996; Chen 2009). Evidence for this in CF-5 is only recorded by the compositions of garnet interiors, armored inclusions within garnet, and matrix plagioclase interiors. Petrographic and electron microprobe evidence of contact overprinting includes Ca-enriched garnet rim zones, Ca-enriched rims on matrix plagioclase, spinel crystals in the matrix and in garnet rims, and the absence of muscovite (and potassium feldspar) in the matrix. The assemblage consisting of Ca-enriched rim zones around garnets, inclusions within these rims, matrix biotite, and rims of matrix plagioclase, is interpreted to record a high-pressure high-temperature overprint, which represents emplacement of the Croton Falls gabbroic pluton.

The lack of strong Mn zoning in garnets from core to rim suggests flattening of an original zoning profile through diffusion. We interpret this to be the result of diffusion following the regional metamorphism during slow cooling from a metamorphic peak *T* well above 600 °C, and it is similar to garnet concentration profiles in other Taconian garnets from similar regional metamorphic grade in the region (Whitney *et al.*, 1996). The extent of modification of Taconic prograde garnet growth zoning (either during the regional event or in the contact reheating) is not entirely clear and may be irretrievable without more complex modeling (e.g. Caddick *et al.*, 2010).

The peak Taconic regional metamorphic assemblage varies throughout the Manhattan Schist, but in the regional sillimanite–muscovite–staurolite zone is quartz–plagioclase–biotite–muscovite–potassium feldspar–garnet–staurolite–sillimanite–ilmenite–pyrrhotite. CF-5 lacks muscovite and staurolite in the matrix, indicating that both were lost during the contact-heating event. Rocks of similar regional and contact metamorphic grade in the Cortlandt Complex contact aureole contain rare small staurolite inclusions within garnet interiors but not in garnet rims or in the matrix.

2.5.1 Partial Melting and Changes in Modal Garnet and Plagioclase Growth

Heat flux from the Croton Falls gabbroic intrusion is inferred to have produced temperatures high enough to result in partial melting of metapelitic lithologies in the innermost contact aureole – *T* in excess of 800 °C at about 0.8 GPa. This would have depleted such bulk compositions in silica, H_2O and alkalic components through the breakdown of muscovite, recrystallization (and simultaneous volume reduction) of plagioclase and incorporation of these components into a more-or-less granitic melt. Sparse outcrop exposures do not allow certainty on the fate of this melt fraction, but samples collected within the outer zone of the pluton consist of apparent hybridized lithologies such as monzonorite and monzodiorite that resulted from mixing of the granitic fraction with the mafic magma. Similar hybridization is extensive at the nearby Cortlandt mafic complex (Ratcliffe *et al*., 1982; Waldron, 1986).

Resultant rims of matrix plagioclase crystals in the residual contact aureole rocks have a more calcic composition than original plagioclase (An_{37}), due to preferential loss of albite component to melt. The breakdown of plagioclase and biotite (and probably staurolite as well, see below) also contributed to new garnet rim growth, in composite reactions much like:

$$3 \text{ anorthite} = \text{grossular} + 2 \text{ sillimanite} + \text{quartz} \quad (2.1)$$

$$\text{biotite} + 2 \text{ quartz} + \text{sillimanite} = \text{pyrope/almandine} + \text{melt (Kfs} + H_2O) \quad (2.2)$$

New garnet rims formed during the contact event were necessarily more Ca-rich in order to maintain an appropriate Ca partition with the newly formed plagioclase rims (An_{47}) at the

ambient contact-metamorphic *P–T* (i.e., higher than regional *P–T*). A transient intergranular distribution of melt may have acted as a diffusive transport medium through which all phases could efficiently interact, aiding removal of silica and alkalic components to melt and facilitating diffusive communication between newly formed or recrystallized garnet and plagioclase rims. Because multi-component diffusion in plagioclase is so slow (Grove *et al*., 1984), Ca-enrichment of plagioclase rims through simple diffusive loss of the albite component would be unlikely, and recrystallization/reprecipitation of more calcic plagioclase around unaltered cores, perhaps mediated by local melt, is a more viable mechanism. The patchy nature of many anorthite-enriched plagioclase margins is consistent with this dissolution/reprecipitation model for matrix crystals (**Fig. 2.6**).

Given that *both* garnet and plagioclase recrystallized simultaneously, we assign a change in equilibrium coefficient of the GASP equilibrium to increased pressure. If garnet were the only phase to recrystallize, it is clear that changing *K* could equally well reflect changing bulk rock composition as melt is extracted rather than a response to increased pressure (Spear and Kohn, 1996; Spear and Parrish, 1996; Spear *et al.*, 1999). Overall, there must have been a modest volume reduction of plagioclase in the matrix due to incorporation of a sodic plagioclase component into melt, and a concomitant increase in volume of garnet.

2.5.2 Staurolite,Sspinel and Evidence of New Garnet Growth

During contact heating, staurolite present in the sample broke down to produce garnet and spinel:

$$2 \text{ staurolite} + 2 \text{ quartz} = \text{garnet} + \text{spinel} + 7 \text{ sillimanite} + H_2O \text{ (melt)}. \quad (2.3)$$

In sample CF-5, spinel is present only in the matrix or in Ca-enriched garnet rim zones. Typical Manhattan Schist samples from the staurolite–sillimanite zone contain abundant staurolite, so its dissolution (assuming an originally minor Zn content) would produce the small modal amount of high gahnite spinel observed in CF-5.

One of the analyzed spinel crystals, contains completely armored plagioclase and sillimanite inclusions. The high anorthite nature of the plagioclase (similar to matrix plagioclase

rims) indicates that spinel growth either post-dated or was contemporaneous with the reactions involved in matrix plagioclase recrystallization. Further, the occurrence of spinel (which is absent from rocks experiencing just the regional Taconic metamorphism) only within garnet rims and matrix indicates that the Ca-enrichment of garnet rims must be due to new overgrowth during the contact event rather than inward diffusion of Ca into preexisting garnet. We note also that where garnet crystal edges appear to have been pinned by early (i.e. low An) plagioclase (e.g. the lower right corner of **Fig. 2.3D**), neither plagioclase nor garnet recrystallized. This presumably also indicates that melt distribution at highest temperatures was heterogeneous throughout this sample.

2.5.3 Summary of P–T History and Textural Development

The proposed succession of *P–T* conditions and textural development are briefly summarized with reference to **Fig. 2.12**, where panels 1–7 reflect textures and reactions at numbered stages on the *P–T* path. The first evidence of metamorphism preserved in CF-5 records Taconic regional metamorphism at ~ 650 °C, 0.5 GPa. This produced a staurolite–garnet–plagioclase-bearing assemblage, with matrix and plagioclase inclusion compositions of An_{37} (**Fig. 2.12**, stage 1). Approximately 0.3 GPa of subsequent loading (stage 2) is enigmatic, with no obvious recrystallization observed in samples that did not later experience contact metamorphic stages. The *P–T* path between the waning stage of Taconic metamorphism and Croton Falls contact metamorphism is thus poorly constrained, but it is clear that emplacement of gabbroic melts induced heating at 0.8–0.9 GPa in CF-5. This initiated a series of reactions (**Fig. 2.12**, stage 3) including partial plagioclase, biotite and muscovite breakdown, which generated melt and sillimanite, and contributed to rim overgrowth on pre-existing garnet crystals. Initial staurolite breakdown also formed sillimanite and garnet in this stage, and rutile may have begun replacing ilmenite. Residual staurolite from this stage is hypothesized to have been ZnO enriched because later breakdown produced gahnite-rich spinel as peak temperatures approached ~ 800 °C (stage 4). Continued garnet growth through stage 4 is recorded by entrapment of some of these spinel crystals (as shown in **Fig. 2.7**). Muscovite was eventually exhausted during melting.

Heating was presumably relatively brief with subsequent cooling (stage 5) initiating melt crystallization. This is primarily manifest as plagioclase rim recrystallization, and must have

occurred in a temperature range in which an increasingly sodic melt was in equilibrium with An_{47}. Volumetric constraints suggest that with addition of these rims, plagioclase crystals were still ~ 25% smaller than the initial An_{37} crystals in stages 1 & 2. A thin, outer rim of Ca-rich garnet also formed at this time (see also **Fig. 2.5**). No obvious leucosome pockets are preserved and a lack of late-stage muscovite growth implies that H_2O dissolved in melt was efficiently extracted from the system near peak–*T* conditions or during cooling. We thus infer melt loss before stage 7, which approximately marks the wet solidus for this system. We note, however, that it is currently unclear whether partial melt loss occurred during progressive heating or was restricted to cooling. There is little evidence for extensive subsequent Fe–Mg exchange between garnet and biotite (either as matrix grains or inclusions), possibly implying relatively fast cooling from contact metamorphic temperatures.

2.5.4 Tectonic Implications

Pressure and temperature calculations from this study indicate that the emplacement of the Croton Falls pluton occurred under pressure conditions 0.2–0.3 GPa higher (approximately 7–11 km deeper) than the peak regional metamorphic conditions. The likeliest and even inescapable explanation for such a pressure increase is some form of crustal thickening, presumably at shallow crustal levels, following regional metamorphism and prior to the contact event. We propose that the change in pressure is related to emplacement of Taconic thrust sheets during the waning stages of regional metamorphism at the end of the Taconic orogenic event. The end of the Taconic Orogeny (and the end of collision of the Laurentian margin with a continental arc) was marked by the accretion of thrust allochthons in what is now western New England and adjacent New York and consequent deformation of the underlying rocks, now reflected by rotated and steeply tilted Taconic isograds in the footwall, as explained above and documented extensively by previous investigators (Stanley & Ratcliffe, 1985; Sutter *et al*., 1985; Hames *et al*., 1991; Ratcliffe *et al*., 1998). Although strong deformation is pervasive throughout the Hudson Valley region, deformation of the non-tilted plutons of the Manhattan Prong (Cortlandt, Croton Falls, Peach Lake) is limited to discrete shear zones that appear to be of Acadian (*c*. 390 Ma) age, indicating that the major deformation and isograd tilting occurred prior to pluton emplacement within the 25–35 m.y. time span between the waning stages of regional metamorphism and the onset of contact metamorphism. This deformation was accompanied or

soon followed by emplacement of a thrust sheet (or sheets) over the region, likely originating from Cameron's Line (a major tectonostratiagraphic boundary that lies 10 km east of Croton Falls and is assumed to be the root of the Taconian suture zone). In an unpublished thesis, Waldron (1986) proposed the emplacement of an 8–10 km thick thrust sheet following rotation of the regional metamorphic isograds and prior to intrusion of the Cortlandt Complex based on a preliminary thermobarometric analysis that has been borne out by this study.

Much of the Taconic regional metamorphic terrane in western Connecticut and in New York that lies below the thrust surface bounding the Taconic allochthons must have experienced the pressure increase of 0.2–0.3 GPa that marked emplacement of the allochthons. However, only in sites associated with local pluton heating (e.g., Cortlandt, Croton Falls, Peach Lake) do we see any evidence in the rocks at thin section scale for this post-regional metamorphic loading related to allochthons. In order for a medium- to high-grade mineral assemblage to record evidence of a later metamorphic event, it would typically be required to add thermal energy (producing temperatures higher than the original event, unless fluid input is also pervasive) to allow a sufficient degree of recrystallization to be observed petrographically and recorded more subtly in modified mineral compositions. The heat required could effectively only be supplied by intrusion of mafic magma, which can produce temperatures higher than upper-amphibolite facies regional metamorphism in the inner parts of thermal aureoles, but only very locally. In areas where the temperature increase was not sufficient to induce observable recrystallization and consequent compositional adjustments, it would be impossible to document the emplacement of allochthons using thermobarometry in the sub-thrust metamorphic rocks. This raises the possibility that such post-metamorphic loading may be more common than currently expected but remains unobserved in the absence of temporally fortuitous mafic magma emplacement.

The inset in **Fig. 2.1** is a simplified geologic map of the southern New England/New York Appalachians west of Cameron's Line. Large late-Taconic allochthons or allochthon remnants are present in the region north of the study area. South of the Hudson Highlands (in Westchester County) these late allochthons appear to have been completely eroded away, exposing Taconic regional metamorphic rocks below the original thrusts. (Note that the Hibbard *et al.* [2006] map shown in **Fig. 2.1** indicates some Taconic allochthons south the Hudson Highlands, in Westchester County. These are early allochthons that predate the Taconic regional metamorphism.) The lack of late, shallow allochthons to the south indicates that there was deeper

erosion south of the Hudson Highlands, which has resulted in exposure of the mafic intrusions that were emplaced beneath the late thrust sheets and their country rocks. Evidence for isolated high-temperature, and likely high-pressure, contact-metamorphic conditions throughout the northern Manhattan Prong is reflected in the presence of zincian spinel either rimming or intergrown with staurolite in samples throughout the terrane and not necessarily associated with exposures of small mafic plutons (Brock & Brock, 1998). These authors ascribe the widespread occurrence of spinel to a region-wide granulite-facies event, but it seems more likely that there may have been other small lens-like mafic plutons similar to Croton Falls that have either not yet been exposed or are now eroded away, leaving only contact aureole rocks at the surface.

Geochronology of the mafic plutons (Dallmeyer, 1975; Bender, 1980; Ratcliffe *et al.*, 1982; Bender *et al.*, 1984) dates the intrusive events to about 435 Ma, only 25–35 million years after the last stages of Taconic regional metamorphism, implying that temperatures of the country rock were likely still 450–550 °C (assuming an average cooling rate of 3–5 °C/m.y. from 465–470 Ma peak regional temperature at 630 °C). How the emplacement of the allochthons might have affected a normal cooling pattern is currently not known.

It might be argued that the Taconic regional-metamorphic assemblage, now fully represented only in the garnet interiors in sample CF-5, has been subtly altered to reflect the pressure increase before these garnets ceased growing. However, there is little physical or chemical evidence of this: garnet interiors show no zoning and the *P–T* estimates from the interior garnet assemblages closely resemble values obtained for rocks of similar metamorphic grade from outside thermal aureoles in Westchester and Dutchess Counties. The Ca-enriched rims in garnets from sample CF-5 are clear evidence of pressure increase in an obvious heating event, and are unequivocally associated with emplacement of the Croton Falls mafic pluton. In the case of forcible intrusion at shallower depths, deformation-mediated textural adjustments might be expected to aid in contact-metamorphic recrystallization. The lack of such apparent deformation and recrystallization in the Croton Falls aureole likely reflects more passive intrusion, in accord with the sill-like form of this body.

Maximum temperatures reached in the Croton Falls contact aureole were likely similar to the peak temperatures reached at the Cortlandt Complex, since both plutons appear to have similar magma compositions. However, based on the difference in magma volume and the evidence of extent of chemical contamination in the two complexes, the widths of aureole zones

reflecting similar temperatures at the two complexes were likely different – considerably wider at the larger Cortlandt Complex. There is evidence that partial melting of the aureole did occur at Croton Falls, based on the absence of potassium feldspar and muscovite from the sample study reported in this paper, but the extent of chemical and physical interaction was probably not nearly as extreme as that at the Cortlandt Complex.

2.6 Conclusions

This study documents the evolution of *P–T* conditions in the northern Appalachians immediately after the Taconic regional metamorphism and before magmatic emplacement, through textural and chemical evidence in a contact metamorphosed sample. High-pressure conditions associated with emplacement of the Croton Falls pluton coincide with previously estimated *P–T* conditions of the Cortlandt Complex. The regional *P–T* 'pre-print' calculated from this study also closely resembles estimates from other studies in the area. This study demonstrates that an increase in thermal energy due to heat input from mafic magma overcame the activation energy of crystallization, permitting contact aureole samples to record multiple stages of an orogenic history. We anticipate that late-orogenic loading may have been widespread in the northern Appalachians at this time, but emphasize that without additional heat input to catalyze a second stage of metamorphic transformation, evidence for this would be sparse or entirely absent. In the absence of a pulse of heating, pervasive fluid infiltration would be required to recrystallize these Taconic assemblages, leaving the observer with a suite of ambiguous, partly retrogressed metamorphic rocks.

2.7 Acknowledgements

We would like to thank Adam Henry for collecting sample CF-5 and Kim Waldron for laying the foundation and inspiration to continue investigating this area. We would like to thank Doug Tinkham, Pavel Pitra and Joseph Pyle for detailed and constructive reviews, and Michael Brown for supportive editorial handling.

2.8 References

Balk, R., 1927, Die primare strukture des noritmassivs von Peekskill am Hudson: Neues Jahrb. Mineralogie, **51**, p. 249-303.

Bender, J.F., 1980. Petrogenesis of the Cortlandt Complex. PhD Dissertation, State University of New York, Stony Brook.

Bender, J.F., Hanson, G.N. & Bence, A.E., 1984. Cortlandt Complex; differentiation and contamination in plutons of alkali basalt affinity. American Journal of Science (1880), **284**, 1-57.

Bowen, N.L., 1956. The evolution of igneous rocks. New York, Dover Publications, Inc.

Brock, P.C. & Brock, P.W.G., 1998. Taconian-aged granulite facies metamorphism in the Manhattan Prong, NY and CT. Geology of Long Island and Metropolitan New York, Department of Geosciences, SUNY Stony Brook, 28-30.

Caddick M.J., Konopásek J. & Thompson A.B., 2010. Preservation of garnet growth zoning and the duration of prograde metamorphism. Journal of Petrology, **51**, 2327-2347.

Chen, Y., 2009. The *P-T-t* history of a Barrovian sequence in Dutchess County, New York, and the adjacent part of Connecticut. MS thesis, University of Maryland, College Park.

Dallmeyer, R.D., 1975. $^{40}Ar/^{39}Ar$ release spectra of biotite and hornblende from the Cortlandt and Rosentown plutons, New York, and their regional implications. Journal of Geology, **83**, 629-643.

Dana, J.D., 1881. The geological realtions of the limestone belts of Westchester County, New York. American Journal of Science (1880), **22**, 103-119.

Dana, J.D., 1884. Note on the Corlandt and Stony Point hornblendic and augitic rock (New York). American Journal of Science (1880), **28**, 384-386.

Dorfler, K.M., Tracy, R.J., Caddick, M.J., 2012, Melting of metapelitic xenoliths in mafic magma, melt removal, and residuum formation at 0.8 GPa. Geological Society of America Abstracts with Programs, **44**, n 7.

England P.C. & Thompson A.B., 1984. Pressure-temperature-time paths of regional metamorphism I. Heat transfer during the evolution of regions of thickened continental crust. Journal of Petrology, **25**, 894-928.

Ferry, J.M. & Spear, F.S., 1978. Experimental calibration of the partitioning of Fe and Mg between biotite and garnet. Contributions to Mineralogy and Petrology, **66**, 113-117.

Fisher, D.W., Isachsen, Y.W. & Rickard, L.V., 1970. Bedrock geologic map of New York. New York State Museum and Science Service, Scale 1:125,000.

Friedman, G.M., 1954. The spinel-silica reaction succession; a study of incompatible mineral phases. Journal of Geology, **62**, 366-374.

Friedman, G.M., 1956. The origin of spinel-emery deposits, with particular reference to those of the Cortlandt Complex, New York. New York State Museum Bulletin, **351**, 1-68.

Hall, L.M., 1968. Times of origin and deformation of bedrock in the Manhattan Prong. E. Zen and others, Eds., Studies of Appalachian Geology: Northern and Maritime. John Wiley and Sons, 117-127.

Hames, W.E., Tracy, R.J., Ratcliffe, N.M. & Sutter, J.F., 1991. Petrologic, structural and geochronologic characteristics of the Acadian metamorphic overprint on the Taconide zone in part of southwestern New England. American Journal of Science, **291**, 887-913.

Henry, A., 1997. Petrologic and fluid inclusion constraints on the tectonic evolution of the Manhattan Prong, Southeastern New York. MS thesis, Virginia Polytechnic Institute and State University.

Hibbard, J.P., van Staal, C., Rankin, D. & Williams, H., 2006. Geology, Lithotectonic Map of the Appalachian Orogen (South), Canada-United States of America. Geological Survey of Canada, Map 02096A, scale 1:1500000.

Hodges, K.V. & Spear, F.S., 1982. Geothermometry, geobarometry and the Al_2SiO_5 triple point at Mt. Moosilauke, New Hampshire. American Mineralogist, **67**, 1118-1134.

Holdaway, M.J. & Lee, S.M., 1977. Fe-Mg cordierite stability in high grade pelitic rocks based on experimental, theoretical and natural observations. Contributions to Mineralogy and Petrology, **63**, 175-198.

Holland, T.J.B. & Powell, R., 2003. Activity-composition relations for phases in petrological calculations: an asymmetric multicomponent formulation. Contributions to Mineralogy and Petrology, **145**, 492-501.

Johnson, A.M. & Tracy, R.J., 1998. Textural and chemical relations among spl-spr-grt-opx, Salt Hill emery mine, Cortlandt Complex, N.Y. Eos (Richmond, Va.), **79**, 360.

Johnson, A.M. & Tracy, R.J., 1999. Textural and chemical relations among spinel-sapphirine-garnet-orthopyroxene, Salt Hill emery mine, Cortlandt Complex, NY. Geological Society of America Abstracts with Programs, **31**, 40.

Koziol, A.M., 1989. Recalibration of the garnet-plagioclase- Al_2SiO_5-quartz (GASP) geobarometer and application to natural parageneses. American Geophysical Union Spring Meeting, Baltimore, Maryland, EOS, **70**, 493.

Koziol, A.M. & Newton, R.C., 1988. Redetermination of the anorthite reaction and improvement of the plagioclase-garnet-Al_2SiO_5-quartz barometer. American Mineralogist, **73**, 216-223.

Long, L.E. & Kulp, J.L., 1962. Isotopic age study of the metamorphic history of the Manhattan and Reading Prongs. Geological Society of America Bulletin, **73**, 969-996.

Perchuck, L.L. & Lavrent'eva, I.V., 1983. Experimental investigation of exchange equilibria in the system cordierite-garnet-biotite. S.K. Saxena Ed., Kinetics and Equilibrium in Mineral Reaction, Springer Verlag, Berlin, 199-239.

Perchuck, L.L., Podlesskii, K.K. & Aranovich, L.Y., 1991. Thermodynamics of some framework silicates and their equilibria: application to geothermobarometry. L.L. Perchuck, Ed., Progress in Metamorphic and Magmatic Petrology, A Memorial Volume in Honor of D.S. Korzhinsky, Cambridge University Press, Cambridge, 131-164.

Pouchou, J.-L. & Pichoir, F., 1984. A new model for quantitative X-ray microanalysis; Part I: application to the analysis of homogeneous samples. La Recherche Aerospatiale, **3**, 13-38.

Powell, R. & Holland, T.J.B., 1988. An internally consistent dataset with uncertainties and correlations: 3. Applications to geobarometry, worked examples and a computer program. Journal of Metamorphic Geology, **6**, 173-204.

Powell, R. & Holland, T.J.B., 1994. Optimal geothermometry and geobarometry. American Mineralogist, **79**, 120-133.

Powell, R. & Holland, T.J.B., 2008. On Thermobarometry. Journal of Metamorphic Geology, **26**, 155-179.

Powell, R., Holland, T.J.B. & Worley, B., 1998. Calculating phase diagrams with THERMOCALC: methods and examples. Journal of Metamorphic Geology, **16**, 577-588.

Ratcliffe, N.M., 1970. Ancient strike-slip fault tectonics in the Hudson Highlands and Manhattan Prong. Transactions New York Academy of Sciences, ser. 2, **32**, 1009-1021.

Ratcliffe, N.M., Armstrong, R.L., Mose, D.G., Seneschal, R., Williams, N. & Baiamonte, M.J., 1982. Emplacement history and tectonic significance of the Cortlandt Complex, related plutons, and dike swarms in the Taconide Zone of southeastern New York based on K-Ar and Rb-Sr investigations. American Journal of Science (1880), **282**, 58-390.

Ratcliffe, N.M., Bender, J.F. & Tracy, R.J., 1983. Tectonic setting, chemical petrology and petrogenesis of the Cortlandt Complex and related rocks of southeastern New York State: Guidebook for field trip 1. Northeastern Section, Geological Society of America Meeting, Kiamesha Lake, New York, 1-101.

Ratcliffe, N.M., Hames, W.E. & Stanley, R.S., 1998. Interpretation of ages of arc magmatism, metamorphism, and collisional tectonics in the Taconian Orogen of western New England. American Journal of Science (1880), **298**, 791-797.

Rogers, G.S., 1911. Geology of the Cortlandt Series and its emery deposits. New York Academy of Science Annals, **21**, 11-86.

Spear, F.S. & Kohn, M.J., 1996. Trace element zoning in garnet as a monitor of crustal melting. Geology, **24**, 1099-1102.

Spear, F.S. & Parrish, R.R., 1996. Petrology and cooling rates of the Valhalla Complex, British Columbia, Canada. Journal of Petrology, **37**, 733-763.

Spear, F.S., Kohn, M.J. & Cheney, J.T., 1999. *PT*-Paths from anatectic pelites. Contributions to Mineralogy and Petrology, **134**, 17-32.

Stanley, R.S. & Ratcliffe, N.M., 1985. Tectonic synthesis of the Taconian Orogeny in western New England. Geological Society of America Bulletin, **96**, 1227-1250.

Sutter, J.F., Ratcliffe, N.M. & Mukasa, S.B., 1985. $^{40}Ar/^{39}Ar$ and K-Ar data bearing on the metamorphic and tectonic history of western New England. Geological Society of America Bulletin, **96**, 123-136.

Thompson, A.B., 1976. Mineral reactions in pelitic rocks: II. Calculation of some *P-T-X* (Fe-Mg) phase relations. Americal Journal of Science, **276**, 425-4454

Tracy, R.J. & McLellan, E.L., 1985. A natural example of the kinetic controls of compositional and textural equilibration. A.B. Thompson and D.C. Rubie, Eds., Metamorphic reactions; kinetics, textures, and deformation, **4**, 118-137.

Waldron, K.A., 1986. High pressure contact metamorphism in the aureole of the Cortlandt Complex, southeastern New York. PhD Dissertation, Yale University.

White, R.W., Powell, R. & Holland, T.J.B., 2007. Progress relating to calculation of partial melting equilibria for metapelites. Journal of Metamorphic Geology, **25**, 511-527.

Whitney, D.L., Mechum, T.A., Kuehner, S.M. & Dilek, Y.R., 1996. Progressive metamorphism of pelitic rocks from protolith to granulite facies, Dutchess County, New York, USA; constraints on the timing of fluid infiltration during regional metamorphism. Journal of Metamorphic Geology, **14**, 163-181.

Williams, G.H., 1887. The norites of the "Cortlandt Series" on the Hudson River near Peekskill, New York. American Journal of Science, 3d series, **33**, 135-144 and 191-199.

Williams, G.H., 1888. The contact metamorphism produced in the adjoining mica schists and limestones by the massive rocks of the "Cortlandt Series" near Peekskill, New York. American Journal of Science, 3d series, **36**, 254-269.

Williams, M.L. & Grambling, J.A., 1990. Manganese, ferric iron and the equilibrium between garnet and biotite. American Mineralogist. **75**, 886-908.

2.9 Figures

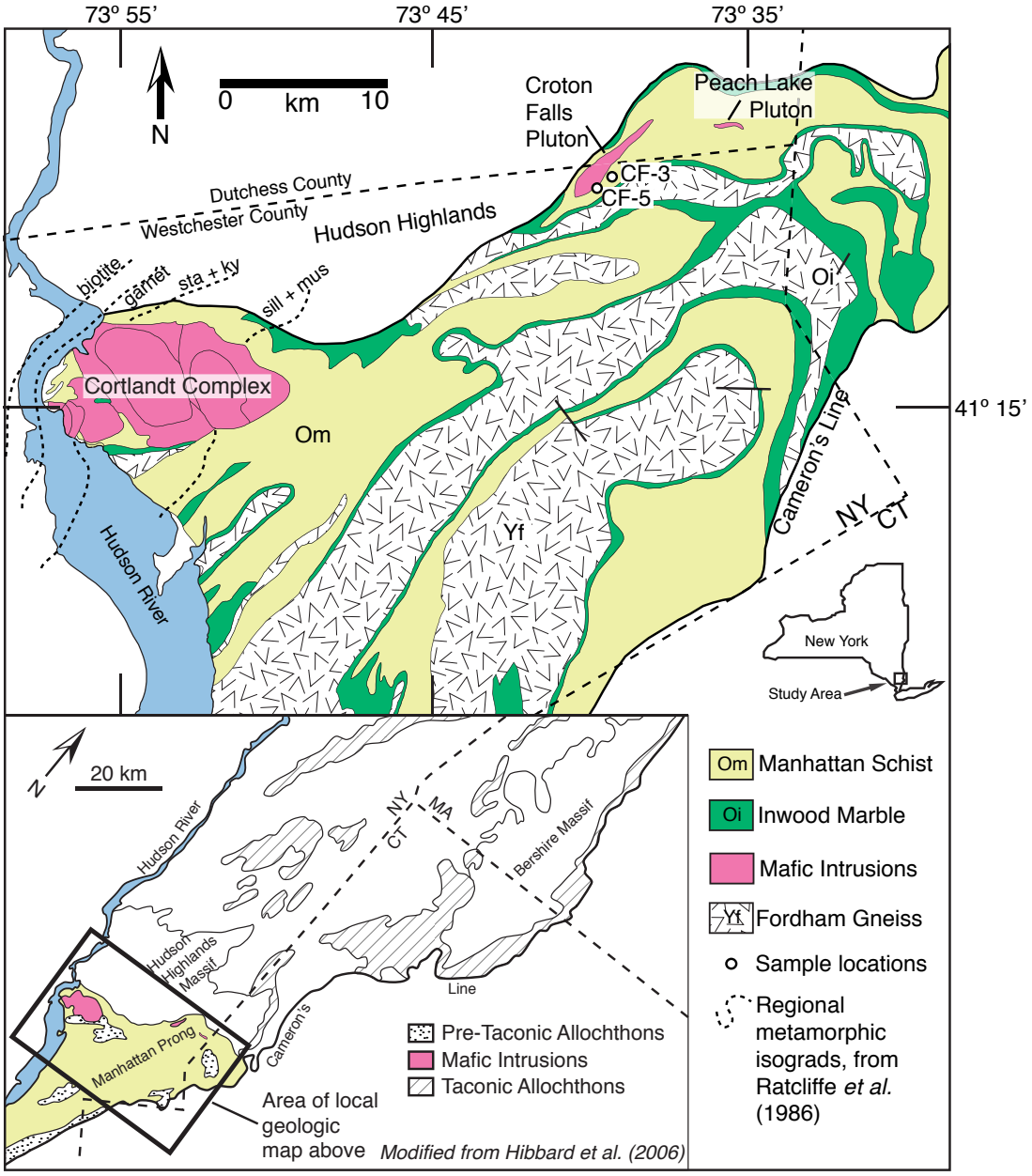

Figure 2.1. Simplified geologic map of the study area. Top panel shows the entire upper Manhattan Prong, including the Cortlandt Complex with regional isograds from Ratcliffe et al. (1983). The dotted line denotes the boundaries of the state of New York (NY) and Connecticut (CT) as well as the counties of Westchester and Dutchess. CF-5 is the sample analyzed in this paper. CF-3 is a contact metamorphosed sample that lies farther from the contact and did not develop spinel or the high-Ca plagioclase and garnet overgrowths described for CF-5. Lower insert is a simplified geologic map illustrating the presence of Taconic allochthons in the area north of the Manhattan Prong, west of Cameron's Line. Deeper erosion in the south exposes the mafic intrusions (and adjacent country rock) emplaced under the allochtons.

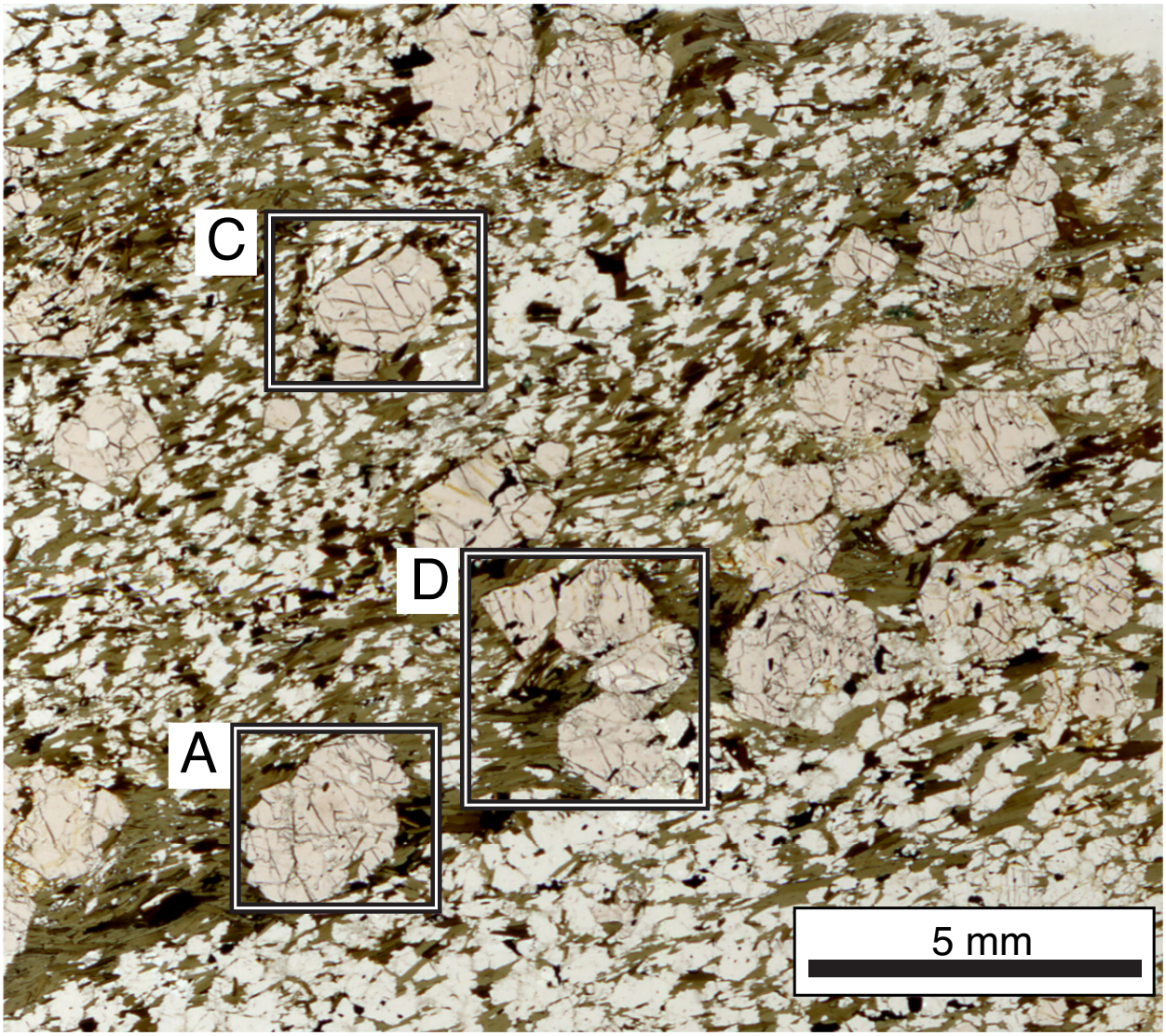

Figure 2.2. Photomicrograph of part of the CF-5 thin section used in the study. Labeled boxes correspond to garnets A, C, and D.

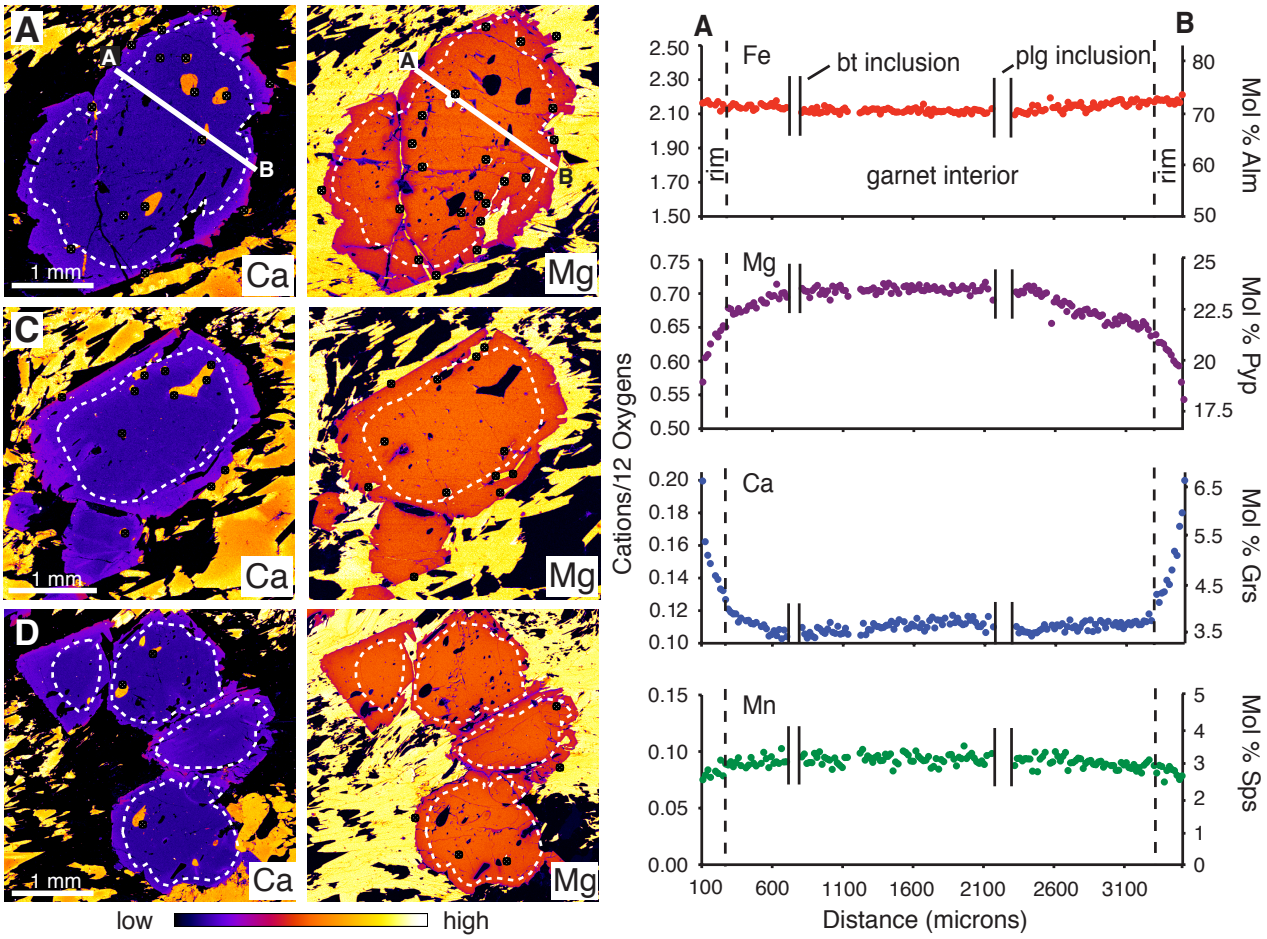

Figure 2.3. Ca and Mg X-Ray maps of garnets A, C, and D. Color scale is proportional to the elemental concentration. White dotted lines demarcate the boundary between the low Ca interior of crystals and the Ca-enriched rim zones. Yellow inclusions in the Ca map are plagioclase, white inclusions in Mg map are biotite. Black and white points on the Ca maps indicate where each plagioclase-garnet pair analysis was taken. Points on the Mg maps indicate where each biotite-garnet pair analysis was taken. Note Ca zoning in matrix plagioclase in the Ca-map of garnet C. White line in garnet A corresponds to the traverse shown to right, showing the abundance of major cations (measured on a 12-oxygen basis). Vertical dotted lines on traverse correspond to the boundary between the garnet interior and Ca-enriched rims. Short solid vertical lines denote inclusions in the garnet where chemical data has been omitted. Note that there is minimal change in Fe and Mn content across the garnet. Mg and Ca content changes abruptly at the border between the garnet interior and rim.

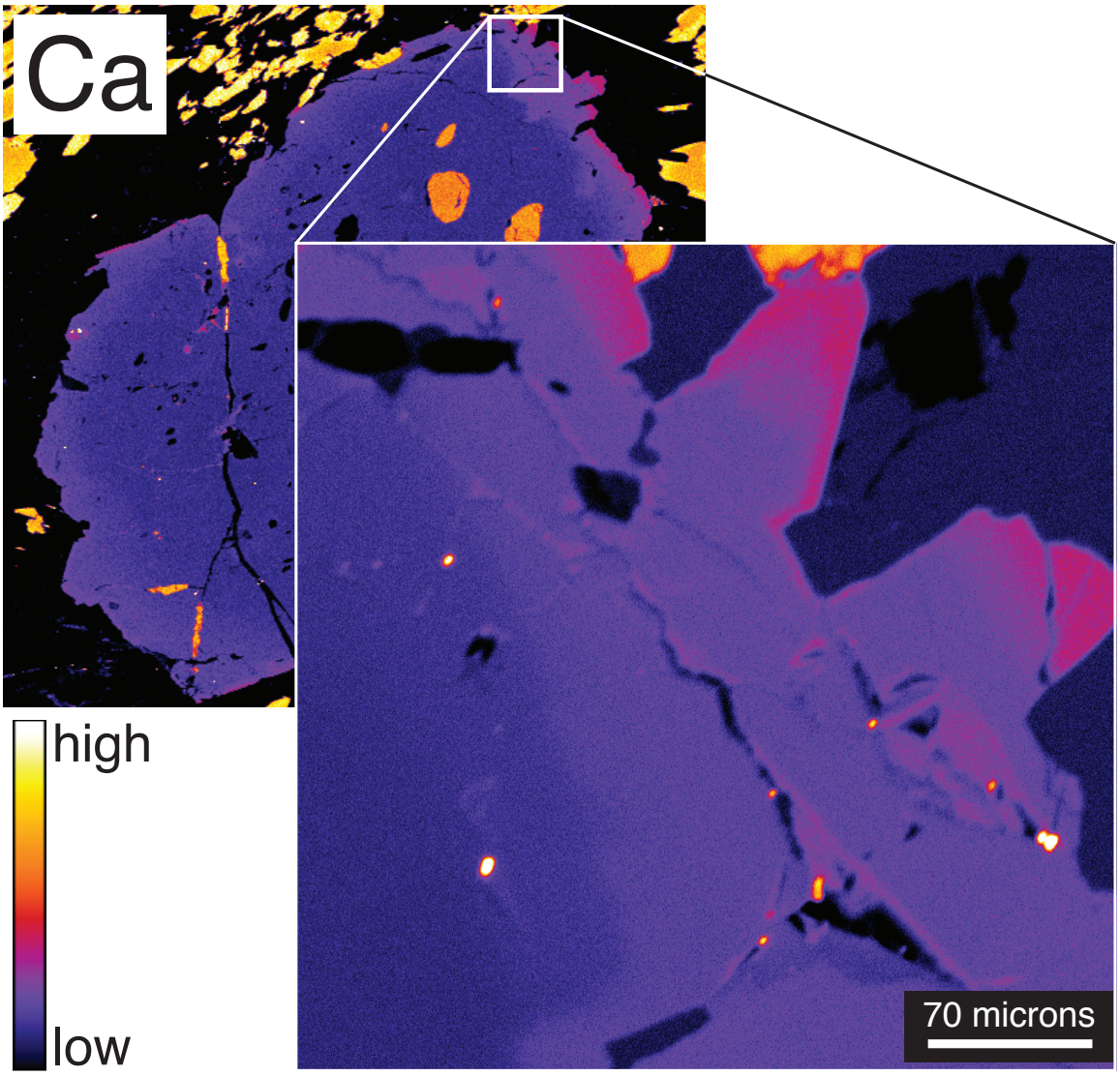

Figure 2.4. Detail of the Ca-enriched rim zone of garnet A. A thin zone of very Ca-enriched garnet is present at the very edge of the porphyroblast. An intermediate zone of Ca-enriched garnet (relative to the interior composition) makes up the majority of the garnet rim.

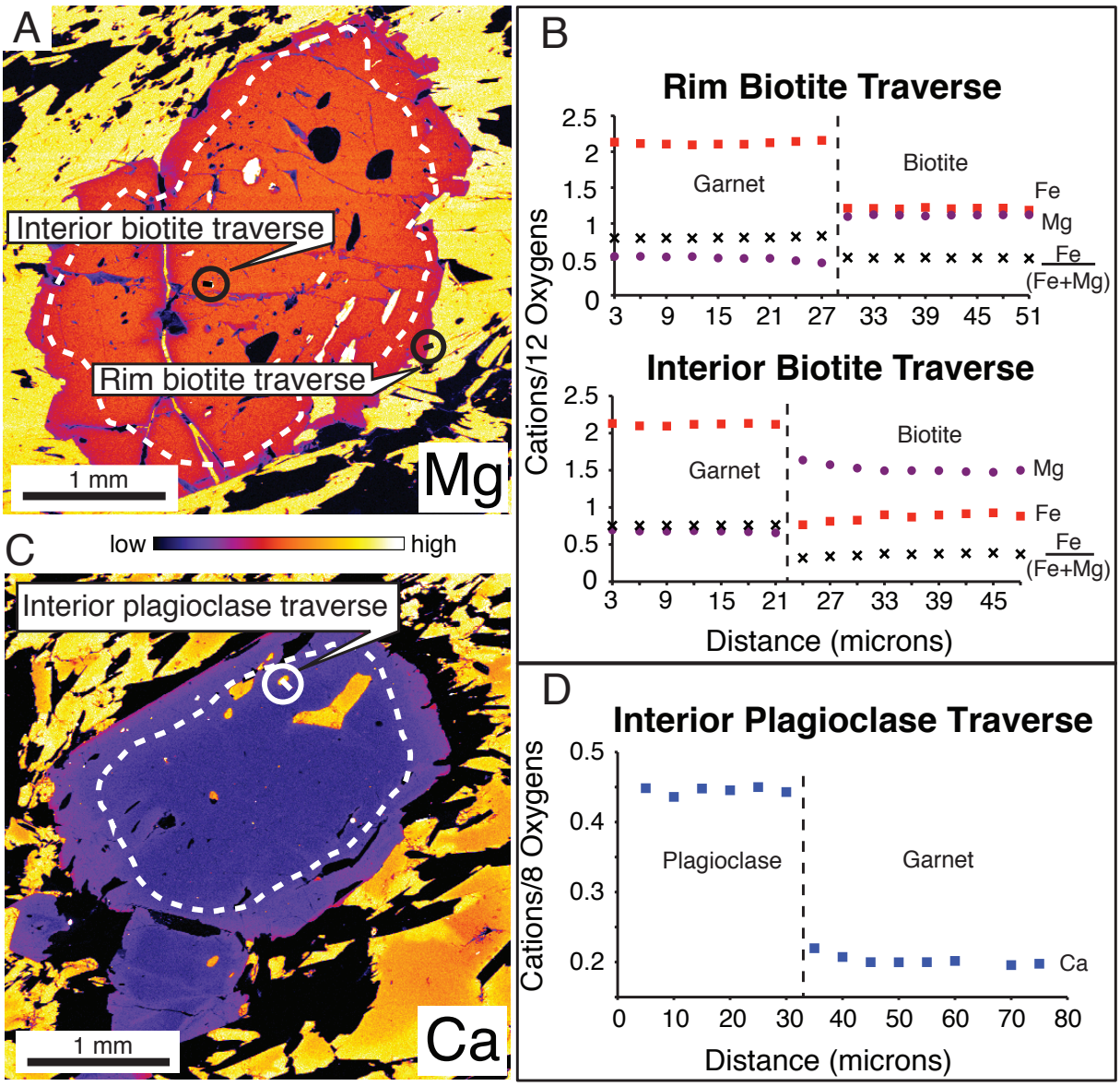

Figure 2.5. Panel (a) and (b) Representative traverses across biotite-garnet boundaries from the interior and Ca-enriched rim zone of garnet A. The rim biotite traverse shows minimal zoning in the Fe content of either biotite or garnet. A slight decrease in Mg content is present in garnet next to the inclusion. The interior biotite traverse shows slight increase in Mg content and decrease in Fe content in the biotite inclusion toward the garnet boundary. Panel (c) and (d) Example of a typical traverse across an interior plagioclase-garnet boundary from garnet C. Minimal Ca zoning is present in the garnet adjacent to the plagioclase inclusion.

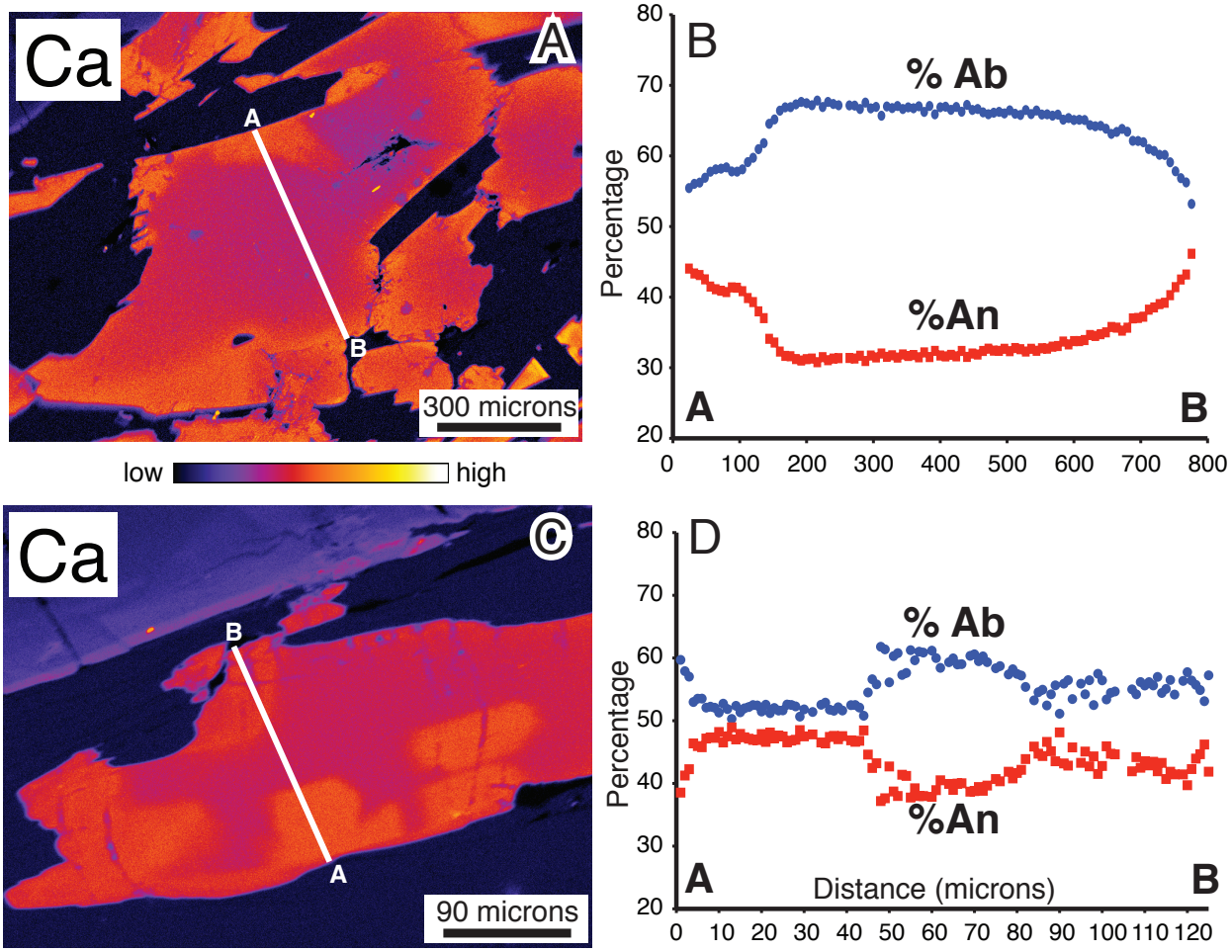

Figure 2.6. Ca chemical maps and traverses across matrix plagioclase. (a) matrix plagioclase with relatively patchy Ca-enriched zones on the edges of the crystal. (b) traverse across plagioclase in panel A. The plagioclase varies from An_{48} to An_{30}. (c) matrix plagioclase with very patchy Ca-enriched zones. (d) traverse across plagioclase in panel C. Composition varies from An_{49} to An_{36}.

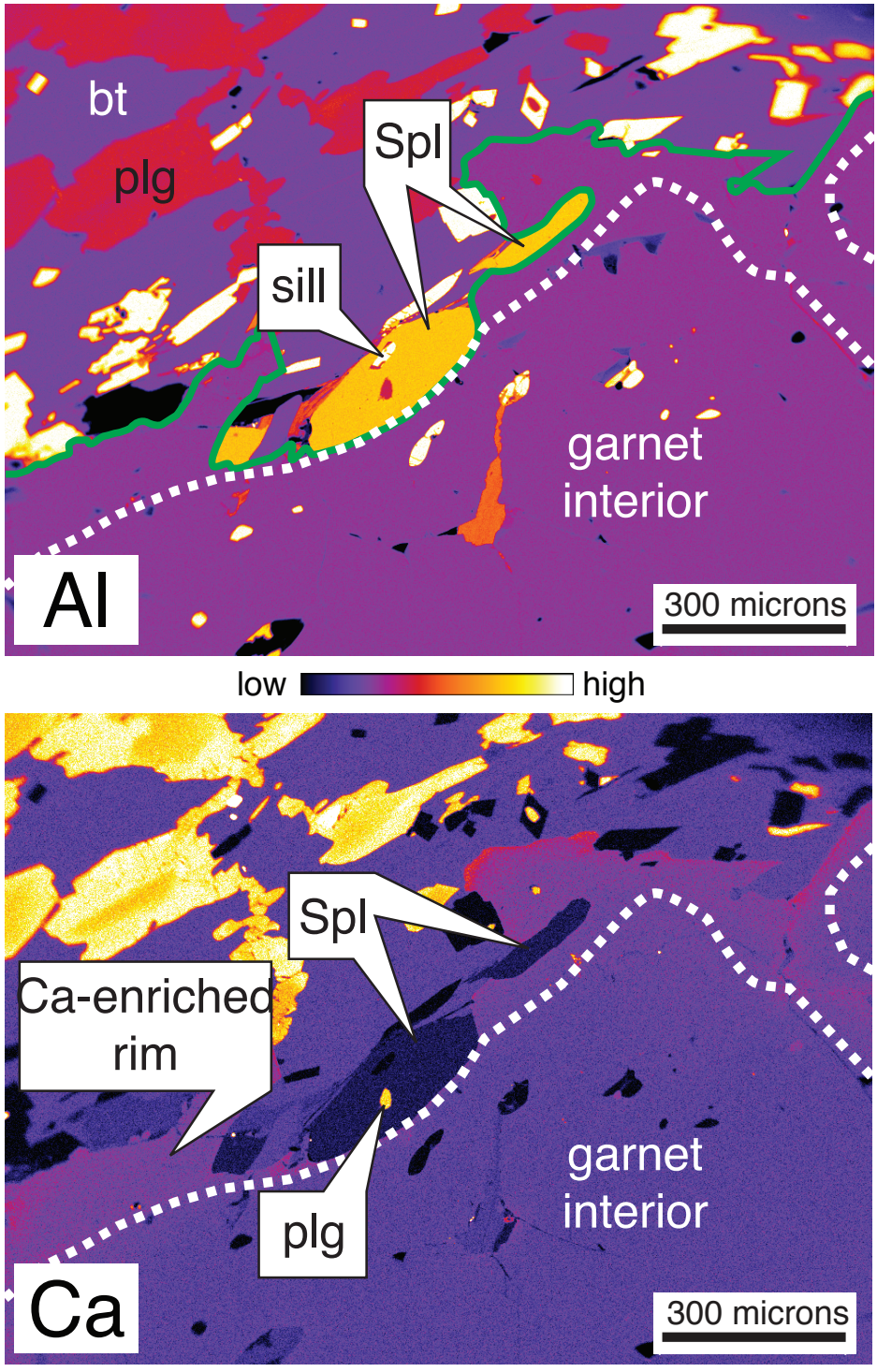

Figure 2.7. EDS chemical images of spinel crystals in the Ca-enriched rim zone of a garnet. The larger spinel crystal has inclusions of plagioclase and sillimanite (see Table 2.5 for chemical analyses of spinel and plagioclase). Note the Ca-zoning in matrix plagioclase in the Ca chemical map.

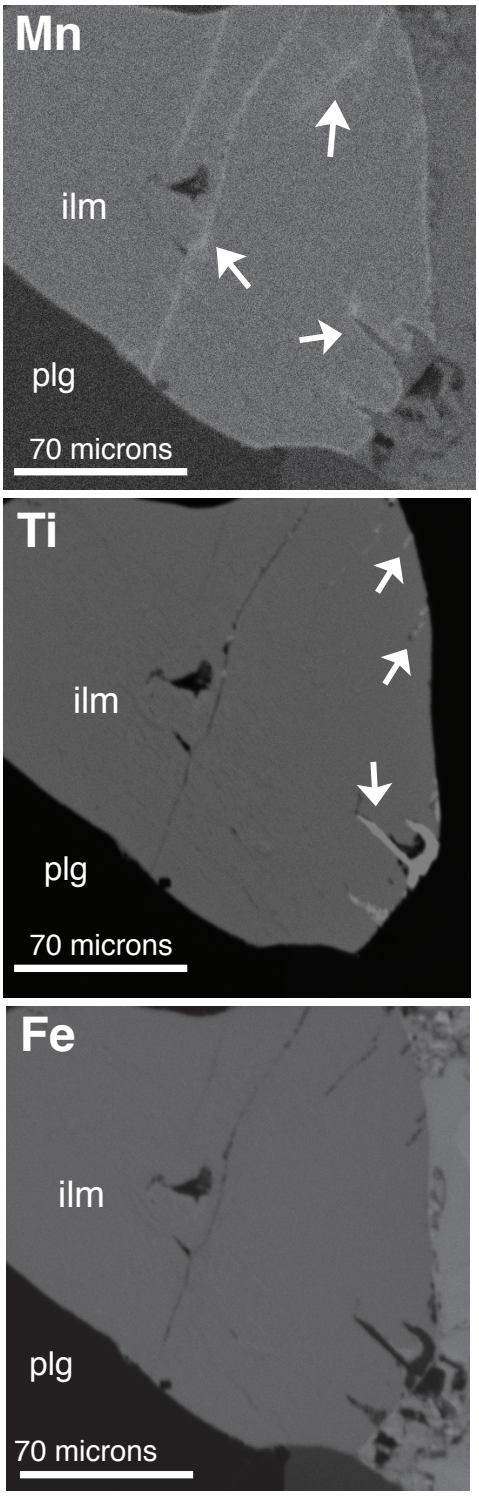

Figure 2.8. Rutile replacement of ilmenite in the matrix. Arrows in the Mn map highlight an increase in Mn content in the cracks of ilmenite and along the boundary between the rutile fingers and ilmenite. Arrows in the Ti map point to the rutile replacement.

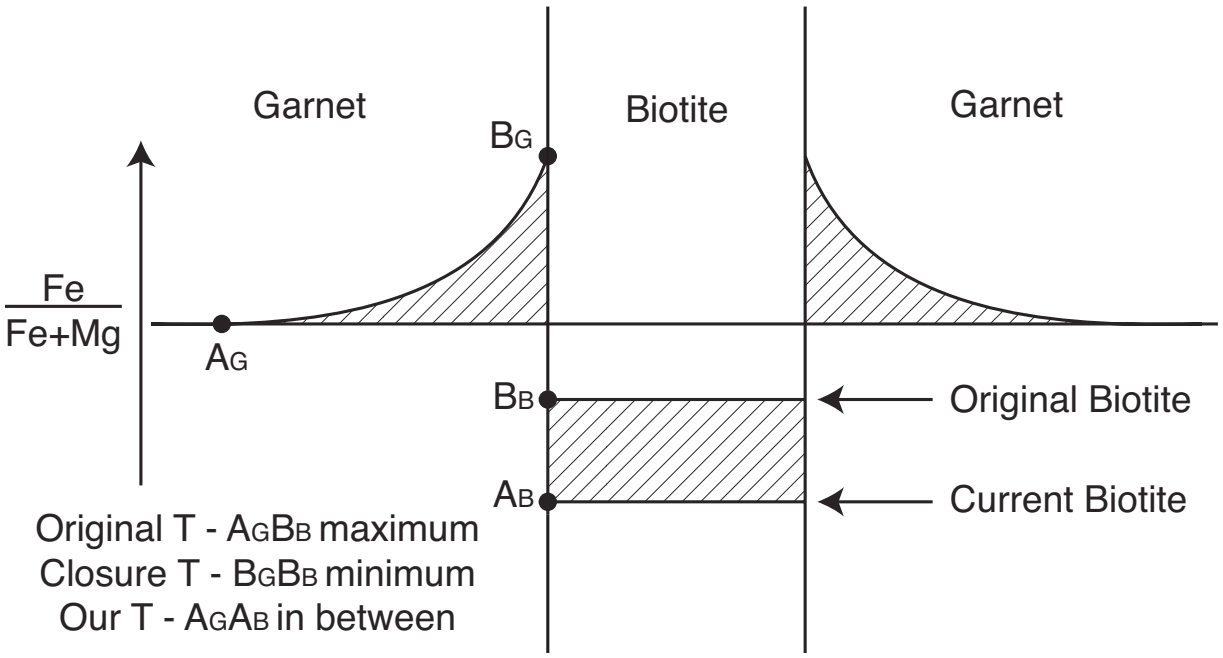

Figure 2.9. Schmatic illustration of garnet-biotite diffusion profiles and our integration method for choosing the appropriate chemical composition to do thermobarometric calcuations. The area underneath the diffusion curve in the garnet is the same as the area between the difference in Fe/Fe+Mg in the biotite inclusion (See Figure 10 in Spear and Parrish, 1996).

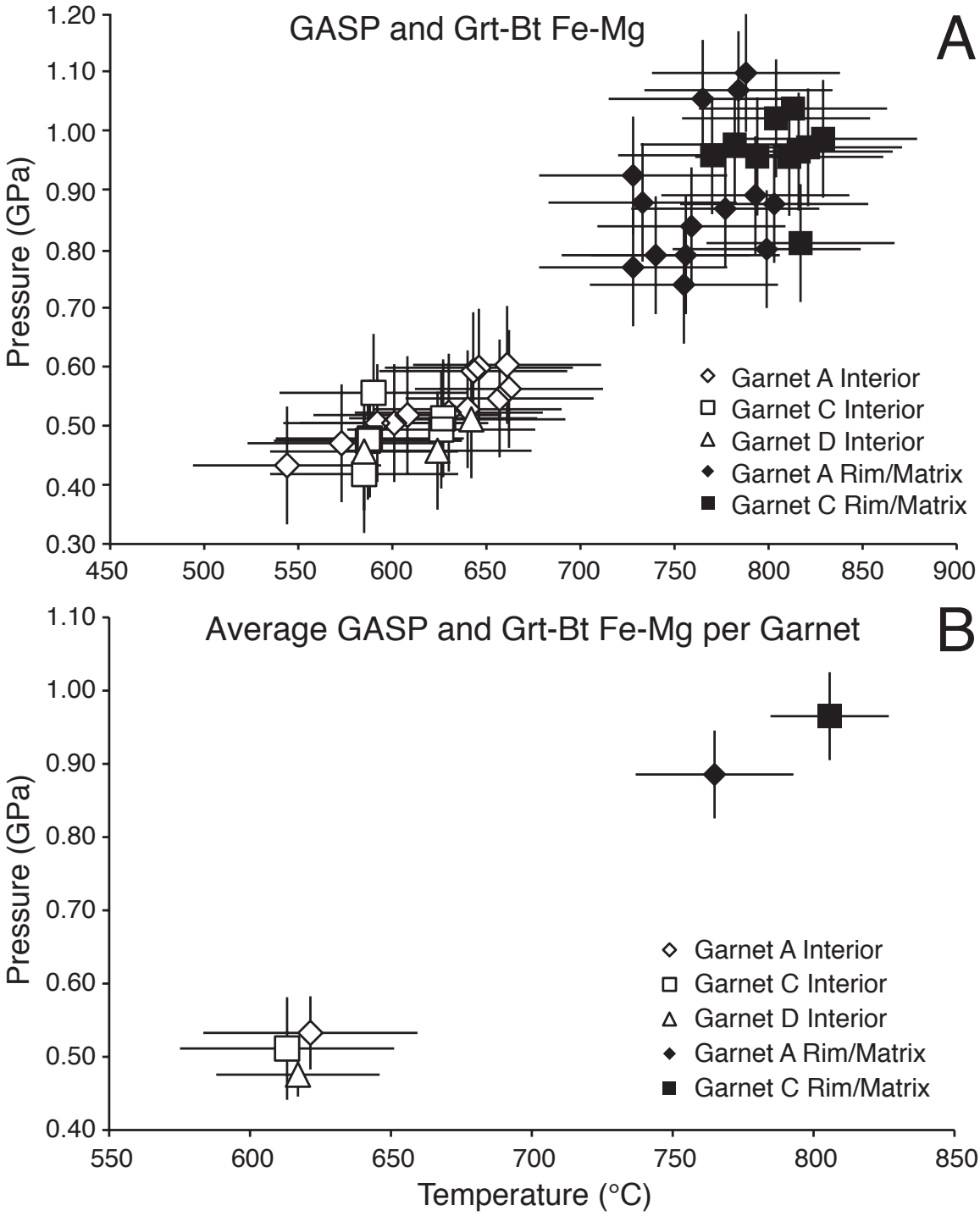

Figure 2.10. GASP and Grt-Bt Fe-Mg results. Panel (a) coupled garnet-biotite thermometry and GASP barometry for each analyzed garnet-biotite-plagioclase sub-assemblage from three garnet porphyroblasts. Error bars represent an arbitary calibration uncertainty of ± 50 ˚C and ± 1 kbar. Panel (b) averaged *PT* values from interior and rim sub-assemblages for each garnet porphyroblast. Error bars represent scatter in data set, without incorporating the minimal 'thermodynamic uncertainties' shown in panel (a). Results are also listed in Table 2.6.

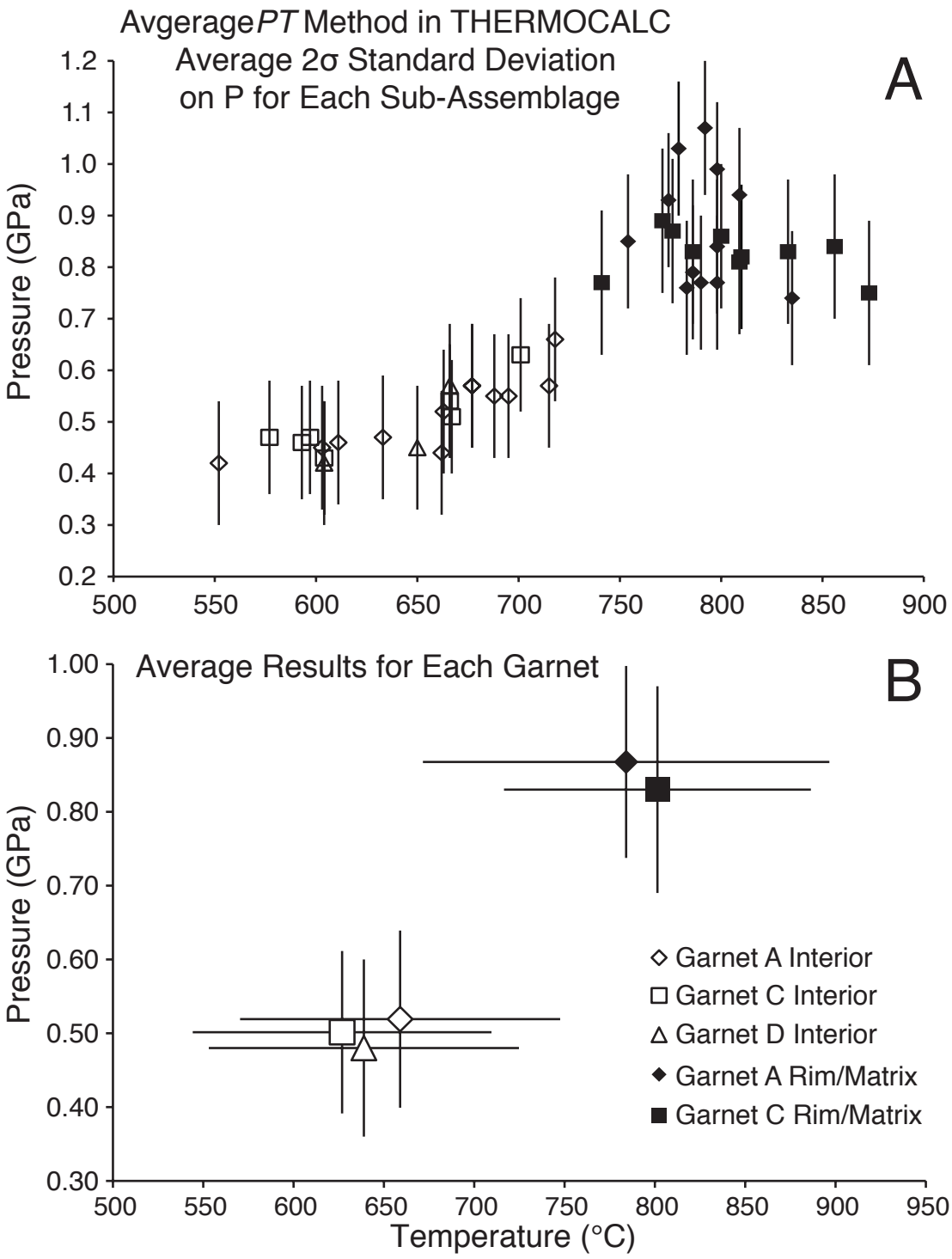

Figure 2.11. Average*PT* method in THERMOCALC. Panel (a) *PT* values for each garnet-biotite-plagioclase sub assemblage calculated with the Average*PT* method in THERMOCALC. Temperature values were assumed as known so that only 2σ uncertainly in *P* is shown (see text for details). Panel (b) averaged *PT* values from each domain of each garnet crystal. Error bars represent standard deviation of scatter of *PT* data, without incorporating the thermodynamic uncertainty from panel (a).

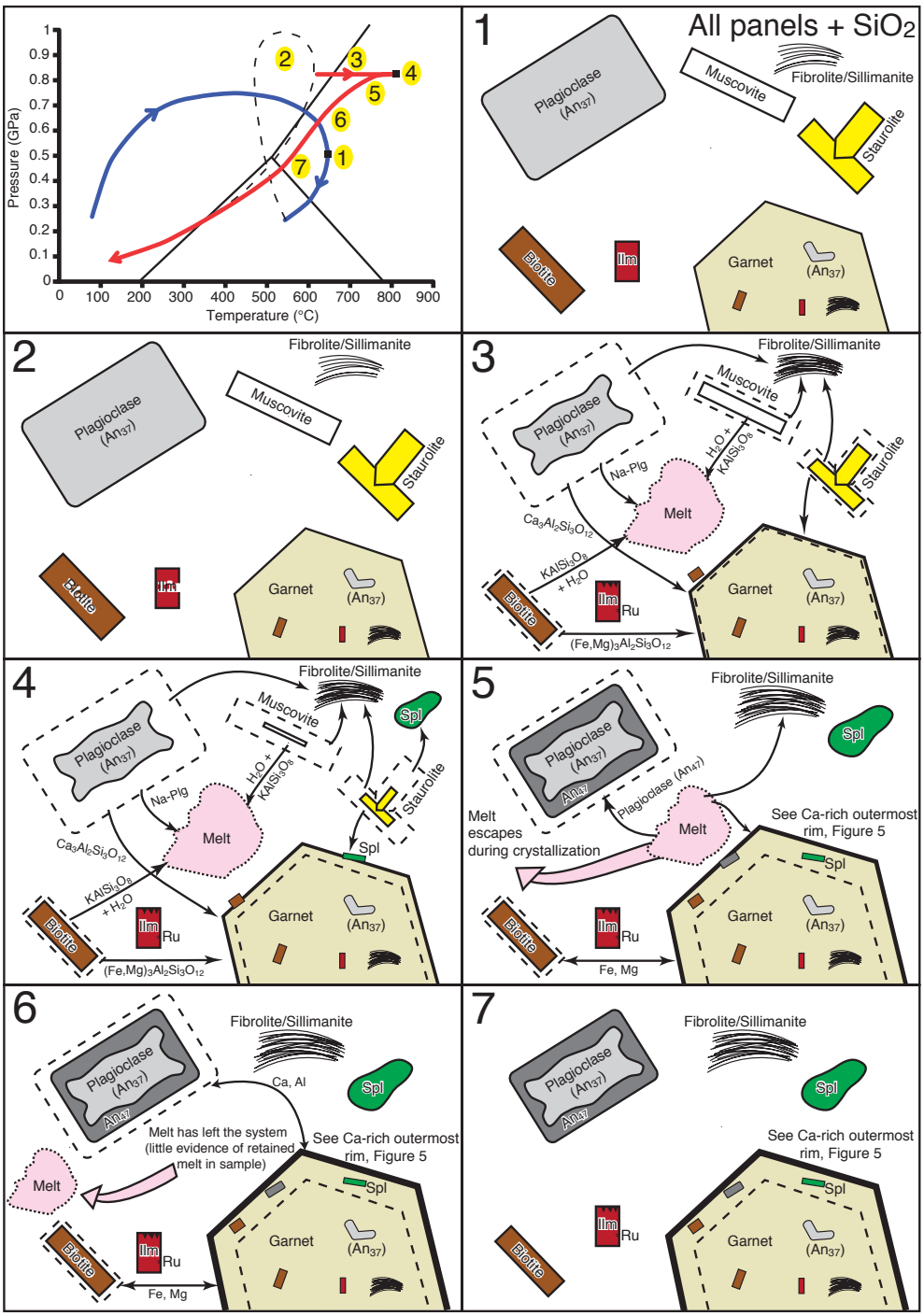

Figure 2.12. Schematic *PT* history and proposed textural development of CF-5. Panels 1–7 reflect the textural development of the sample and correspond to the numbered stages on the *PT* path. Dotted path in *PT* diagram is the schematic representation of the emplacement of thrust sheets and doesn't signify actual path between point 1 and 4. See section *Summary of P-T History and Textural Development* of text for discussion of these tectonic and micro textural stages.

2.10 Tables

	Pl			Bt			Grt	
	Interior (7)	Rim (6)		Interior (12)	Rim (11)		Interior (19)	Rim (17)
SiO_2	60.87	59.72	SiO_2	36.69	36.17	SiO_2	39.10	38.94
TiO_2	-	-	TiO_2	3.16	3.34	TiO_2	0.03	0.02
Al_2O_3	25.17	26.29	Al_2O_3	18.71	18.36	Al_2O_3	21.90	21.86
FeO	0.40	0.49	FeO	15.20	19.09	FeO	32.50	33.61
MnO	-	-	MnO	0.04	0.03	MnO	1.39	1.20
MgO	0.00	0.00	MgO	12.86	9.67	MgO	5.64	4.60
CaO	7.04	7.80	CaO	0.01	0.01	CaO	1.44	2.26
Na_2O	7.15	6.92	Na_2O	0.26	0.12	Na_2O	-	-
K_2O	0.38	0.12	K_2O	9.06	9.29	K_2O	-	-
Total	101.01	101.34	Total	95.99	96.07	Total	102.00	102.49
Si	2.69	2.63	Si	2.71	2.72	Si	3.02	3.02
Al	1.31	1.37	Al^{IV}	1.29	1.28	Al^{VI}	1.99	2.00
Fe^{2+}	0.01	0.02	Al^{VI}	0.33	0.35	Fe^{2+}	2.10	2.18
Ca	0.33	0.37	Ti	0.18	0.19	Mn	0.09	0.08
Na	0.61	0.59	Fe^{2+}	0.94	1.20	Mg	0.65	0.53
K	0.02	0.01	Mn	0.00	0.00	Ca	0.12	0.19
			Mg	1.41	1.08			
			Na	0.04	0.02	X_{Alm}	70.97	73.21
Or	2.20	0.71	K	0.89	1.91	X_{Prp}	21.93	17.86
Ab	63.31	61.16				X_{Sps}	3.07	2.64
An	34.49	38.13	Fe/(Fe+Mg)	0.40	0.53	X_{Grs}	4.03	6.29
An/(Ab+An)	35.27	38.40	Mg/(Mg+Fe)	0.60	0.47	Fe/(Fe+Mg)	0.76	0.80

Plagioclase cations calculated on an 8-oxygen basis, biotite cations calculated on an 11-oxygen equivalent basis, garnet cations calculated on a 12-oxygen basis

Table 2.1. Average compositions of garnet A and its inclusions

	Pl			Bt			Grt	
	Interior (9)	Rim (4)		Interior (3)	Rim (10)		Interior (12)	Rim (14)
SiO_2	58.97	58.36	SiO_2	36.51	35.94	SiO_2	38.73	38.74
TiO_2	-	-	TiO_2	3.28	3.30	TiO_2	0.02	0.02
Al_2O_3	26.37	26.65	Al_2O_3	18.58	18.33	Al_2O_3	21.96	21.78
FeO	0.44	0.16	FeO	15.46	19.24	FeO	33.32	33.68
MnO	-	-	MnO	0.03	0.03	MnO	1.30	1.13
MgO	0.00	0.00	MgO	12.34	9.90	MgO	5.38	5.04
CaO	8.29	8.70	CaO	0.02	0.01	CaO	1.79	1.90
Na_2O	6.58	6.43	Na_2O	0.17	0.12	Na_2O	-	-
K_2O	0.22	0.15	K_2O	9.62	9.56	K_2O	-	-
Total	100.87	100.45	Total	96.01	96.42	Total	102.50	102.29
Si	2.62	2.60	Si	2.70	2.70	Si	2.99	3.00
Al	1.38	3.40	Al^{IV}	1.30	1.30	Al^{VI}	2.00	1.99
Fe	0.02	0.01	Al^{VI}	0.33	0.32	Fe^{2+}	2.15	2.16
Ca	0.39	0.42	Ti	0.18	0.19	Mn	0.08	0.08
Na	0.57	0.55	Fe^{2+}	0.96	1.21	Mg	0.62	0.62
K	0.01	0.01	Mn	0.00	0.00	Ca	0.15	0.15
			Mg	1.36	1.11			
			Na	0.02	0.02	X_{Alm}	71.67	71.94
Or	1.25	0.91	K	0.91	0.92	X_{Prp}	20.61	20.52
Ab	58.23	56.66				X_{Sps}	2.90	2.69
An	40.53	42.43	Fe/(Fe+Mg)	0.41	0.52	X_{Grs}	4.90	4.90
An/(Ab+An)	41.04	42.82	Mg/(Mg+Fe)	0.59	0.48	Fe/(Fe+Mg)	0.78	0.78

Plagioclase cations calculated on an 8-oxygen basis, biotite cations calculated on a 11-oxygen equivalent basis, garnet cations calculated on a 12-oxygen basis

Table 2.2. Average compositions of garnet C and its inclusions

	Plg		Bt			Grt	
	Interior (5)		Interior (3)	Rim (2)		Interior (7)	Rim (2)
SiO_2	58.82	SiO_2	36.40	36.73	SiO_2	38.62	39.68
TiO_2	-	TiO_2	3.34	3.22	TiO_2	0.02	0.02
Al_2O_3	26.08	Al_2O_3	18.63	18.84	Al_2O_3	21.48	22.27
FeO	0.42	FeO	15.37	20.28	FeO	33.48	35.85
MnO	-	MnO	0.03	0.05	MnO	1.19	1.21
MgO	0.00	MgO	12.57	9.87	MgO	5.48	4.66
CaO	7.96	CaO	0.01	0.02	CaO	1.65	1.89
Na_2O	6.93	Na_2O	0.24	0.18	Na_2O	-	-
K_2O	0.22	K_2O	9.12	9.33	K_2O	-	-
Total	100.43	Total	95.72	98.52	Total	101.92	105.58
Si	2.62	Si	2.70	2.71	Si	2.99	2.99
Al	1.37	Al^{IV}	1.30	1.29	Al^{VI}	2.00	1.98
Fe	0.02	Al^{VI}	0.34	0.35	Fe^{2+}	2.17	2.27
Ca	0.38	Ti	0.19	0.18	Mn	0.08	0.08
Na	0.60	Fe^{2+}	0.96	1.25	Mg	0.63	0.53
K	0.01	Mn	0.00	0.00	Ca	0.13	0.15
		Mg	1.39	1.09			
		Na	0.04	0.03	X_{Alm}	72.16	75.00
Or	1.24	K	0.86	0.88	X_{Prp}	20.98	17.38
Ab	60.39				X_{Sps}	2.60	2.63
An	38.37	Fe/(Fe+Mg)	0.41	0.53	X_{Grs}	4.26	5.06
An/(Ab+An)	38.85	Mg/(Mg+Fe)	0.59	0.47	Fe/(Fe+Mg)	0.78	0.81

Plagioclase cations calculated on an 8-oxygen basis, biotite cations calculated on a 11-oxygen equivalent basis, garnet cations calculated on a 12-oxygen basis

Table 2.3. Average compositions of garnet D and its inclusions

	Interior (78)	Rim (17)
SiO_2	60.14 ± 0.81	57.98 ± 0.65
Al_2O_3	24.99 ± 0.52	26.38 ± 0.42
FeO	0.04 ± 0.02	0.12 ± 0.09
CaO	7.23 ± 0.56	8.91 ±0.47
Na_2O	7.86 ±0.32	6.87 ± 0.26
K_2O	0.24 ± 0.05	0.15 ± 0.04
Total	101.26	101.41
Si	2.67 ± 0.03	2.59 ± 0.02
Al	1.31 ± 0.03	1.39 ± 0.02
Fe^{2+}	0.001 ± 0.003	0.005 ± 0.001
Ca	0.34 ±0.03	0.43 ± 0.02
Na	0.68 ± 0.03	0.6 ± 0.02
K	0.013 ± 0.001	0.008 ± 0.001
	1.29 ± 0.29	0.81 ± 0.20
Or	65.45 ± 2.40	57.75 ± 2.06
Ab	33.27 ± 2.63	41.43 ± 2.23
An	33.70 ± 2.58	41.77 ± 2.17
An/(Ab+An)	60.14 ± 0.81	57.98 ± 0.65

Plagioclase cations calculated on an 8-oxygen basis.

Table 2.4. Average compositions from matrix plagioclase

Average compositions of Spinels		Average Composition of Plagioclase inclusion in Spinel	
TiO_2	0.01 ± 0.01		
Al_2O_3	58.55 ± 0.29	SiO_2	57.63 ± 0.50
FeO	16.41 ± 1.95	Al_2O_3	26.79 ± 0.34
Fe_2O_3	1.87 ± 0.41	FeO	0.68 ± 0.08
MnO	0.06 ± 0.02	CaO	8.89 ± 0.13
MgO	3.04 ± 0.47	Na_2O	6.8 ± 0.21
ZnO	22.91 ± 2.70	K_2O	0.13 ± 0.02
Total	102.86	Total	100.93
Ti	0.002 ± 0.003		
Al	15.68 ± 0.08	Si	2.57 ± 0.01
Fe^{3+}	0.32 ± 0.07	Al	1.41 ± 0.02
Fe^{2+}	3.12 ± 0.37	Fe^{2+}	0.03 ± 0.003
Mn	0.01 ± 0.004	Ca	0.42 ± 0.01
Mg	1.03 ± 0.16	Na	0.59 ± 0.02
Zn	3.84 ± 0.46	K	0.01 ± 0.001
Gah	48.02 ± 5.79	Or	0.73 ± 0.11
Spn	12.88 ± 1.96	Ab	57.61 ± 0.75
Mag	2 ± 0.45	An	41.66 ± 0.76
Her	36.95 ± 4.33	An/(Ab+An)	41.96 ± 0.76

Spinel cations calculated on a 32-oxygen basis, plagioclase cations calculated on an 8-oxygen basis.

Table 2.5. Average compositions of spinel and plagioclase inclusions therein (see Fig 2.7.)

Method	Regional Metamorphism		Contact Metamorphism	
	P (GPa)	*T* (°C)	*P* (GPa)	*T* (°C)
Waldron, 1986	0.49 - 0.57	530 - 550	0.7 - 0.8	>700
Whitney et al., 1996	0.3 – 0.53	485 - 515		
Henry, 1997	0.4 - 0.57	680 - 760	0.38 - 0.6	575 - 700
Chen, 2009	0.59 ± 0.11 (1σ)	557 ± 12 (1σ)		
This study, Exchange and Net-Transfer Equilibria	0.51 ± 0.1	617 ± 50	0.93 ± 0.1	785 ± 50
This study, Average*PT* method in THERMOCALC	0.50 ± 0.12	642 ± 76	0.85 ± 0.13	798 ± 87

Table 2.6. *P–T* estimates from studies in and around the Manhattan Prong.

Chapter 3

Thermodynamic Modeling of Crustal Melting Using Xenolith Analogs from the Cortlandt Complex, New York, USA

K.M. Dorfler, M.J. Caddick, R.J. Tracy

Department of Geosciences, Virginia Polytechnic Institute and State University, Blacksburg, VA 24061, USA

This article will be submitted to *Journal of Petrology* for publication

Abstract: Emplacement of gabbroic magmas of the Cortlandt Complex, New York induced rapid (less than 5 years) heating of pelitic schist protoliths (T up to 1200 ˚C, P ~ 0.9 GPa). Xenoliths entrained within the mafic melt experienced significant melting and melt-segregation processes, now represented as a series of complex fabrics and structures comprising Si-rich veins and Al-rich, Si-poor residuum (a typical assemblage is spinel–magnetite–ilmeno-hematite–sillimanite±sapphirine±corundum). Subtle microscopic textures in the residuum include corundum–magnetite symplectites, which are interpreted to be a result of oxidative breakdown of the hercynite component in spinel during cooling. Aluminous orthopyroxene selvages in veins typically have grown along the contact between the residuum and quartzofeldspathic melt. Hybrid monzonorite and monzodiorite crop out near the xenoliths and are interpreted to represent assimilation by the mafic magma of the partial melt produced from the pelitic xenolith. Equilibrium-melting and batch-melting models track the evolution of the pelitic schist, its partial melt upon heating, and the residuum from melting and melt extraction. We introduce a 'filter-pressing' cooling calculation to simulate the crystallization of the quartzofeldspathic veins. Modeling results yield: (1) an initial partial melt that, when mixed with the estimated composition of the mafic melt, produces a hybrid igneous rock consistent with the monzonorite found near the xenolith, (2) a high-T melt that upon 'filter-pressing' crystallization produces a mineral assemblage which texturally and compositionally corresponds to the quartzofeldspathic veinlets retained in the samples within xenolith interiors, and (3) a residual material that, when oxidized, resembles the assemblages in the residuum. Modeling of crystallization of the high-T melt predicts early orthopyroxene formation, with Al content of orthopyroxene consistent with that of analyzed selvage pyroxene. We propose that this pyroxene reflects a primary melt crystallization phase rather than reaction-rim margins of the veins against residual matrix.

3.1 Introduction

Detailed studies of country rock–magma interactions are vital to developing our understanding of processes such as crustal contamination of mantle-derived mafic magmas, partial melting in the crust, and melt loss during high-grade metamorphism. Specifically, understanding interactions between felsic crustal xenoliths and mafic magma in plutons can yield valuable insight into: (i) larger-scale processes in mid to deep-crustal settings by shedding light on material and heat transfer; (ii) the production of granitoid melts through partial melting of aluminous protoliths; and (iii) the generation of dense silica deficient residuum that may be an important constituent of the lower crust (Johnson *et al.*, 2010, Markl, 2005, Preston *et al.*, 1999).

Laboratory-produced samples and experimental studies (e.g. Ackermand *et al.*, 1975, Hensen & Green, 1970, Hensen & Green, 1971, Hensen & Green, 1972, Hensen & Green, 1973, Newton, 1972, Patino Douce & Beard, 1995) are extremely useful in understanding how UHT products (melts and residuum) form, as both the reactants and products are carefully controlled and the processes are closely monitored. However, experimental studies cannot fully simulate the

evolution of natural rocks due in part to obvious scaling, time, and mass constraints, as well as to the fact that natural materials may represent complex interplay between coeval heating, melt addition or loss, fractionation processes, wall-rock interaction, and deformation (e.g. Preston *et al.*, 1999). To some extent this information is recoverable through careful spatial characterization of mineral composition and textures of natural igneous and metamorphic samples. On the other hand, in most cases one or more of the protoliths or products of melting and crystallization in natural environments is absent or has been subsequently modified in the field. Although natural samples may not have been produced in an easily interpreted environment, if the products and reactants of UHT processes such as partial melting of crustal xenoliths are available and the melt preserved, careful thermodynamic and mass balance modeling experiments can replicate the processes and products, allowing for quantitative insight into how residual xenolithic material and partial melt evolved, and how they possibly modified the primary enclosing magma (e.g. magma mixing/contamination).

Several recent studies have focused on interactions between felsic xenoliths and mafic magma and resulting implications for crustal contamination and the overall production of granitic melts, including localities such as the Moine Supergroup (Preston *et al.*, 1999), French Massif Central (Maury & Bizouard, 1974), Bushveld Complex (Johnson *et al.*, 2010, Johnson *et al.*, 2011) and Skaergaard intrusion (Markl, 2005). In addition to these, another occurrence that shows country rock–magma interactions is the Cortlandt Complex in southeastern New York, a small (~ 60 km^2) Ordovician mafic complex which contains many aluminum-rich xenoliths that experienced extensive chemical interaction with initially Mg-rich and presumably mantle-derived basaltic melts during the emplacement of the mafic pluton.

This study focuses on a single xenolith (roughly 30 m across), which is representative of others in a xenolith swarm at Salt Hill in the southeastern quadrant of the Complex, 6 km southeast of Peekskill, New York. A clear physical contact between the xenolith and the host cannot be identified due to quarrying and extensive vegetation as well as the possibility that the contact itself may be a bit diffuse or transitional. Mineral assemblages and textures from samples collected in a single traverse across the xenolith and into the surrounding igneous rocks indicate extensive melting that produced a silicic melt which was then extracted and mixed with the mafic magma, locally forming a hybrid monzonorite marginal zone and leaving behind an aluminum-, iron- and titanium-enriched, silica- and alkali-depleted residuum within the xenolith.

The immobile residuum consists of a mineral assemblage of spinel–magnetite–ilmeno-hematite–sillimanite±sapphirine±corundum, colloquially known as 'emery', that can vary in mineral proportion and is transected by a network of veins and veinlets of fine-grained quartzofeldspathic material, interpreted to be remnants of some stage of partial melt produced within the xenolith. Production of granitoid melt upon heating of an Al-rich sediment is well documented and often linked with magma contamination (Diaz-Alvarado *et al.*, 2011, Johnson *et al.*, 2010, Markl, 2005, Preston *et al.*, 1999, Theriault *et al.*, 1997). However, clear field evidence of a granitic melt, a contaminated or hybridized magma and an unmodified parental magma from a single occurrence has yet to be documented as far as we know. This study on the Salt Hill xenolith and surrounding igneous rocks yields petrologic evidence of the pre-intrusion protolith of the xenolith, estimated parental host magma, aluminous xenolith residuum, felsic melt produced during heating, and a hybrid igneous rock formed through mixing of the locally derived partial melt with the apparently primitive, mantle-derived gabbroic magma.

The strategy for this study was to use careful textural and mineralogical observations and chemical compositions (chemical petrography) of samples from the Cortlandt Complex to constrain and test quantitative models for isobaric melting of the Salt Hill metapelitic xenolith during magmatic heating, with the ultimate goal of understanding the mechanisms involved in production of a siliceous melt and aluminum-rich residuum during contact heating. These fractionated products can ultimately be linked to crustal melting and fractionation at mid- to deep-crustal levels. Equilibrium-melting and batch-melting models (at varying melt-removal intervals) were tested to simulate the range of possible melting processes and allow discrimination between them based on observed petrologic relationships. Modeling results produced: (1) an initial partial melt that, when mixed with the estimated composition of the mafic melt, produces a hybrid igneous rock congruous with the monzonorite found near the xenolith, (2) a high-T melt that, upon crystallization, produces a mineral assemblage that texturally and compositionally corresponds to the quartzofeldspathic veinlets retained in the samples within xenolith interiors, and (3) a residual material that, when oxidized, resembles the assemblages in the residuum.

3.2 Petrology of the Cortlandt Complex, Salt Hill xenoliths, and hybrid igneous rock

3.2.1 Cortlandt Complex and Manhattan Schist

The Cortlandt Complex is a ~ 60 km^2 composite intrusion of six mafic to ultramafic plutons near Peekskill, New York, about 40 km north of New York City (**Fig. 3.1**). The six plutons are numbered in order of emplacement as distinguished by crosscutting relations, internal structure, post-emplacement deformation, mineralogy and chemistry (Ratcliffe *et al.*, 1982). The complex formed *c.* 446 Ma (Ratcliffe *et al.*, 2012), postdating regional metamorphism and deformation during the Taconic Orogeny by *c.* 20–30 Ma. Its contacts cross-cut steeply dipping Taconic Barrovian regional metamorphic isograds that range from biotite and garnet on the lower-grade western end near the Hudson River to sillimanite-staurolite-muscovite at the eastern end. Given the relatively short west-to-east dimension of the complex (<8 km), this likely represents a compressed metamorphic gradient that is thought to be unrelated to the subsequent emplacement of mafic melts.

The relatively short time interval between peak regional metamorphism and pluton emplacement suggests that the regional country rocks at the eastern end of the Complex were still at elevated temperatures (~ 480–550 ˚C) at the time of emplacement, (assuming average cooling rate of 3–5 ˚C Ma-1 from a peak-T of ca. 630 ˚C over 25-30 Ma, Dorfler *et al.*, 2014). Thermobarometric characterization of a nearby contact aureole around a contemporaneous small pluton to the north-northeast of the Cortlandt Complex indicates that the pressure at the current level of erosion was ~ 0.9 GPa at the time of pluton emplacement (Dorfler *et al.*, 2014). In an unpublished thesis, Waldron (1986) estimated peak conditions for regional metamorphism on the eastern side of the Cortlandt Complex outside of the contact aureole (sillimanite + muscovite grade) to be 615–645˚C and 0.64–0.72 GPa, using thermobarometers available at the time.

The youngest pluton of the series (pluton VI) is host to many metapelite or marble xenoliths and contains the Salt Hill xenolith swarm that contains numerous screens and curtains of aluminous xenoliths located in the southeasternmost end of the pluton. Unequivocal parental magma for the pluton has not been identified anywhere in the Complex due to intense fractional crystallization, geochemical interactions and contamination/assimilation (Bender *et al.*, 1984). However, Tracy (2009) conducted a series of experimental fractional crystallization model calculations at 0.8 GPa using MELTS (Asimow & Ghiorso, 1998, Ghiorso & Sack, 1995) with several potential parental mafic magma compositions. Using a Karoo picritic dolerite (a mildly

alkalic Mg-rich basalt) as a parental magma (McBirney, 2007), he was able to produce a close match to the compositions and proportions of minerals in the cumulate olivine-pyroxenite layers of Pluton VI, implying that the primary melt was likely to have been similar in composition to McBirney's Karoo dolerite.

There is no evidence of any distinctive systematic mineral assemblage variation from the core to the rim of the xenolith that would indicate any temperature gradient, so it is assumed that the xenolith and surrounding igneous rocks achieved thermal equilibrium. Thermometry using THERMOCALC (Powell & Holland, 1988, Powell & Holland, 1994, Powell & Holland, 2008, Powell *et al.*, 1998) of equilibria involving spinel, orthopyroxene, garnet, sillimanite and quartz in the xenolith implies that the secondary silicates equilibrated at temperatures ~ 1100 ˚C during cooling, indicating the peak temperature of the residuum in thermal equilibrium with the magma must have been greater than 1100 ˚C. The composition of evolved fractionate from the original parental magma composition used in the MELTS simulation at 1200 ˚C (effectively a mildly alkalic gabbro composition) is thus used as an analog for the external magma surrounding the xenolith at the time of its contact heating and resulting dehydration reactions, including melting.

The country rocks of the Manhattan Prong that surround the intrusive complex include regionally metamorphosed and complexly folded Neoproterozoic to Ordovician gneisses, schists, marbles, and amphibolites. Both the Inwood Marble and Manhattan Schist immediately surround the complex, the latter abutting the southeastern border of the complex closest to Salt Hill. The Manhattan Schist as a map unit contains diverse lithologies including pelitic schists of varying composition, amphibolites and calc-silicates. It is likely that the protoliths for the Salt Hill xenolith swarm were similar to the Manhattan Schist units just outside the contact aureole near Salt Hill. These metapelites are quartz-rich plagioclase-sillimanite-muscovite-biotite-garnet schists with variable amounts of Fe-Ti oxides and occasional staurolite. Determining an *exact* protolith composition for the xenolith under study is not feasible considering the variable bulk composition of local schist lithologies and the extensive metasomatic effects that altered the bulk chemistry of the xenolith during melting and melt extraction. Rogers (1911) obtained and reported several wet chemical analyses of Manhattan Schist and found that the four individual schist analyses he obtained (analyses 24–27, see **Table 3.1**) varied from 40.16–62.98 wt% SiO_2, 16.88–29.5 wt% Al_2O_3 and 2.48–19.66 wt% Fe_2O_3.

Additional information on the petrology and structure of the Cortlandt Complex and the surrounding rocks, including the various xenoliths, can be found in Friedman (1956), Barker (1964), Caporuscio and Morse (1978), Domenick and Basu (1982), Ratcliffe et al. (1982), Waldron (1986), and Johnson & Tracy (1998). Parenthetically, the earliest known published work on the Cortlandt Complex was that of J.D. Dana (1881).

3.2.2. Salt Hill Xenoliths and Monzonorite

General petrogenetic relationships within the Cortlandt xenoliths, specifically from Salt Hill, have previously been investigated in field and laboratory studies, with emphasis on the petrogenesis of emery, a corundum-bearing abrasive material (Barker, 1964, Bender *et al.*, 1984, Caporuscio & Morse, 1978, Friedman, 1956). Tracy and McLellan (1985) was the first study to provide detailed petrographic interpretation of the Salt Hill samples using textural and mineral compositional data to determine the kinetic controls on the metamorphic processes, especially reaction kinetics and occurrence of localized equilibrium. They concluded that heating of the xenolith likely produced a significant amount of silica-rich peraluminous melt that eventually escaped and mixed with the surrounding mafic magma to form a hybrid igneous rock zone surrounding the original schist xenolith. Crosscutting quartzofeldspathic veins and veinlets (from millimeters to tens of millimeters in thickness) are present within the xenolith samples, and were interpreted by Tracy & McLellan (1985) to represent a remnant fraction of the highly siliceous, locally derived melt. In this paper we test this premise thermodynamically, showing that although the earlier study captured the gross behavior of Salt Hill heating and resulting reactions, a more complex and subtle suite of processes is required to explain all of the preserved lithologies and textures.

The Salt Hill xenolith samples examined in this study consist of two chemically and physically segregated materials: an alumina-rich, silica-deficient residuum and SiO_2-rich quartzofeldspathic veinlets (**Fig. 3.2**). The residuum consists of varying mineral assemblages including aluminous spinel (20–50 vol%), complexly exsolved ilmeno-hematite (10–20 vol%), magnetite (5–20 vol%), sillimanite (10–50 vol%), corundum (0–5 vol%), sapphirine (0–40 vol%), garnet (0–5 vol%), and anorthite (0–1 vol%). In general, the residuum can be either sapphirine-bearing with Mg-rich spinel or sapphirine-absent in which case modal spinel is generally higher and the spinel has noticeably lower Mg/(Mg+Fe) (**Fig. 3.3**). Corundum is sparse

and sporadic, can occur in either the sapphirine-bearing or sapphirine-absent residuum, and is present as either larger prismatic crystals surrounded by magnetite, spinel, or ilmeno-hematite solid solution, or as much finer-grained corundum-magnetite symplectites along edges of spinel, apparently formed by oxidative breakdown of the hercynite component in spinel.

The crn–mt symplectites occur only in spinel crystals in spl–ilm-hem–mt rich aggregates in the residuum and are in direct contact with only spl, ilm-hem, or mt (**Fig. 3.4**). However, not all spinel crystals host the symplectite and only the spinels that are in direct contact with either ilm-hem or mt contain the texture. Corundum, sapphirine, orthopyroxene and sillimanite can occur nearby (~ 50–100 microns away from the texture) but never adjacent to the symplectite. There is no biotite or white mica present near the symplectites and virtually none in thin section. The symplectites are very fine-grained and can only be identified with EDS chemical overlay maps. The texture makes somewhat of a pathway through some spinel crystals, however there are no distinctive cracks or fractures along with the symplectites that would indicate a fluid-assisted pathway through the spinel, and in many cases the symplectite is present along the edge of a spinel and terminates half-way through the crystal.

Chemical traverses across spinel grains show a distinctive increase in Mg content from Mg/(Mg+Fe) ~ 0.51 in the interior of the spinel to ~ 0.67 to the boundary of the symplectite and decrease in Fe content from Fe/(Fe+Mg) ~ 0.49 to ~ 0.33 at the boundary with the symplectite (**Fig. 3.4**). Essentially, the spinel crystal is becoming less hercynitic (poorer in $FeAl_2O_4$) and more spinel-rich (higher in $MgAl_2O_4$) toward the symplectite. The breakdown reaction of hercynitic spinel:

$$3FeAl_2O_4\ (her) + O_2 = Al_2O_3\ (cor) + Fe_3O_4\ (mt) \qquad (3.1)$$

is a simple oxidation reaction that is typically found in high-*T* granulite-facies metapelites that experienced some degree of fluid-assisted retrogression, resulting in chloritization or sulfidation of the symplectites (Karlsson, 1986; Schneiderman and Tracy, 1991; Waters, 1991; Knudsen, 1996; Dasgupta et al., 1997; Buick, et al; 1998, Tsujimori and Ishiwatari, 2002). The aluminous spinel in the Salt Hill residuum samples clearly exhibits an oxidation reaction to form cor-mt symplectites, however there is no direct evidence for the presence of fluids (or fluid interactions) due to the absence of hydrous phases. We interpret the crn-mt association as evidence of a

simple down-temperature breakdown reaction of hercynite at fO_2 well above FMQ, as suggested by Caporuscio and Morse (1978).

The quartz-grain-supported veinlets contain > 90 wt% SiO_2 (based on modal analysis from image processing and average phase compositions) and consist of roughly 80 modal percent of 1–2 mm diameter rounded quartz crystals with optically continuous microperthitic ternary feldspar infilling the triangular interstices between the quartz crystals (average integrated feldspar composition of $Or_{34}Ab_{51}An_{15}$) with minor prismatic sillimanite blades and hercynite-rich spinel (**Fig. 3.3 and 3.5**). Sapphirine, garnet and orthopyroxene reaction rims surround spinel or Fe-Ti oxides where there is extensive physical (and chemical) interaction between the veinlets and adjacent residuum. More magnesian centimeter- to meter-scale lithologic units within the xenolith contain sapphirine and orthopyroxene and less garnet, whereas the less magnesian units (as indicated by residuum spinel compositions) contain more secondary garnet and no sapphirine or orthopyroxene (Tracy & McLellan, 1985). Overall, orthopyroxene is the most widely occurring secondary silicate (Johnson & Tracy, 1998).

These observations most likely reflect a variation in original bulk composition of the schist protolith, which clearly plays an important role in controlling the residuum assemblage and the formation sequence of secondary silicate phases. Uniformly thick orthopyroxene selvages lie along the veinlet-residuum boundary in zones where there isn't as much physical interaction between veinlet and residuum (**Fig. 3.5**). The orthopyroxene composition is constant parallel to the vein-residuum boundary, with Fe/Fe+Mg = 0.37. However, a strong compositional change in Al content of orthopyroxene occurs normal to the boundary, with a higher average Al concentration (in cations per 6 oxygen formula basis) of 0.46 pfu on the residuum side of the selvage and a lower Al concentration of about 0.22 pfu adjacent to the vein (**Fig. 3.6**). We initially interpreted the selvage as a reaction-rim product that formed during silication of the spinel in the residuum by the reaction spl + melt = opx + sil. However, orthopyroxene is present regardless of the substrate phase in the residuum (spl, ilm-hem, mt or even crn), which indicates that it more likely is a primary product of crystallization from a melt, rather than a reaction product, and that it nucleated from melt along the irregular interface, regardless of substrate mineral.

A hybrid monzonorite near the margin of the xenolith swarm in pluton VI contains intermediate plagioclase, mesoperthitic alkali feldspar, ortho- and clinopyroxenes and texturally

late hornblende and biotite (this latter mineral typically in sprays radiating from Fe-Ti oxide grains). The presence of this "mixed" rock that typically represents contamination indicates that chemical and physical mixing of xenolith-derived partial melt and surrounding mafic magma occurred during xenolith heating and melting following xenolith incorporation in the magma. In thin section, replacement of pyroxene along grain margins by amphibole is common, as is the above-noted growth of radiating sprays of biotite on oxide grains. Additionally, the samples contain excessive modal amounts of apatite and plagioclase crystals are bent into horseshoe-like shapes, which likely indicate severe deformation of the crystals.

One of the goals of this paper is to determine if the monzonorite could have been formed via mixing of a felsic melt produced during heating of the xenolith (at temperatures well above its solidus) with an estimated fractionated composition of the external magma. Mixing felsic and mafic magmas depends on the compatibilities of their physical properties (viscosity) after thermal equilibrium and homogenization can only occur if the two melts behave similarly at the same temperature (Sparks & Marshall, 1986). We aim, therefore, to understand the formation of the hybrid igneous rock, the residuum, the quartzofeldspathic veinlets, and their orthopyroxene selvages by constructing thermodynamic heating, crystallization and oxidation models, and by examining the viscosity contrasts of each of the melt phases to identify whether hybridization is feasible.

3.3 Thermodynamic Modeling Methods

To understand progressive reaction and melting processes during heating of the xenolith to well over 1100 ˚C, we isobarically forward-modeled the heating of a Manhattan Schist protolith bulk composition at 0.9GPa in the system TiO_2-Na_2O-CaO-FeO-Fe_2O_3-K_2O-MgO-Al_2O_3-SiO_2-H_2O. Calculations utilized the ds5.5 update to the Holland & Powell (1998) thermodynamic dataset, further modified for sapphirine end-members following Kelsey *et al*. (2004). Complex phases were modeled with activity-composition models for melt (White *et al.*, 2001, White *et al.*, 2007), feldspar (Holland & Powell, 2003), sapphirine (Taylor-Jones & Powell, 2010), white mica (Coggon & Holland, 2002), ilmeno–hematite (White *et al.*, 2000), spinel–magnetite (White *et al.*, 2002), garnet (White *et al.*, 2005), orthopyroxene, biotite (both Powell & Holland, 1999), and staurolite (Holland & Powell, 1998). All calculations used Perple_X 6.6.8 (Connolly, 2005), with modifications made as described below.

Having a well-constrained protolith bulk-rock composition is crucial for a forward-modeling study. Previous xenolith-magma studies (i.e., Markl, 2005) inferred protolith composition from its altered product, but here there are numerous reported bulk chemical analyses of the regionally metamorphosed Manhattan Schist that are available. For example, Tracy & McLellan (1985) suggested that there were at least two protolith Manhattan Schist lithologies in one xenolith, based on bimodal behavior of the Fe/(Fe+Mg) of matrix spinels in residuum and the presence or absence of sapphirine and cordierite in residuum. For the calculations shown here, we chose to use one average Manhattan Schist composition based on a composite of five separate schist analyses reported by (Rogers, 1911). Because the specific lithologies that produced either type of residuum (sapphirine-bearing and sapphirine-absent) are not known and cannot be reconstructed with any confidence due to extensive melting, using an average composition is the most justifiable approach. We acknowledge that use of this 'average Manhattan Schist' composition introduces some uncertainty, but will demonstrate below that all modeling results using this estimated protolith composition are consistent with melt and reaction products observed.

The Manhattan Schist xenolith, which we estimate to have cooled from ~ 625 ˚C to ~ 500 ˚C in the interval between the Taconic-age sillimanite-grade regional metamorphic peak at roughly 465 Ma to contact heating upon incorporation into magma at roughly 446 Ma, must have been rapidly heated to magmatic temperatures (up to an estimated 1200 ˚C) once it was fully immersed in that mafic melt. 1-D heat conduction modeling, assuming a 30m diameter spherical xenolith and an infinite reservoir of magma at a temperature of 1200 ˚C (i.e. assuming that the heating of the xenolith did not significantly cool the melt), predicts that the core of the xenolith would reach 1150 ˚C in approximately 3 years (**Fig. 3.7**). The outermost 85% (by volume, assuming a spherical xenolith) would have reached 900 ˚C less than one year after initial immersion in the mafic melt, therefore making it possible that the rate of melt production overstepped the rate of melt removal from the xenolith. It is also likely that prograde metamorphic dehydration reactions at lower temperatures that did not involve melting were significantly overstepped until melt was present to increase intergranular diffusion rates. Therefore, we propose that an equilibrium melting model, without removal of melt from the system, best represents processes during the initial heating of the Manhattan Schist. We note,

however, that low temperature equilibria may not accurately reflect the earliest stages of xenolith formation.

At temperatures much higher than that of the solidus, silica-rich melt loss from the xenolith proceeded, yielding a silica-deficient residuum. This requires a different modeling strategy in which the calculated bulk composition is progressively altered upon melt loss. Both the solid phase and melt products of this calculation must be shown to evolve to form the observed mineralogy and measured phase compositions of the aluminum-rich residuum and silica-rich veinlets. **Figure 3.8** is a flowchart that shows the sequential calculations that we undertook to model formation of the various analyzed products, starting with this initial heating to 900 ˚C. Each of these steps required different approaches and assumptions and is described in detail in the following sections.

3.4 Results

3.4.1 Initial Heating and Melt Generation

In an equilibrium thermodynamic model for heating the average Manhattan Schist at 0.9 GPa, melt is first produced at 695 ˚C from the complex melting reactions involving quartz, muscovite, biotite, and plagioclase (**Fig. 3.9A**). As temperature continues to increase, muscovite is the first phase to completely disappear (by 757 ˚C), at which point there is a significant decrease in quartz and biotite contents in the residual solids, followed by kyanite transformation to sillimanite at 762 ˚C. Total feldspar content increases significantly up to 757 ˚C due to the complete breakdown of muscovite and continued breakdown of quartz, with the K_2O content of that feldspar increasing accordingly to ~ 10 wt % at 760 ˚C, corresponding to a composition of ~ $Or_{57}Ab_{40}An_2$. Modal garnet content doubles from 760 to 815 ˚C (7–14 volume % respectively), by which point biotite has completely melted. Quartz and plagioclase continue to dissolve into ambient melt above 815 ˚C, until quartz is finally lost at 912 ˚C. Upon continued temperature increase, plagioclase is the only phase that continues to be depleted rapidly, before its disappearance at 970 ˚C. At this point the calculated residuum consists of garnet, sillimanite, and ilmenite. Once temperature reaches 1007 ˚C, sapphirine begins to form at the expense of sillimanite and garnet, which are lost at 1034 ˚C and 1059 ˚C, respectively. Sapphirine peaks in abundance at 1059 ˚C (6.7 vol%) but then breaks down upon further heating, completely disappearing at 1187 ˚C and leaving only ilmenite in the residuum.

This simple model predicts that quartz and feldspar should be absent from the high-*T* residuum assemblage (matching observations), but the calculated mineral assemblages above 1100 ˚C are significantly different from those observed in the xenolith samples (the only stable phases are sapphirine and ilmenite) and at no point does the model calculate the observed assemblage spl+mt+ilm-hem+sill±spr±cor±an. Although the modeled melt composition produced at 1200 ˚C in **Fig. 3.9A** is silica rich (~ 60 wt%), its modeled crystallization does not reproduce the observed mineralogy of the quartzofeldspathic veinlets. In fact no single melt composition from this model is appropriate to form the mineralogy of the quartzofeldspathic veins when its crystallization is modeled, and we do not believe that modeled melts illustrated in **Fig. 3.9A** were retained within the xenolith as veinlets. Accordingly, we examined a possible outcome if this melt left its xenolith parent. We mixed the melt derived at 900 ˚C through equilibrium melting of the metapelite (where 60 vol% of the xenolith is melted – **Fig. 3.9A**, **Table 3.2**, column 1), with the fractionate of parental mafic melt at 1200 ˚C **Table 3.2**, column 2). The ratio of 'felsic' melt, i.e. melt produced by heating the pelitic schist to 900˚C, and 'mafic' melt was adjusted to minimize the difference between the composition of the resultant hybrid and an averaged analyzed composition of two monzonorite samples found surrounding the xenolith in the field (**Table 3.2**, column 3). A best fit of approximately 60 % mafic melt mixed with 40 % felsic melt yielded a hybrid melt that best matches the composition of the Cortlandt monzonorite in terms of all ten oxides considered, albeit with lower MgO content (presumably reflecting a small difference between estimated and actual mafic melt compositions). We thus propose that the monzonorite formed via mixing of an initial partial pelitic melt at ~ 900 ˚C with the host mafic magma, and explore the feasibility of this in terms of melt viscosities below.

3.4.2 Continued Melting from 900 ˚C and Veinlet Formation

The second stage of our model simulates continued heating of the xenolith, beginning with the same bulk composition used in the initial calculation (**Fig. 3.9A**). Once melt begins to escape its host (i.e. a xenolith), it is likely to continue to do so (Marschall *et al.*, 2013) either continuously or cyclically depending on the applied differential stress and rate of melt pressure buildup (Brown, 2001), so we modified our strategy to calculate phase equilibria in 50 ˚C intervals, removing any stable melt in each step, to simulate a small-step batch melting process. Smaller temperature increments yielded similar results, as discussed below. **Figure 3.9B** shows

the result at each stage by plotting the residuum and melt at each temperature interval, with the 'bulk composition' recast after any step in which melt was produced and extracted. At 900 ˚C, the phase proportions are exactly the same as they were in the previous model (qtz+sill+grt+ilm+plg co-existing with ~ 60 % melt that is extracted before the next calculation step). Removal of this hydrous melt leaves a completely dry residuum that is unable to melt further until dry melting reactions begin above 1100 ˚C, so there is little change in the calculated proportions of the phases between 950 and 1100 ˚C. At 1150 ˚C, however, the system reaches the solidus for its new (depleted) composition and begins to produce a silica-rich melt, leaving behind an even further SiO_2-depleted residuum (spr+grt+ilm).

The calculated melt at 1150 ˚C is silica- and alumina-rich (66 wt% SiO_2, 19 wt% Al_2O_3). Assuming that this melt may have formed the veinlets shown in **Figures 3.3C and 3.5**, we calculated its crystallization products upon cooling using the same thermodynamic data as in the heating calculations (**Fig. 3.10**). This new calculation begins with a bulk composition fixed as the silica-rich melt composition produced at 1150 ˚C (**Fig. 3.9B**), but permits modification of the bulk composition by accounting for loss of partial melt during cooling. Phase equilibria were calculated in 1˚C increments, permitting 25 % of the calculated melt fraction at each step to be removed. This essentially simulates a filter-pressing type of crystallization. We acknowledge that a more sophisticated approach would involve calculation of the melt fraction and viscosity at each temperature before calculating the amount of melt that should be extracted (which should also be cooling-rate dependent), but the simple strategy of removing 25 % of the melt present in each 1˚C increment over the narrow crystallization interval is considered to be a reasonable simplification. A minor modification of Perple_X was required to permit this partial fractionation calculation, and the modified binary is available for download from http://www.metamorphism.geos.vt.edu/Resources.html.

Crystallization of felsic melt illustrated in **Fig. 3.10** begins with 100% melt at 1150 ˚C and ends with melt completely crystallized to qtz+sill+fsp+opx by 1114 ˚C, thus agreeing well with the observed phase assemblage in the veinlets. The very small crystallization temperature interval reflects the anhydrous nature of the melt. Quartz is the first solid phase to form in this model at 1148 ˚C and is followed by sillimanite, ternary feldspar ($Or_{50}Ab_{45}An_4$) and an aluminous orthopyroxene at 1133, 1132, and 1130 ˚C, respectively. The orthopyroxene begins crystallizing with an Al content of ~ 0.34 (per 6 oxygens) and falls to ~ 0.26 by 900 ˚C. The

Fe/(Fe+Mg) ratio in the orthopyroxene is initially 0.48 at 1130 ˚C, increases to 0.60 at 1115 ˚C, and remains constant during further cooling. The final calculated rock is composed of 83 vol% quartz, 12 vol% ternary feldspar, 4 vol% sillimanite and 1 vol% orthopyroxene, with an overall bulk composition containing 92 wt% SiO_2. The modeled assemblage, phase proportions and change in composition of the orthopyroxene as it continues to crystallize are almost identical to our observations of the quartzofeldspathic veinlets and orthopyroxene selvages in the natural samples (e.g. **Figures 3.3, 3.5 and 3.6**). Furthermore, textural observations such as large rounded quartz crystals suspended in interstitial ternary feldspar, which imply that the quartz was first to crystallize from the melt, are consistent with the crystallization sequence modeled here.

3.4.3 Evolution of the Residuum

At 1150 ˚C, the batch-melting model produces a silica-rich melt that crystallizes to a quartzofeldspathic rock consistent with observations of the natural veinlets, but the calculated residuum assemblage (spr+grt+ilm) does not mineralogically resemble the natural residuum. Based on coexistence of ilmeno-hematite (which, based on a bulk composition of the grains in terms of pure $FeTiO_3$ and Fe_2O_3, has a 70:30 ratio of hematite to ilmenite), as shown to the left of **Fig. 3.6A** and in **Fig. B2**) with almost pure magnetite in the natural samples, we estimate that the xenolith experienced increasingly oxidizing conditions almost to the hematite-magnetite buffer at some point during residuum formation/evolution. We thus explored post-melting oxidation and cooling of the residuum that was calculated in the batch-melting model at 1150 ˚C (**Fig. 3.9B**) with a T–X_{O2} diagram (**Fig. 3.11**) in which the horizontal axis represents increasing ferric/ferrous ratio: the initial ratio suggested for the residuum from the calculations for **Fig. 3.9B** is on the left, and Fe_2O_3/FeO increases progressively to the right. As noted above, the natural residuum assemblage is variable but is predominantly composed of spl+mt+ilm-hem+sil±spr±crn with < 2 vol% each of garnet and almost pure anorthite. Simply increasing the ferric/ferrous iron ratio at 1150 ˚C predicts the formation of a residuum assemblage (spl+ilm+spr+sil+an+crn) with phase proportions moderately close to the range observed in the natural sample (**Fig. 3.11**). Furthermore, oxidizing the residuum to a Fe_2O_3/FeO of 0.35–0.58 and cooling to temperatures between 960–1000 ˚C produces the assemblage spl+ilm+spr+sil±crn±grt±an with phase proportions that match well with the observed range in the natural samples (see area identified in **Fig. 3.11**).

3.5 Discussion

3.5.1 Alternative Heating Models

The steps outlined above describe our preferred model for the heating and formation of the Salt Hill xenoliths, predicting the composition and phase proportions consistent with the monzonorite, quartzofeldspathic veinlets, and residuum from the Salt Hill samples. To test alternative possible methods of formation we compared the initial equilibrium-heating stage with results of 'ideal' batch-melting models in which 100 % of the melt generated at any step was removed before the next calculation step. These models utilized phase equilibria calculated in 1, 20, 30, 40 and 50 ˚C increments and used the same thermodynamic database, protolith composition, total pressure, and heating interval as in **Fig. 3.9A** (see **Fig. B1**).

The 1 ˚C increment batch-melting model produced a residuum (at $T > 1200$ ˚C) containing ~ 10.7 vol% quartz. The natural residuum is devoid of primary quartz; therefore this model was discarded. In contrast, the 20, 30, 40 and 50 ˚C increment batch-melting models predict that an unappreciable amount (< 1 vol%) of quartz is stable at temperatures above ~ 1140 ˚C (the 30 ˚C increment model predicts that ~ 8 vol% quartz is stable at 1200 ˚C, but diminishes to < 1 vol% at 1230 ˚C and 0 vol % at 1290 ˚C). In fact, all of these models predict that the mineral assemblage of the residuum will be composed of spr, ilm and spl (with minor amounts of grt, opx and qtz) at temperatures above 1140 ˚C (see **Fig. B1**). These results are similar to the calculated residuum assemblage at 1150 ˚C in our preferred model. However, when each calculated melt (at 1140, 1140, 1160 and 1150 ˚C from the 20, 30, 40, and 50 ˚C interval batch-melt models, respectively) were used in the "filter-pressing" crystallization model described above, the calculated crystallization products yielded inappropriate phase proportions (e.g. 56–69 vol% ternary feldspar) which do not match observations from the quartzofeldspathic veinlets in the Salt Hill samples. In addition, the xenolith-derived melt required to form the hybrid monzonorite by mixing is not produced in these alternate calculations, leading us to believe that retention of melt up to a melt fraction of ~ 60 % at ~ 900 ˚C, followed by progressive melt loss at higher temperature (and lower melt viscosity, see below) is more appropriate.

3.5.2 Monzonorite Formation

The calculation used to mix the 'felsic' melt produced at 900 ˚C in the initial heating model (**Fig. 3.9A**) and the 'mafic' melt derived by fractionation from the inferred parental picritic

dolerite yielded results that match the composition of the monzonorite samples found near Salt Hill. However, melt mixing is only physically possible if the viscosities of both melts are similar. The viscosities of the felsic and mafic melts were therefore calculated with a composition-dependent silicate melt viscosity calculator (available at http://www.eos.ubc.ca/~krussell/VISCOSITY/grdViscosity.html, Giordano *et al.*, 2008). This algorithm is calibrated to calculate viscosity over a wide range of compositions and temperatures at 1 bar pressure and we thus assume a minimal pressure effect on calculated viscosity. This assumption is clearly important, but should lead to less error for the relatively low dissolved-H_2O contents that we model here than it would for very H_2O-rich melts. At 900 ˚C the calculated viscosity of the felsic melt is $10^{4.2}$ Pa-s, decreasing to $10^{2.4}$ Pa-s as temperatures reach 1200 ˚C (**Fig. 3.12**). The calculated viscosity of the mafic melt at 900 ˚C is $10^{4.9}$ Pa-s, decreasing to $10^{1.5}$ Pa-s at 1200 ˚C. Although the viscosities of both felsic and mafic melt differ at 1200 ˚C, they converge at a calculated viscosity of $10^{3.6}$ Pa-s at 980 ˚C, implying that physical and chemical mixing of the felsic melt and mafic magma was likely not impeded by viscosity contrasts following extraction of the felsic melt from the xenolith at ~ 900 ˚C. This suggests that our interpretation of hybridization to form the monzonorite is feasible from a physical/mechanical point perspective. We note also that the viscosity of the high-*T* silica-rich melt generated at 1150 ˚C (**Fig. 3.9B**) is substantially higher than either of the other two calculated melt compositions, rendering the melt less mobile. This is consistent with the observation of retention of some proportion of this melt within the xenolith during crystallization to form veinlets.

The *exact* composition of the melts that mixed to produce the hybrid igneous rock and the temperature at which melt began to escape the xenolith cannot be definitively determined. However, our models quantitatively show that melt produced during initial rapid heating of the pelitic schist can compositionally and physically mix with the mafic melt to yield a hybrid igneous rock similar to the monzonorite upon its escape from the xenolith. Although the specific processes by which melt left the xenolith are unknown, melt transport and accumulation in partially molten rocks may be driven by hydraulic gradients caused by density differences or active deformation (Bons *et al.*, 2004). Therefore it is possible that the segregation of less-dense silica- and alkali-rich partial melt into veins or lenses contributed to the collapse and agglomeration of the iron- magnesium- titanium-rich residuum. Some samples of the residuum

contain triple-junction grain boundary textures of spinel and Fe-Ti oxides that are characteristic of annealing, which may have taken place during melt accumulation. Additionally, our modeling supports previous studies that report contamination of mafic magma by partial granitic melt derived from metapelites (Johnson *et al.*, 2010, Preston *et al.*, 1999).

3.5.3 Crystallization of Orthopyroxene Selvages

We initially interpreted the orthopyroxene selvage texture to be the product of silication of the residuum (principally spinel) by the quartzofeldspathic veins, much as initially proposed by Friedman (1954) in a paper on the spinel-silica reaction succession. However, there are two observations that conflict with that simple interpretation: (1) the selvages have a generally uniform thickness of about 30 microns along veinlet margins and adjacent to the residuum, irrespective of the substrate mineral in the residuum, whether spinel, corundum, ilmenohematite, magnetite or sillimanite; and (2) the composition of the orthopyroxene shows the same variation in Al content and Fe/Fe+Mg irrespective of the adjacent residuum and veinlet phases. Microprobe analytical traverses along the length of the selvage reveal little variation in Al content or Fe/Fe+Mg ratio (see **Fig. 3.6**) immediately adjacent to the residuum. Traverses that transect the selvage have the same Fe/Fe+Mg ratio across the orthopyroxene but decreasing Al content toward the veinlet. Based on these observations, a simple localized reaction-margin origin of the orthopyroxene is not credible, and instead it seems probable that the orthopyroxene was not a product of silication, but more likely crystallized from the veinlet-forming melt and nucleated uniformly at the irregular veinlet contact, on the surface of the residuum.

The 'filter-pressing' cooling model developed for this study, where 25% of the melt is removed at each 1 ˚C increment, best represents crystallization of the calculated silica-rich melt at 1150 ˚C. If the partial melt is segregated into veinlets and melt pockets (as observed in natural samples) by the agglomeration of the dense residuum, then phases crystallizing from the high-*T* melt would remain in the fractures as melt continued to be compressively "squeezed" or pumped. The filter-pressing crystallization model predicts that 1 vol% orthopyroxene forms from cooling the calculated melt produced at 1150 ˚C. Although orthopyroxene is the third and last phase to crystallize, it is predicted to crystallize only 18 ˚C after the initial crystallization of quartz, the first phase to crystallize at 1148 ˚C, and 3 ˚C after sillimanite, the second phase to crystallize at 1133 ˚C. This small temperature interval means that although the orthopyroxene was technically

the "last" phase to crystallize, sillimanite, ternary feldspar and orthopyroxene began to crystallize at about the same temperature after quartz. This cooling model was the only calculation that produced results consistent with the quartzofeldspathic veinlet texture and chemistry.

The modeled orthopyroxene initially crystallizes at 1130 ˚C with an Al content of about 0.34 cations pfu and upon cooling lessens to about 0.26 cations pfu by 900 ˚C. These values differ slightly from what we observe in the orthopyroxene selvages (which, on average, decrease from 0.46 on the residuum side of the selvage to about 0.22 adjacent to the vein, see **Fig. 3.6**), but the trend of decreasing aluminum content from the inferred first-crystalling orthopyroxene on the veinlet wall to the last orthopyroxene is consistent with our observations. The calculated Fe/(Fe+Mg) ratio of the orthopyroxene is initially 0.48 at 1130 ˚C and increases to 0.60 at 1115 ˚C and remains there for the duration of cooling. This differs from the Fe/(Fe+Mg) ratio in the samples, which remains a consistent 0.37 at any distance across the selvage. This discrepancy may be due to the differences in bulk chemistry of the protolith, or to the possibility that there was diffusional mobility of Fe and Mg within the selvage (in contrast to more limited Al mobility) and thus diffusional re-equilibration. Tracy & McLellan (1985) suggested that the Fe/(Fe+Mg) of the residuum spinel locally, and the occurrence of discrete secondary silicate assemblages, e.g., spl-grt-opx versus spl-spr-opx-crd that could be correlated with this variation in spinel chemistry, were a function of variations in original Fe/(Fe+Mg) of the Manhatttan Schist protolith within the xenolith. It is likely that the variation in Fe/(Fe+Mg) of the modeled orthopyroxene, which crystallized from the partial melt produced from heating the Manhattan Schist, may also be indirectly a function of the protolith composition.

3.5.4 Oxidation of the Residuum and Symplectite Formation

The calculated *T–X(FeO/Fe_2O_3)* diagram (**Fig. 3.11**) illustrates a potential residuum oxidation process in which oxygen content increases (indicated by the change in ferrous/ferric iron ratio) across a decreasing temperature space (cooling), from 1150–700 ˚C. In general, the model is a reasonable match with the observed range of phase proportions of most the phases in the natural residuum. Although there are textural and mineralogical observations in the samples that are not explicitly explained by the *T–X* diagram (ilmenite-hematite ratio in the rhombohedral oxide phase and the breakdown of hercynite to form crn-mt symplectite), the underlying principle that the model shows is that the residuum must have been oxidized, probably at a late

stage in its evolution, in order to produce the residuum mineral assemblages observed. We can use this same principle to explain the formation of the corundum–magnetite symplectites due to hercynite oxidation.

In a study highlighting the occurrence of sapphirine and quartz in the Salt Hill residuum, Caporuscio and Morse (1978) suggested that the coexistence of magnetite with a hematite-rich reintegrated bulk composition of exsolved ilm-hem grains suggested that oxygen fugacity was defined by the Fe-Ti oxide mineral assemblage and was well above FMQ, in fact approaching HM. In our samples, some of the hercynitic component of spinel in the residuum has clearly broken down to two phases, corundum and magnetite, nearby either magnetite or ilmeno-hematite crystals (**Fig. 3.4**). Additionally, it appears that in some places in the residuum, ilmeno-hematite has broken down to form rutile and magnetite via the oxidation reaction:

$$3\ Fe^{2+}TiO_3\ (\text{ilmenite}) + \tfrac{1}{2}\ O_2 = Fe_3O_4\ (\text{magnetite}) + 3\ TiO_2\ (\text{rutile}) \quad (3.2)$$

(see **Fig. B2**). It is possible that these textures are a result of down-temperature breakdown (oxidation) reactions of spinel (Equation 3.1) and ilmenite from peak temperature, ~ 1150 ˚C. **Figure 3.13** shows the reaction curves for Equations 3.1 (with a hercynite activity in spinel of 0.5) and 3.2 as well as MH and FMQ buffer curves in T–fO_2 space. The diagram illustrates the fact that the symplectites could have formed during cooling with either a fixed activity of oxygen *or* with increasing or decreasing fO_2. There are no hydrous phases present in the samples to suggest H_2O-rich fluid infiltration through the xenolith, so it is very possible that the oxidation is occurring anhydrously and the symplectite is simply a result of cooling.

3.6 Conclusions

This study successfully applies a series of calculated models to understand the formation of aluminous xenoliths from Salt Hill in the Cortlandt Complex. The series of models calculates melting a pelitic schist to produce (1) a lower-temperature silicate melt that yield a hybrid igneous rock composition upon mixing with a mafic melt, (2) quartzofeldspathic veinlets with phase compositions consistent with the observed veinlet phases, and (3) an aluminous xenolith assemblage consistent with the emery residuum observed in the natural samples. These results support previous studies on the production of siliceous melts via partial melting of pelitic rocks and on the formation of hybrid igneous rocks via pelitic assimilation and melt mixing between

mafic and siliceous melts. Textural observations of hercynite and ilmenite breakdown in the emery are believed to be a product of oxidation during cooling of the xenolith and further investigation should focus on the timing and processes of the formation of the breakdown textures. The xenolith samples from the Cortlandt Complex were produced in high pressure, UHT conditions similar to conditions in the lower-crust. Therefore we believe this study may shed some light on the possible ongoing processes and products in the mid- to lower crust.

3.7 Acknowledgements

We would like to thank Michael Brown for stimulating conversation concerning earlier modeling techniques and results.

3.8 References

Ackermand, D., Seifert, F. & Schreyer, W. (1975). Instability of sapphirine at high pressures. *Contributions to Mineralogy and Petrology* **50**, 79-92.

Asimow, P. D. & Ghiorso, M. S. (1998). Algorithmic modifications extending MELTS to calculate subsolidus phase relations. *American Mineralogist* **83**, 1127-1131.

Barker, F. (1964). Reaction between mafic magmas and pelitic schist, Cortlandt, New York. *American Journal of Science (1880)* **262**, 614-634.

Bender, J. F., Hanson, G. N. & Bence, A. E. (1984). Cortlandt Complex; differentiation and contamination in plutons of alkali basalt affinity. *American Journal of Science (1880)* **284**, 1-57.

Bons, P. D., Arnold, J., Elburg, M. A., Kalda, J., Soesoo, A. & van Milligen, B. P. (2004). Melt extraction and accumulation from partially molten rocks. *Lithos* **78**, 25-42.

Brown, M. (2001). Orogeny, migmatites and leucogranites: A review. *Journal of Earth System Science* **110.4**, 313-336.

Caporuscio, F. A. & Morse, S. A. (1978). Occurrence of sapphirine plus quartz at Peekskill, New York. *American Journal of Science (1880)* **278**, 1334-1342.

Coggon, R. & Holland, T. J. B. (2002). Mixing properties of muscovite-celadonite-ferroceladonite-paragonite micas and revised garnet-phengite thermobarometers. *Journal of Metamorphic Geology* **20**, 683-696.

Connolly, J. A. D. (2005). Computation of phase equilibria by linear programming: a tool for geodynamic modeling and its application to subduction zone decarbonation. *Earth and Planetary Science Letters* **236**, 524-541.

Diaz-Alvarado, J., Castro, A., Fernandez, C. & Ignacio Moreno-Ventas, I. (2011). Assessing bulk assimilation in cordierite-bearing granitoids from the Central System Batholith, Spain; experimental, geochemical and geochronological constraints. *Journal of Petrology* **52**, 223-256.

Domenick, M. A. & Basu, A. R. (1982). Age and origin of the Cortlandt Complex, New York: Implications from Sm-Nd data. *Contributions to Mineralogy and Petrology* **79**, 290-294.

Dorfler, K. M., Tracy, R. J. & Caddick, M. J. (2014). Late-stage orogenic loading revealed by contact metamorphism in the northern Appalachians, New York. *Journal of Metamorphic Geology* **32**, 113-132.

Friedman, G. M. (1956). *The origin of spinel-emery deposits, with particular reference to those of the Cortlandt Complex, New York*. Albany.

Ghiorso, M. S. & Sack, R. O. (1995). Chemical mass transfer in magmatic processes. IV. A revised and interally consistent thermodynamic model for the interpolation and extrapolation of liquid-solid equilibria in magmatic systems at elevated temperatures and pressures. *Contributions to Mineralogy and Petrology* **119**, 197-212.

Giordano, D., Russell, J. K. & Dingwell, D. B. (2008). Viscosity of magmatic liquids: A model. *Earth and Planetary Science Letters* **271**, 123-134.

Hensen, B. J. & Green, D. H. (1970). Experimental data on coexisting cordierite and garnet under high grade metamorphic conditions. *Physics of the Earth and Planetary Interiors* **3**, 431-440.

Hensen, B. J. & Green, D. H. (1971). Experimental study of he stability of cordierite and garnet in pelitic compositions at high pressures and temperatures: I, compositions with excess alumino-silicate. *Contributions to Mineralogy and Petrology* **33**, 309-330.

Hensen, B. J. & Green, D. H. (1972). Experimental study of the stability of cordierite and garnet in pelitic compositions at high pressures and temperatures; II, compositions without excess alumino-silicate. *Contributions to Mineralogy and Petrology* **35**, 331-354.

Hensen, B. J. & Green, D. H. (1973). Experimental study of the stability of cordierite and garnet in pelitic compositions at high pressres and temperatures III. Synthesis of experimental data and geological applications. *Contributions to Mineralogy and Petrology* **38**, 151-166.

Holland, T. J. B. & Powell, R. (1998). An internally consistent thermodynamic data set for phases of petrological interest. *Journal of Metamorphic Geology* **16**, 309.

Holland, T. J. B. & Powell, R. (2003). Activity-composition relations for phases in petrological calculations: an asymmetric multicomponent formulation. *Contributions to Mineralogy and Petrology* **145**, 492-501.

Johnson, A. M. & Tracy, R. J. (1998). Textural and chemical relations among spl-spr-grt-opx, Salt Hill emery mine, Cortlandt Complex, N.Y. *Eos (Richmond, Va.)* **79**, 360.

Johnson, T. E., Brown, M. & White, R. W. (2010). Petrogenetic modelling of strongly residual metapelitic xenoliths within the southern Platreef, Bushveld Complex, South Africa. *Journal of Metamorphic Geology* **28**, 269-291.

Johnson, T. E., White, R. W. & Brown, M. (2011). A year in the life of an aluminous metapelite xenolith - the role of heating rates, reaction overstop, H2O retention and melt loss. *Lithos* **124**, 132-143.

Kelsey, D. E., White, R. W., Holland, T. J. B. & Powell, R. (2004). Calculated phase equilibria in K2O-FeO-MgO-Al2O3-SiO2-H2O for sapphirine-quartz-bearing mineral assemblages. *Journal of Metamorphic Geology* **22**, 559-578.

Markl, G. (2005). Mullite-corundum-spinel-cordierite-plagioclase xenoliths in the Skaergaard Marginal Border Group: multi-stage interaction between metasediments and basaltic magma. *Contributions to Mineralogy and Petrology* **149**, 196-215.

Marschall, H. R., Dohman, R. & Ludwig, T. (2013). Diffusion-induced fractionation of niobium and tantalum during continental crust formation. *Earth and Planetary Science Letters* **375**, 361-371.

Maury, R. C. & Bizouard, H. (1974). Melting of acid xenoliths into a basanite: an approach to the possible mechanisms of crustal contamination. *Contributions to Mineralogy and Petrology* **48**, 275-286.

McBirney, A. R. (2007). *Igneous Petrology*. Sudbury, MA: Jones and Bartlett Publishers, Inc.

Newton, R. C. (1972). An experimental determination of the high-pressure stability limists of magnesian cordierite under wet and dry conditions. *Journal of Geology* **80**, 398-420.

Patino Douce, A. E. & Beard, J. S. (1995). Dehydration-melting of Biotite Gneiss and Quartz Amphibolite from 3 to 15 kbar. *Journal of Petrology* **36**, 707-738.

Powell, R. & Holland, T. J. B. (1988). An internally consistent dataset with uncertainties and correlations: 3. Applications to geobarometry, worked examples and a computer program. *Journal of Metamorphic Geology* **6**, 173-204.

Powell, R. & Holland, T. J. B. (1994). Optimal geothermometry and geobarometry. *The American Mineralogist* **79**, 120.

Powell, R. & Holland, T. J. B. (1999). Relating formulations of the thermodynamics of mineral solid solutions: Activity modeling of pyroxenes, amphiboles, and micas. *American Mineralogist* **84**, 1-14.

Powell, R. & Holland, T. J. B. (2008). On thermobarometry. *Journal of Metamorphic Geology* **26**, 155-179.

Powell, R., Holland, T. J. B. & Worley, B. (1998). Calculating phase diagrams with THERMOCALC: methods and examples. *Journal of Metamorphic Geology* **16**, 577-588.

Preston, R. J., Dempster, T. J., Bell, B. R. & Rogers, G. (1999). The petrology of mullite-bearing peraluminous xenoliths: Implications for contamination processes in basaltic magmas. *Journal of Petrology* **40**, 549-573.

Ratcliffe, N. M., Armstrong, R. L., Mose, D. G., Seneschal, R., Williams, N. & Baiamonte, M. J. (1982). Emplacement history and tectonic significance of the Cortlandt Complex, related plutons, and dike swarms in the Taconide Zone of southeastern New York based on K-Ar and Rb-Sr investigations. *American Journal of Science (1880)* **282**, 358-390.

Ratcliffe, N. M., Tucker, R. D., Aleinikoff, J. N., Amelin, Y., Merguerian, C. M. & Panish, P. T. (2012). U-Pb zircon and titanite ages of late-to post-tectonic intrusions of the Cortlandt-Beemerville magmatic belt, CN, NY, and NJ: relation to Iapetan closure in the Taconian orogeny. *Geological Society of America Abstracts with Programs* **44**, 73.

Rogers, G. S. (1911). Geology of the Cortlandt Series and it's Emery Deposits. *Annals New York Academy of Science* **21**, 11-86.

Sparks, R. S. J. & Marshall, L. A. (1986). Thermal and mechanical constraints on mixing between mafic and silicic magmas. *Journal of Volcanology and Geothermal Research* **29**, 99-124.

Taylor-Jones, K. & Powell, R. (2010). The stability of sapphirine plus quartz: calculated phase equilibria in FeO-MgO-Al2O3-SiO2-TiO2-O. *Journal of Metamorphic Geology* **28**, 615-633.

Theriault, R. D., Barnes, S.-J. & Severson, M. J. (1997). The influence of country-rock assimilation and silicate to sulfide ratios (*R* factor) on the genesis of the Dunka Road Cu–Ni–platinumn-group element deposit, Duluth Complex, Minnesota. *Canadian Journal of Earth Sciences* **34**.

Tracy, R. J. (2009). High pressure crystallization of mafic magma: field observations, compositional measurements and computer modeling. *Eos Trans. AGU*.

Tracy, R. J. & McLellan, E. L. (1985). A natural example of the kinetic controls of compositional and textural equilibration. *A.B. Thompson and D.C. Rubie, Eds., Metamorphic reactions; kinetics, textures, and deformation* **4**, 118-137.

Waldron, K. A. (1986). High pressure contact metamorphism in the aureole of the Cortlandt Complex, southeastern New York. *Geology*: Yale University.

White, R. W., Pomroy, N. E. & Powell, R. (2005). An in situ metatexite–diatexite transition in upper amphibolite facies rocks from Broken Hill, Australia. *Journal of Metamorphic Geology* **23**, 579–602.

White, R. W., Powell, R. & Clarke, G. L. (2002). The interpretation of reaction textures in Fe-rich metapelitic granulites of the Musgrave Block, central Australia: constraints from mineral equilibria calculations in the system K_2O–FeO–MgO–Al_2O_3–SiO_2–H_2O–TiO_2–Fe_2O_3. *Journal of Metamorphic Geology* **20**, 41-55.

White, R. W., Powell, R. & Holland, T. J. B. (2001). Calculation of partial melting equilibria in the system Na_2O-CaO-K_2O-FeO-MgO-Al_2O_3-SiO_2-H_2O (NCKFMASH). *Journal of Metamorphic Geology* **19**, 139-153.

White, R. W., Powell, R. & Holland, T. J. B. (2007). Progress relating to calculation of partial melting equilibria for metapelites. *Journal of Metamorphic Geology* **25**, 511-527.

White, R. W., Powell, R., Holland, T. J. B. & Worley, B. (2000). The effect of TiO_2 and Fe_2O_3 on metapelitic assemblages at greenschist and amphibolite facies conditions: mineral equilibria calculations in the system K_2O-FeO-MgO-Al_2O_3-SiO_2-H_2O-TiO_2-Fe_2O_3. *Journal of Metamorphic Geology* **18**, 497-511.

3.9 Figures

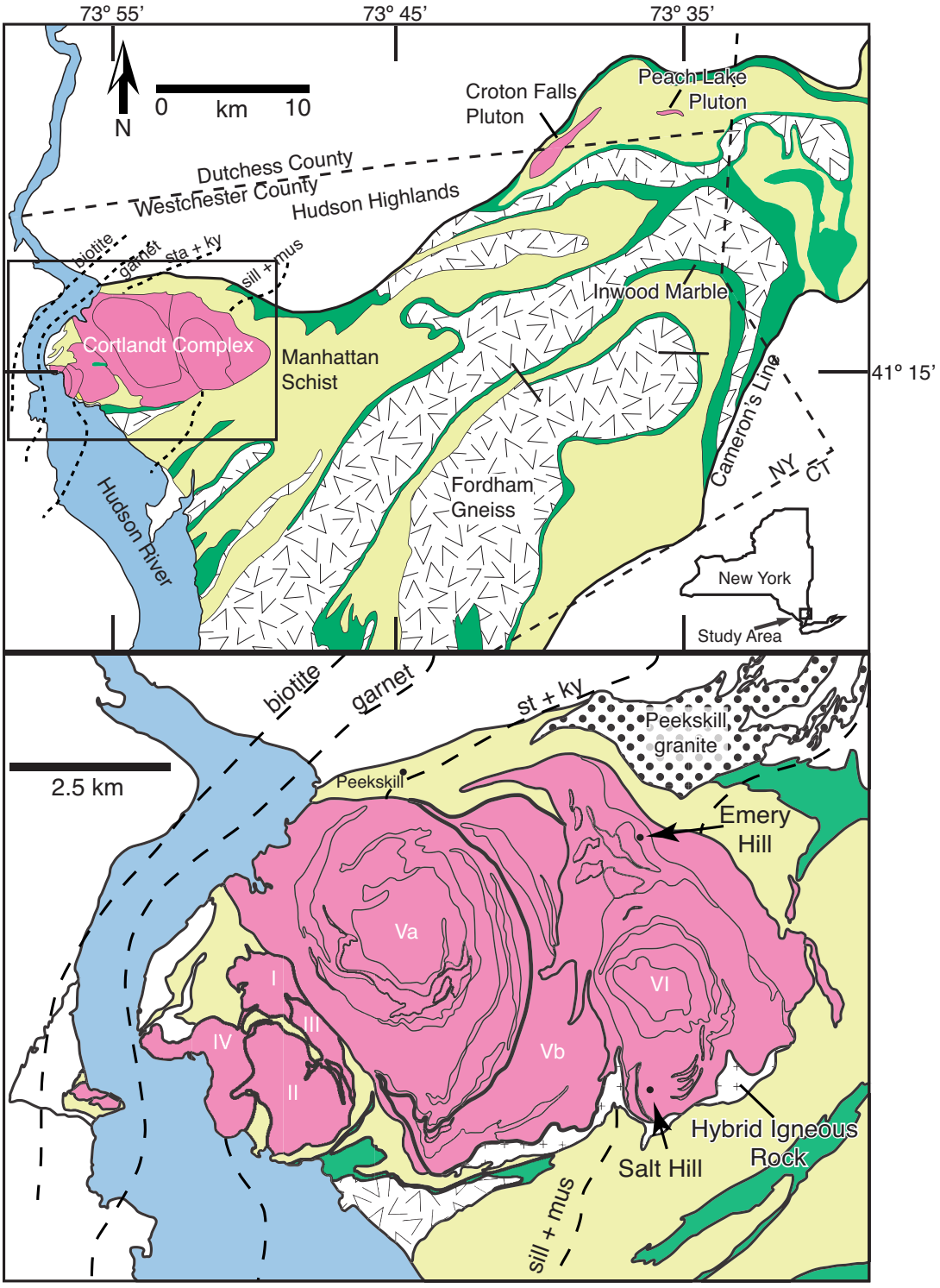

Figure 3.1. Simplified geologic map of the Cortlandt Complex and Manhattan Prong. Plutons outlined in bold black lines. Thin lines within each pluton indicate cumulate layering.

Figure 3.2. Close up of hand sample of the emery outlining the two chemically and physically segregated materials. The white outlined sections are the quartzofelspathic veinlets, which are chemically and physically segregated from the darker, Al-rich residuum. Rock hammer handle for scale.

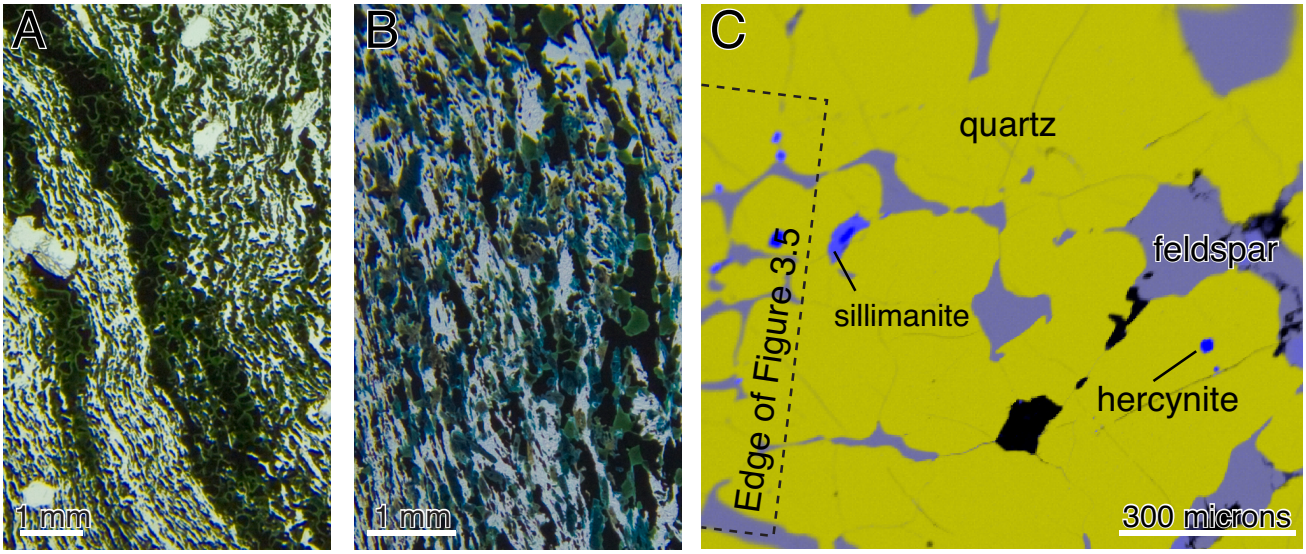

Figure 3.3. Examples of different types of residuum and texture of the quartz veinlets. (a) sapphirine-free, spinel-rich residuum. Spinel is green, rhombohedral oxides are black, large white crystals are corundum, white fibrous crystals are sillimanite. (b) sapphirine-rich residuum. Blue and tan crystals are sapphirine, black crystals are rhombohedral oxides, large green crystals are spinel, colorless crystals are sillimanite. (c) false-color EDS image of quartzofeldspathic vein. Yellow crystals are quartz, light blue material between quartz crystals is ternary feldspar. Sillimanite and hercynite is sometimes present in rounded quartz crystals. The edge of Figure 3.5 is shown for reference.

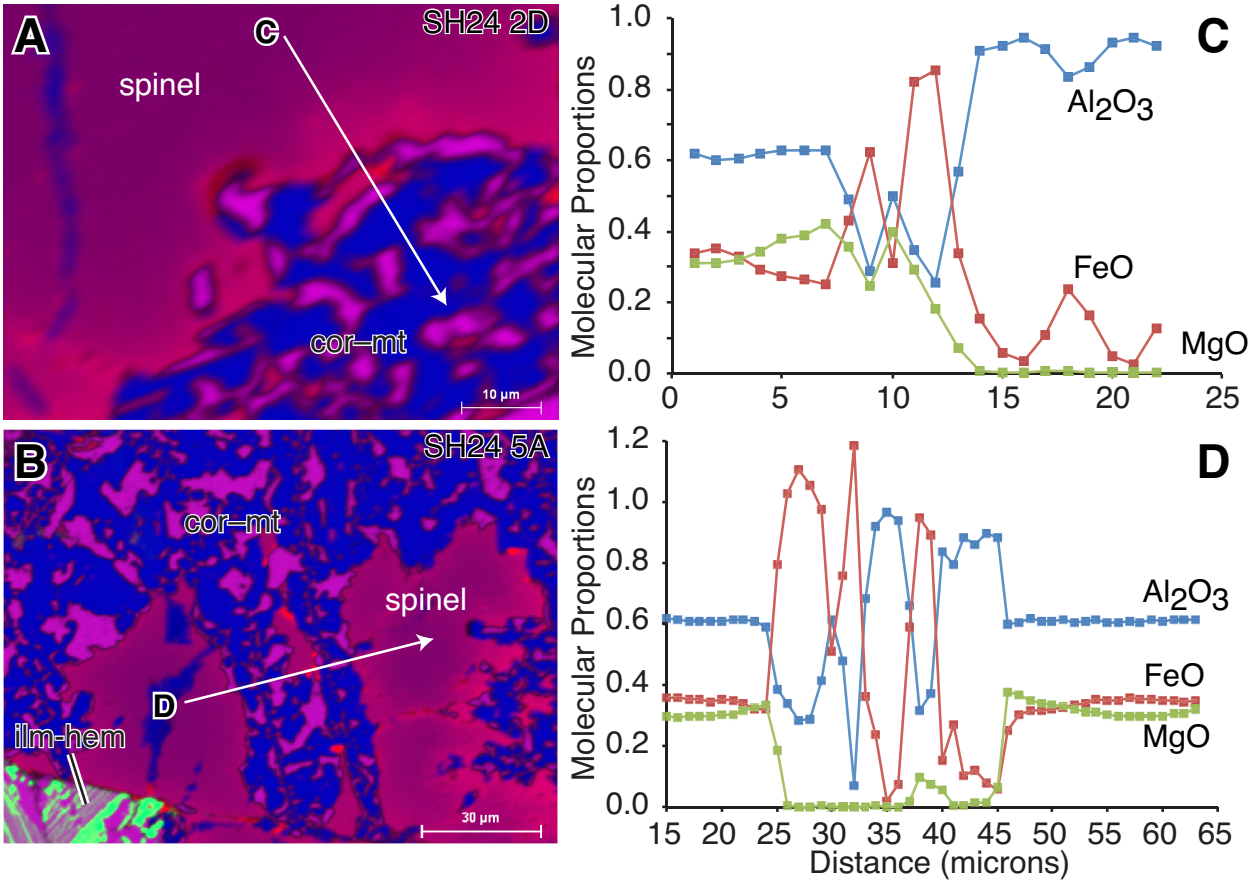

Figure 3.4. Chemical map overlays and traverses across corundum–magnetite symplectites. Colors in panel (a) and (b) correspond to: Al – blue, Fe – pink, Mg – red, Ti – green. The increase in brightness in the spinrl crystal toward the symplectite represent a decreasing Fe/Fe+Mg in the spinel. Quantitative traverses in panels (c) and (d) of the molecular proportions of oxides correspond to the traverses drawn on panels (a) and (b).

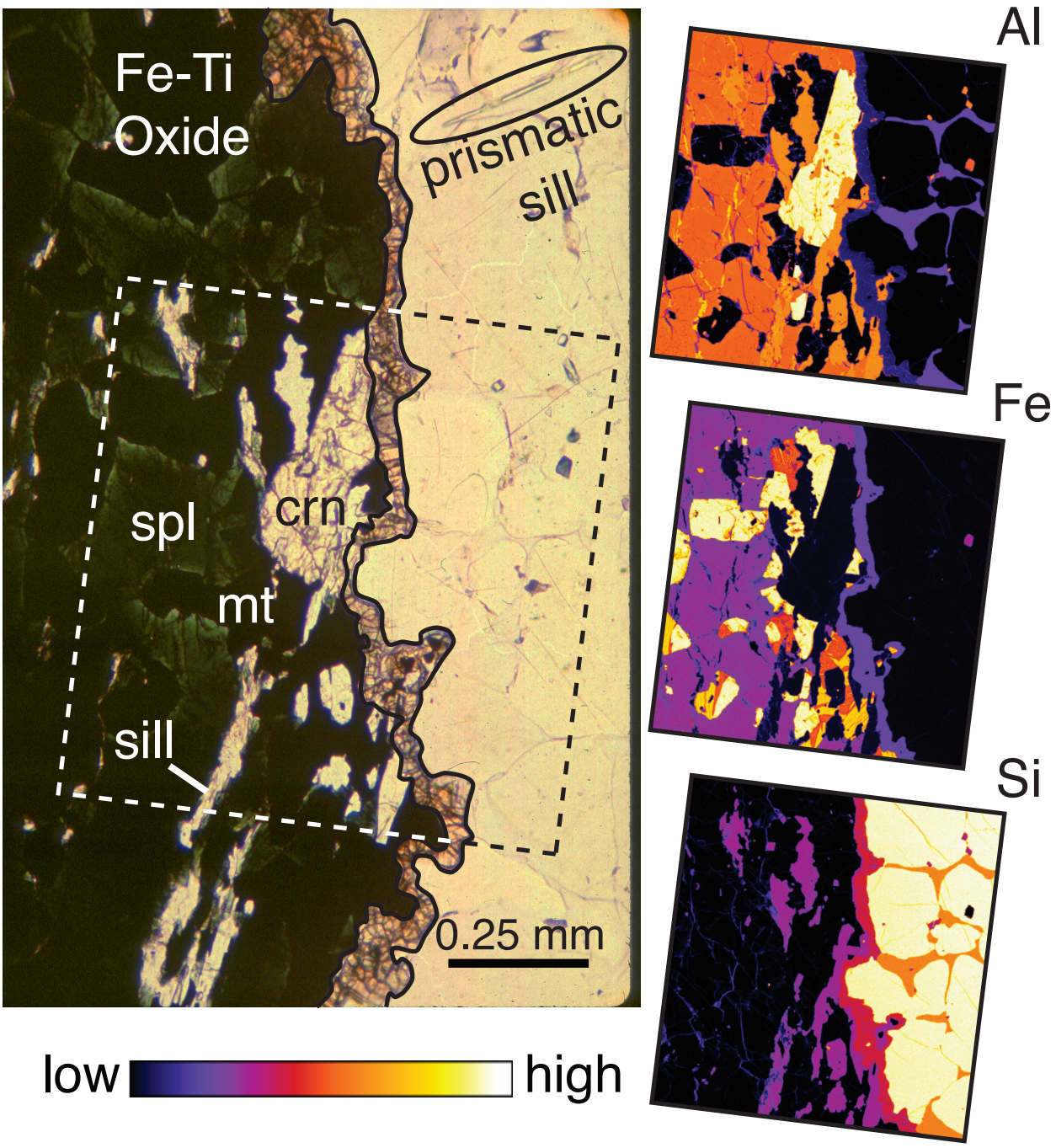

Figure 3.5. Part of a thin section micrograph showing the orthopyroxene rimming texture between residuum and quartzofeldspathic veinlet. WDS chemical images show the relative abundance of elements in the dotted area of the micrograph.

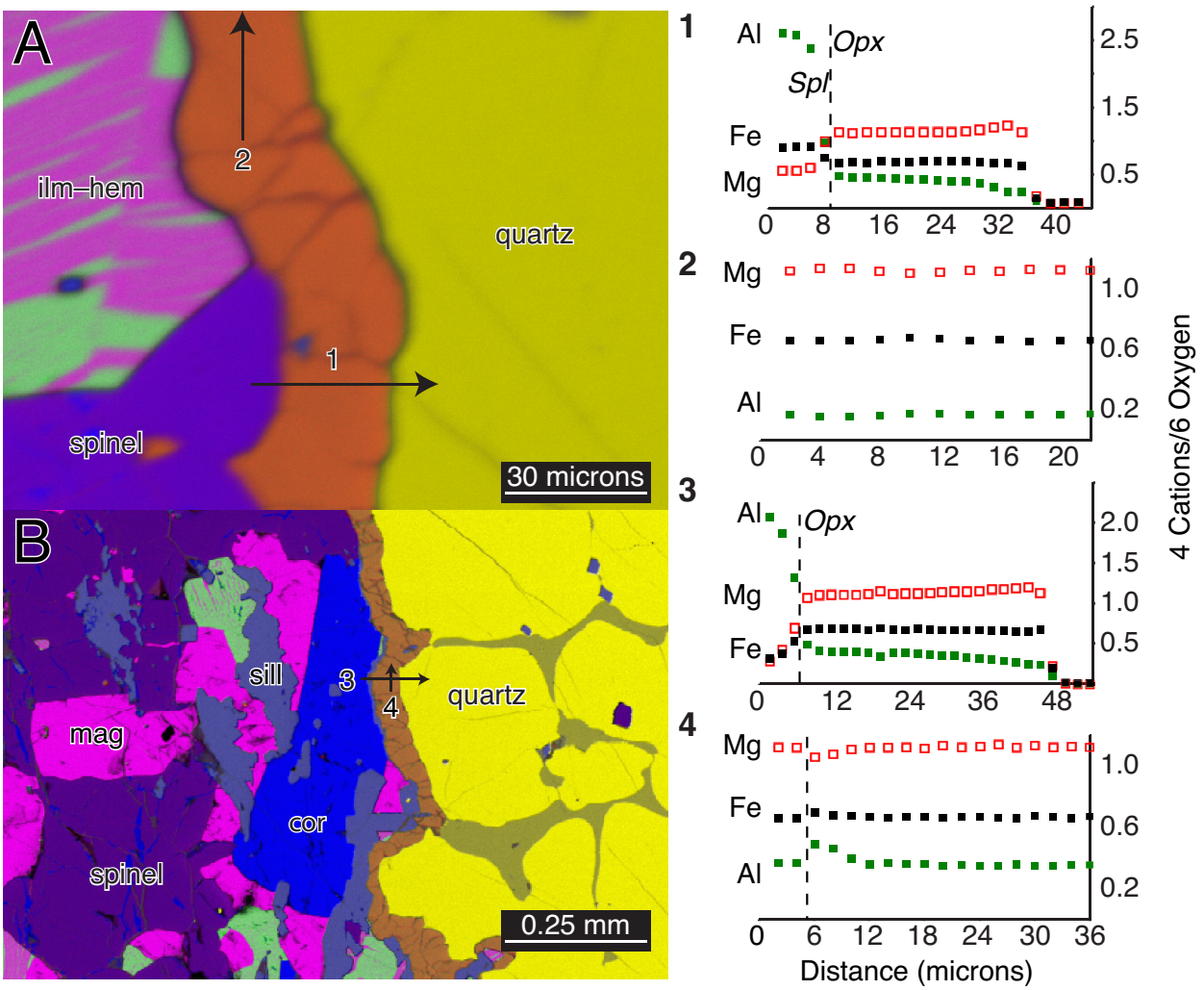

Figure 3.6. Traverses across an orthopyroxene selvage. Traverses 1 and 2 are shown in panel (a), traverses (3) and (4) shown in panel (b). The composition of the orthopyroxene is unchanging in traverses parallel to the vein–residuum boundary (traverses 2 and 4). Al content shows a steady decrease in content in traverses (1 and 3) toward the quartzofeldspathic side. Dotted line in traverse 4 corresponds to a crack in the orthopyroxene. See text for additional information.

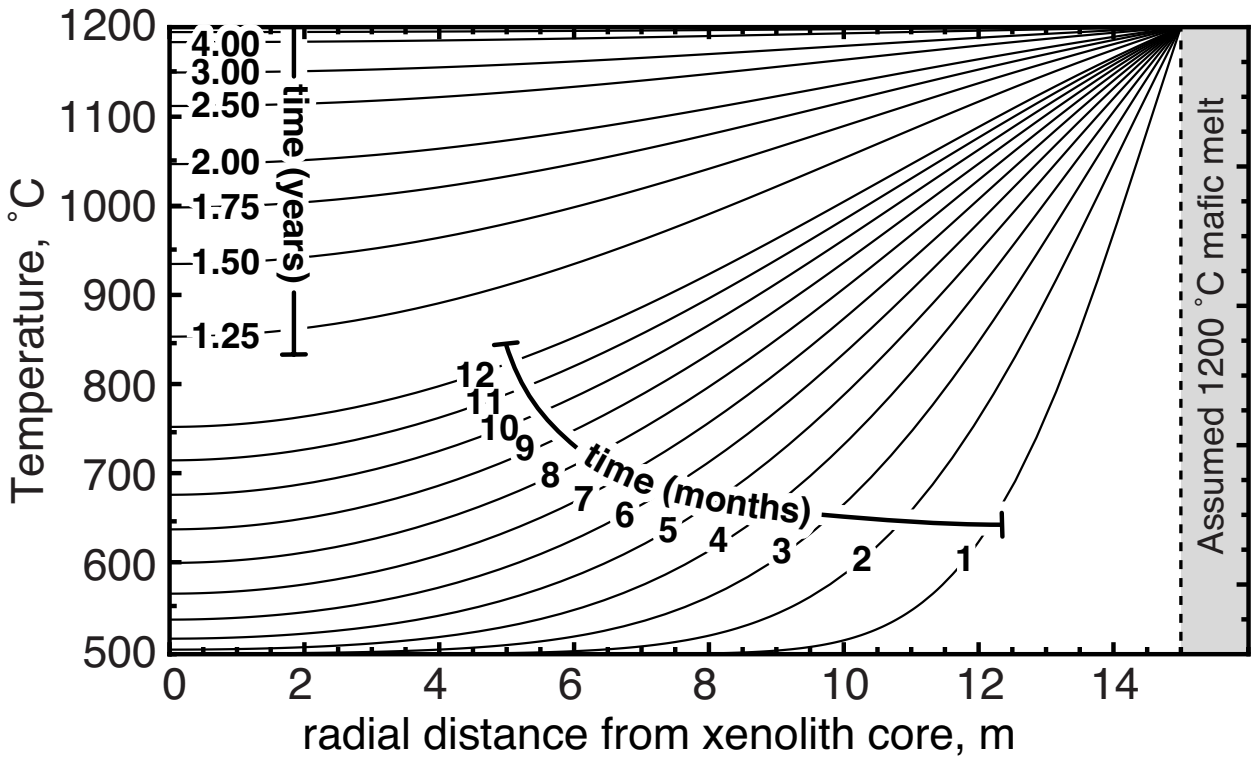

Figure 3.7. A 1-D heat conduction modeling assuming a 30m diameter spherical xenolith with an initial *T* of 500 ˚C and an infinite, non-cooling reservoir of magma at 1200 ˚C. Model predicts that core of the xenolith would reach magmatic temperatures in about 3 years.

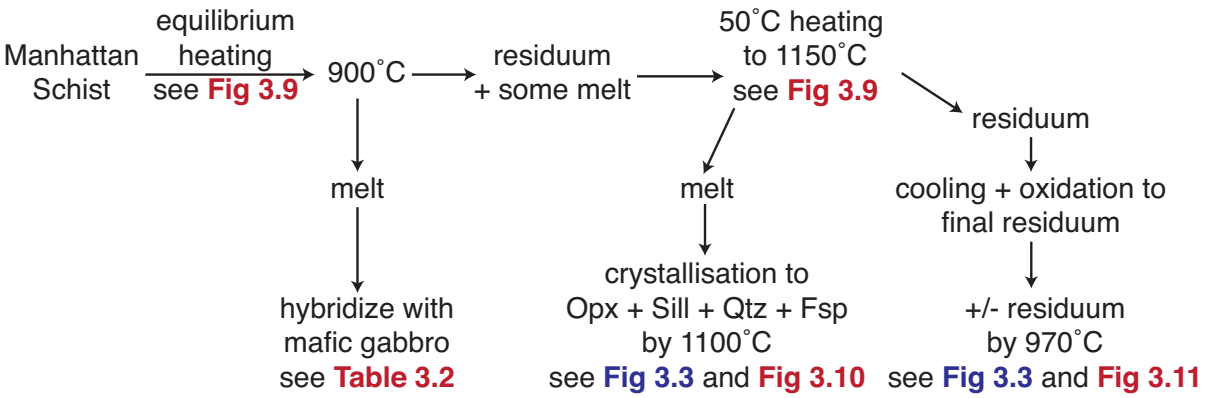

Figure 3.8. Flow chart showing progression of modeling techniques used to produce the hybrid monzonorite, quartzofeldspathic veinlets and aluminous residuum. Figures and Tables that correspond to the appropriate calculation for each stage are indicated in red. Figures of images of the material that correspond to the end results (veinlets or residuum) are indicated in blue.

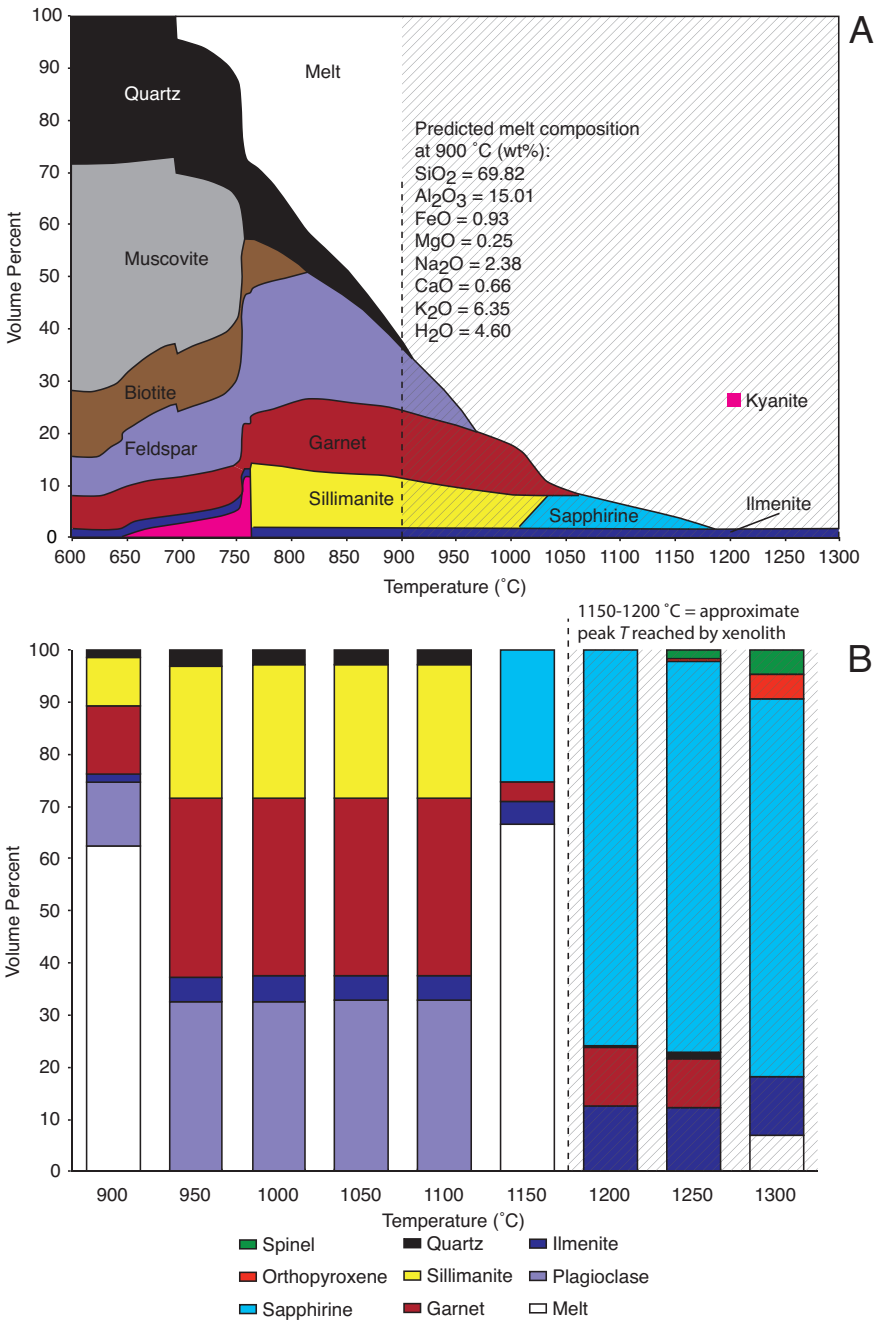

Figure 3.9. Phase abundances calculated from a 1D (isobaric at 0.9 GPa) pseudosection. (a) Gibbs free energy minimizations were in 1 ˚C intervals, and a constant bulk composition of the Manhattan Schist (Table 3.**1**) was assumed. Activity–composition models used are listed in the text. Note that 'feldspar' combines plagioclase and alkali feldspars. (b) Phase abundances calculated in 50 ˚C intervals, with recasting of the bulk composition to simulate extraction of melt produced at any step. Note that the 900 ˚C calculation is identical to the result at 900 ˚C in panel (a). Hashed areas to the right of the dotted line represents the part of the calculation not applicable to this study (see text for details). Composition of melt and residuum at 1150 ˚C is used in cooling (Fig 3.10) and T–X_{O2} (Fig 3.11) calculations.

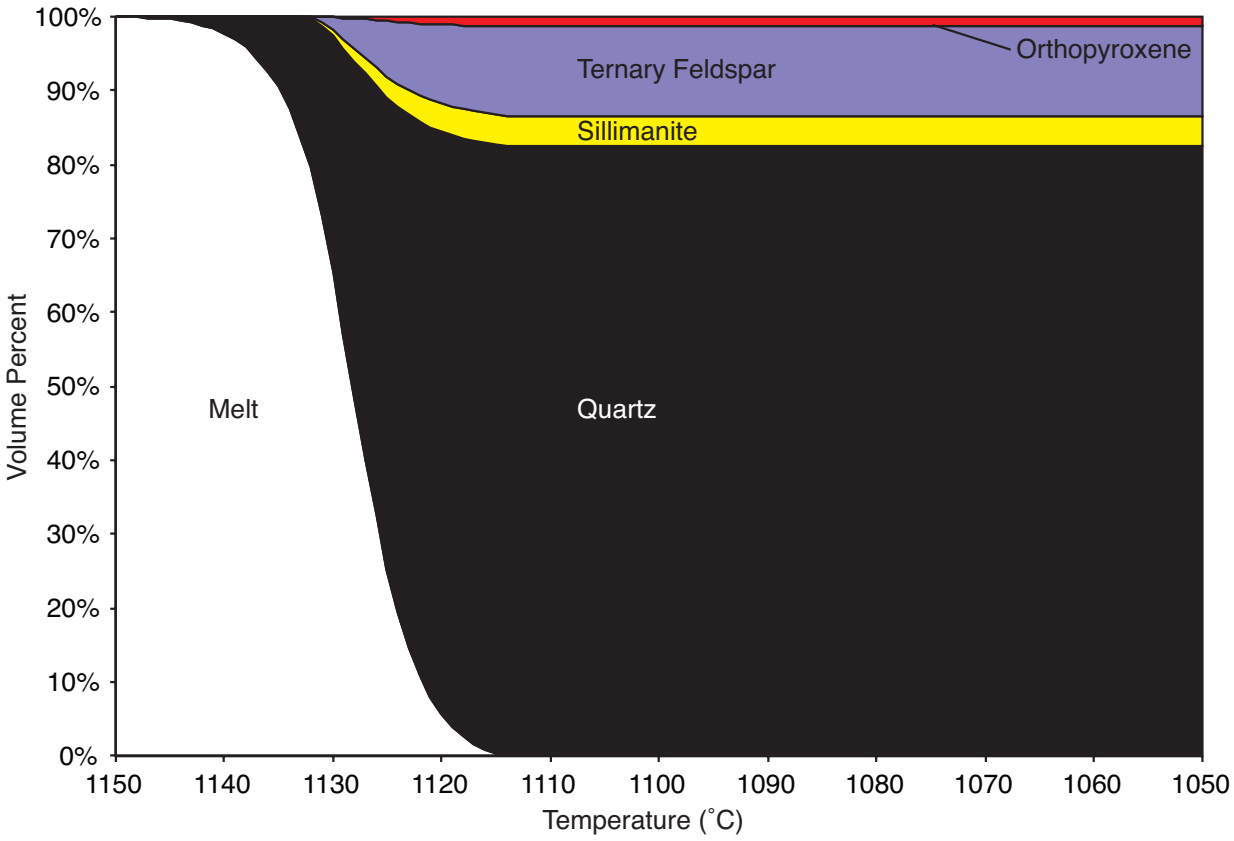

Figure 3.10. Cooling model with phase abundances calculated from a 1D (isobaric at 0.9 GPa) pseudosection. Gibbs free energy minimizations were in 1 ˚C intervals, and a starting bulk composition of the melt produced at 1150 ˚C in Fig. 3.9B was used. 25 % of the calculated volume of melt was extracted at each step (see text for details). All solid phases included in other calculations were considered here, but only four were found to be stable.

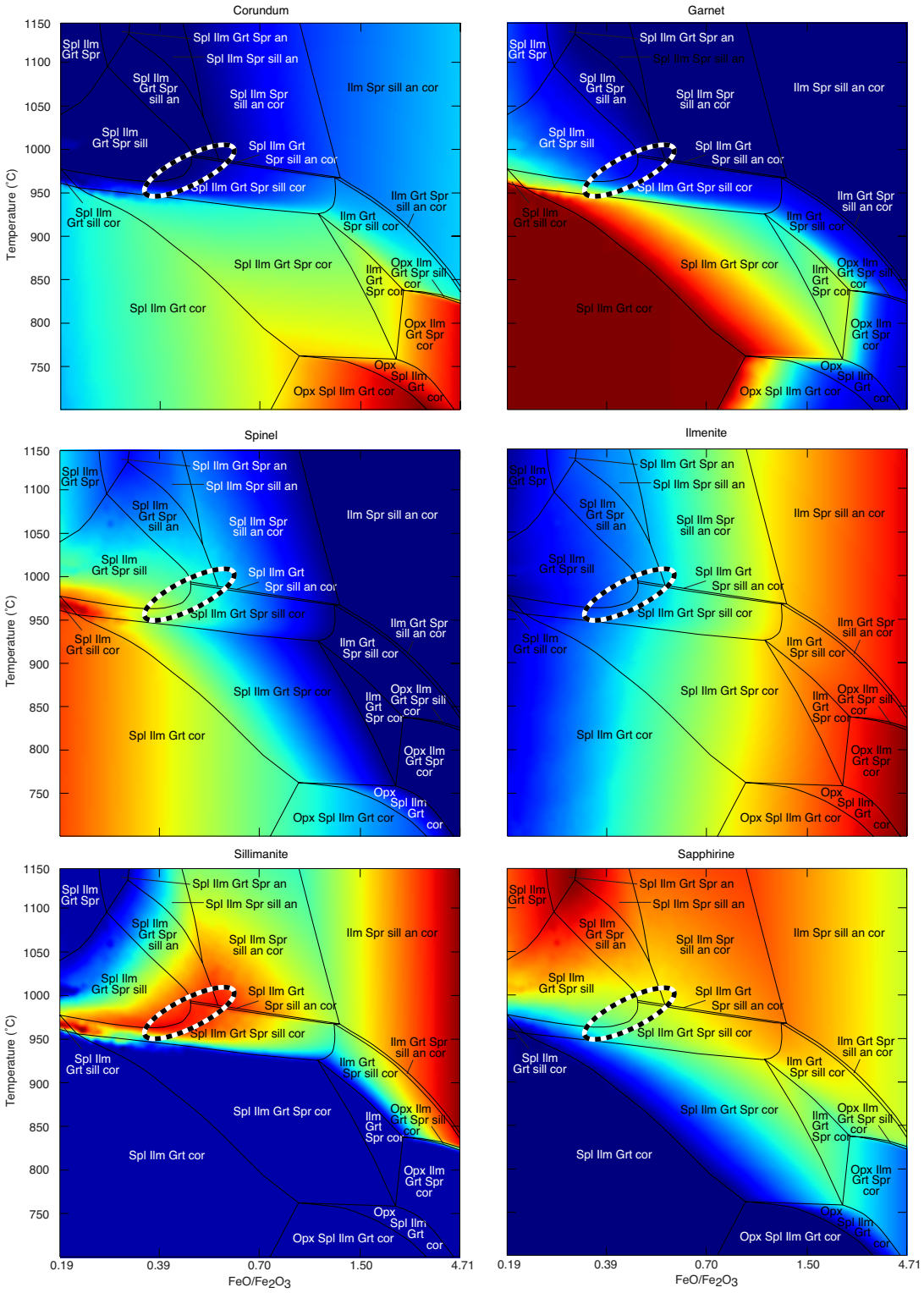

Figure 3.11. *T–X* diagrams with phase abundances contoured for corundum, garnet, spinel, ilmenite, sillimanite and sapphirine (warm colors indicate high phase abundance, cold colors indicate absence of phase). Dotted circle denotes area where phase abundances most closely match the residuum samples.

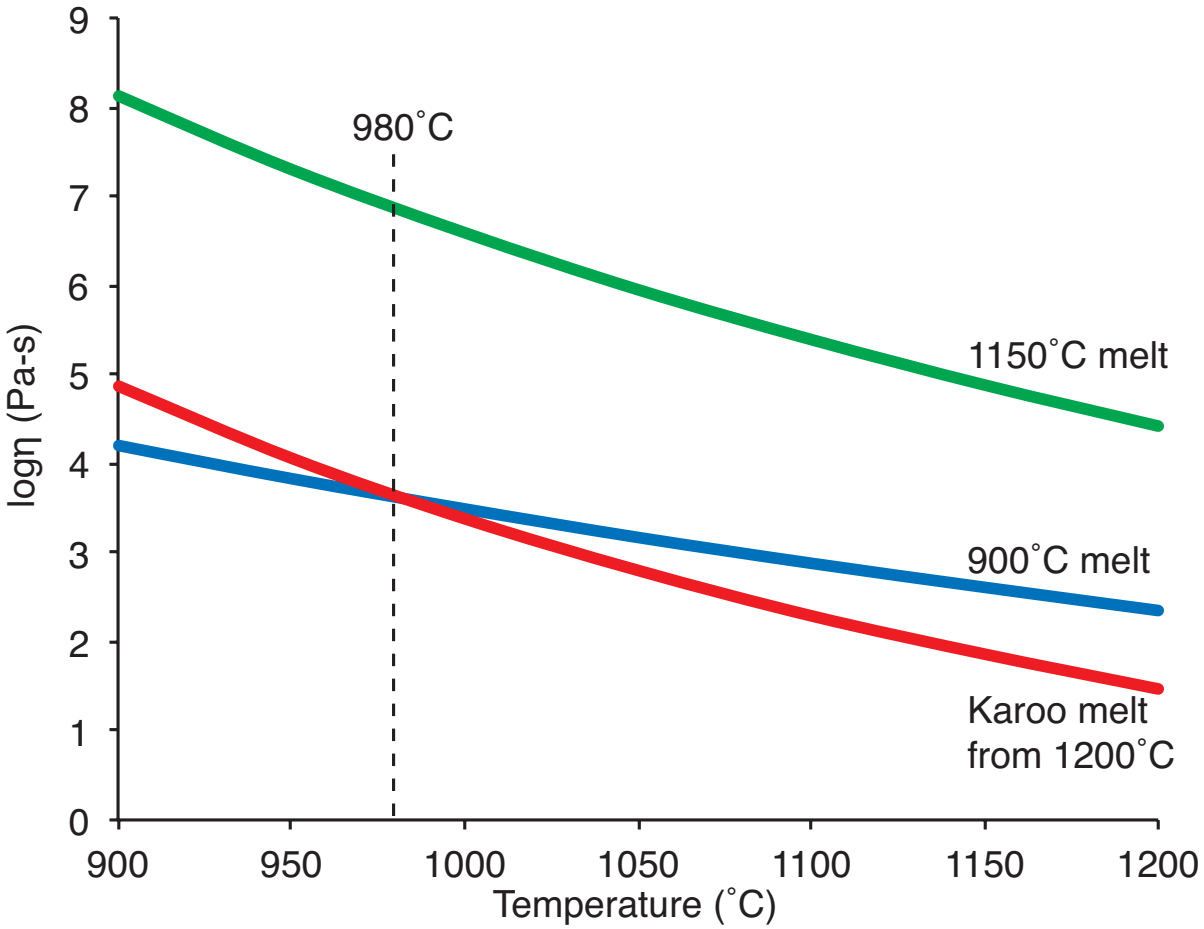

Figure 3.12. Calculated viscosities for melts produced in the modeling scenario. Calculated melt composition at 900 ˚C from the equilibrium heating model (Fig 3.9A) has the same viscosity as the estimated Mg-rich mafic magma at 980 ˚C (dotted line). High-*T* melt produced at 1150 ˚C (see Fig 3.9B) does not reach viscosities close to the lower-*T* partial melt or the mafic magma in this temperature range.

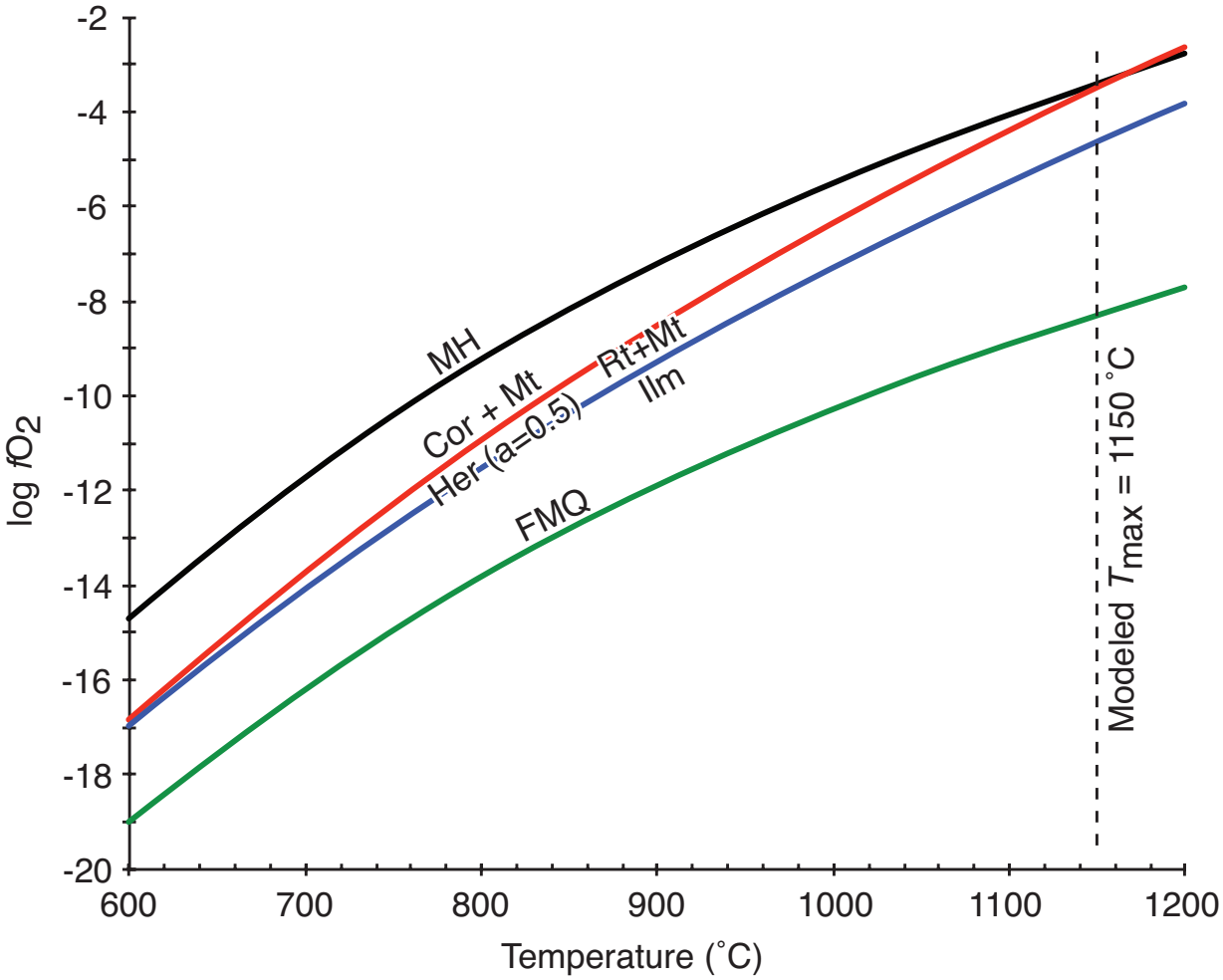

Figure 3.13. T–f_{O2} diagram with appropriate buffers (after Tsujimori & Ishiwatart, 2002). Ilmenite oxidation to rutile + magnetite is indicated by blue line. Hercynite oxidation (with a her activity of 0.5) to corundum + magnetite is indicated by red line. FMQ and MH buffers shown. Reaction curves illustrate that the textures observed in the samples could be a product of cooling from predicted maximum temperature (~ 1150 ˚C) under stable f_{O2} conditions.

3.10 Tables

Oxide	#23 (wt%)	#24 (wt%)	#25 (wt%)	#26 (wt%)	#27 (wt%)
SiO_2	57.94	62.98	61.57	55.12	40.16
Al_2O_3	21.70	16.88	19.53	24.32	29.50
Fe_2O_3	1.57	2.48	5.44	6.13	19.66
FeO	5.90	5.00	2.61	4.99	5.80
MgO	2.49	1.58	1.90	Trace	Trace
CaO	0.58	Trace	Trace	Trace	0.85
Na_2O	1.74	3.02	3.48	2.71	1.46
K_2O	4.68	7.45	2.14	2.83	1.36
H_2O +	2.17	–	–	–	–
H_2O -	0.29	–	–	–	–
CO_2	Trace	–	–	–	–
TiO_2	1.01	–	1.53	2.46	–
P_2O_5	Trace	Trace	Trace	Trace	Trace
S	–	0.08	0.85	1.23	0.82
Cr_2O_3	–	–	–	–	–
MnO	0.19	–	–	–	–
Sum	100.26	99.47	99.05	99.79	99.61

Table 3.1. Manhattan Schist analyses from Rogers (1911). Analysis #23 is a composite analysis of five specimens from various points beyond the borders of the series. Analyses #24–27 are individual analyses from schist samples near the Cortlandt Complex

Oxide (wt%)	Calculated melt at 900 ˚C	Karoo melt calculated at 1200 ˚C	Average monzonorite	39% Silica-rich melt, 61% Karoo
SiO_2	69.82	44.54	54.59	54.49
TiO_2	0.00	2.68	1.62	1.63
Al_2O_3	15.00	15.71	14.11	15.43
Fe_2O_3	0.00	2.05	1.23	1.24
FeO	0.93	11.93	8.51	7.60
MnO	0.00	0.17	0.08	0.10
MgO	0.25	6.58	6.79	4.09
CaO	0.66	9.14	6.43	5.80
Na_2O	2.38	2.88	2.32	2.68
K_2O	6.35	1.31	3.22	3.29

Table 3.2. Melt mixing results. Average monzonorite composition calculated by averaging two bulk chemical analyses of two separate monzonorite samples

Chapter 4

The Missing Corundum Conundrum: Is the Presence of Hybrid Rocks Evidence for UHT Metamorphism?

K.M. Dorfler[1], J.S. Beard[2], Tracy, R.J.[1], M.J. Caddick[1]

[1]*Department of Geosciences, Virginia Polytechnic Institute and State University, Blacksburg, VA 24061, USA*
[2]*Virginia Museum of Natural History, Martinsville, VA 24112, USA*

This article may be submitted to *Geology* for publication

Abstract: Hybrid or intermediate igneous rocks are a direct result of partial crustal melting and melt mixing with mafic magma. Monzonorite found at the Cortlandt Complex, NY formed via mixing with a mantle-derived, fractionally crystallized mafic melt and are intimately related to the production of UHT aluminous 'emery' xenoliths. Although hybrid igneous rocks are commonly found in igneous and metamorphic terranes world-wide, residual pelitic material is much less ubiquitous due to the mantle-like densities of the emery. Density calculations and observations of emery placement within the Cortlandt Complex suggest that the presence of emery is due to erosion of the complex to the deepest portions of the magma chamber. Due to the temperature, pressure and bulk-rock chemistry associated with production of the xenoliths, it is likely emery is much more widespread in the Earth's lower crust or along the lower crust–mantle boundary, but the only evidence that typically remains at shallower crustal levels is the presence of hybrid igneous rocks.

4.1 Introduction

Hybrid igneous rocks such as norites, diorites, and tonalities are associated with contamination of mafic magma by partial melting of crustal rocks (Alasino et al., 2014; Diaz-Alvarado et al., 2011; Duchesne et al., 1989; Theriault et al., 1997). Recent studies on pelitic xenolith assimilation focus on the production of 'granitic' melts from partial melting of pelites and the interaction of that melt with mafic magma (Johnson et al., 2010; Preston et al., 1999). Such interaction can result in the formation of a hybrid igneous rock such as monzonorite, or monzodiorite. Chapter three of this dissertation successfully reports thermodynamic and mathematical models that replicate the formation and chemistry of a natural sample of monzonorite. However, the results imply that only the initial partial melt produced during the melting of a pelite to UHT conditions will be able to mix with a mafic melt to produce a hybrid rock. Therefore, norites produced via xenolith assimilation should be associated with a residual, unmelted material similar in composition to the Salt Hill emery xenoliths of the Cortlandt Complex (aluminum-, iron- and titanium-enriched, silica- and alkali-depleted material with a typical assemblage of spinel–magnetite–ilmeno-hematite–sillimanite±sapphirine±corundum). If so, why are hybrid igneous rocks more commonly found in nature than the residual 'emery' compositions?

In this contribution we speculate on the evolution of a pelite during heating in terms of the changes in density and how it dictates eventual placement of the hybrid rocks and unmelted pelitic residuum. Many hybrid igneous rock occurrences may be the traces of pelite assimilation in mafic magma, but due to the density of the residual material, the (possibly very common) emery sinks to unexposed depths possibly as low as the crust–mantle boundary.

4.2 How Are Hybrid Rocks Formed?

There are several possible ways of making a hybrid or intermediate igneous rocks, including: fractional crystallization of a mafic melt; mixing mafic melt with Si-enriched melt; partial melting of a pre-existing mafic rock; or direct melting of subducted sediments. In a recent study on the abundance of andesites in arc magmas, trace element analysis imply that fractionation of a mafic melt coupled with lower crustal assimilation is a fundamental process in producing intermediate compositions (Lee and Bachmann, 2014). Additionally, studies in other tectonic settings (e.g. the Central System Batholith in Spain, Rogaland in SW Norway, Duluth Complex in Minnesota, USA) report that the presence of hybrid rocks is likely due to crustal assimilation and partial melting via a mafic melt (Diaz-Alvarado et al., 2011; Duchesne et al., 1989; Theriault et al., 1997).

Detailed discussion on the formation of hybrid rocks, such as norite, goes back to at least the early 20th century. In *The Evolution of the Igneous Rocks*, Bowen describes norites as the product of assimilation of pelite in basaltic magma (Bowen, 1928) and references the presence of norites around inclusions of aluminous material in the Cortlandt Complex. Due to chemical saturation limitations of mafic melt, he proposed that it is impossible to have a hybrid rock that is purely the sum of a mafic magma and molten pelite. Therefore, the intermediate rocks are actually a function of melt fractionation with some input from melt derived from a "slate" material – an observation that continues to be reported in many other terranes nearly 100 years later.

It is generally thought that mixing mafic and felsic melts is not an efficient way of producing intermediate rocks due to the fact that mafic melts will likely solidify when they come in contact with a felsic melt (Caricchi et al., 2007; Sparks and Marshall, 1986). However, as was shown in chapter three, as a pelite melts, the composition of the partial melt will change depending on the extent of melting and melt removal. Hence, only some fraction of a pelite-derived melt would compositionally and rheologically be able to mix with a mafic magma to produce a hybrid rock. This may not necessarily be a 'granitic' melt, but a melt with a generally higher silica and alkali content than the mafic melt it mixes with to produce an intermediate assemblage.

If partial crustal assimilation is a common process, then why is the non-melted residuum frequently absent in nature? An obvious explanation is that the density of the refractory material is much higher than the surrounding material, causing the residuum to sink to lower depths of the crust. Using the compositions of the calculated products from chapter three, we calculate the densities of the materials produced during melting of a pelite, speculate on the eventual placement the residuum, and discuss the potential implications on lower crust–mantle dynamics.

4.3 Density Discrepancies and Deep Descents

The emery xenoliths at the Cortlandt Complex are silica-deficient aluminous xenoliths that formed via UHT (≥ 1150 ˚C) heating of a Manhattan Schist protolith (quartz-rich aluminous schist) by the mafic magma of the pluton. Density calculations were performed on predicted residuum and melt products from isobaric heating models of a Manhattan Schist composition at 0.9 GPa calculated using Perple_X 6.6.8 (Connolly, 2005; dataset and modifications used in these calculations are outlined in chapter three). **Fig. 4.1** shows density values for the system (residuum + melt) and melt compositions predicted to form at every interval in which phase equilibria was calculated.

As the pelite heats and eventually melts, density decreases relatively steadily (there is a jump in density values for the system between 750–760 ˚C that correlates to muscovite- and kyanite-out reactions). From $T \geq 900$ ˚C, phase equilibria is calculated in 50 ˚C intervals and any stable melt is removed in each step, therefore from 900–1300 ˚C, the density values are displayed as dots for the system and melt in **Figure 4.1**. At 900 ˚C, there is a sharp density increase (from 2.6–3.2 g-cm^{-3}) for the system. This is because any predicted amount of melt is removed, leaving behind just the residuum material. Density remains generally constant until a sharp drop at 1150 ˚C, where the system reaches its new solidus and anhydrous silica-rich melt forms. However, phase equilibria calculated above 1150 ˚C effectively removes that melt, thus the density of the residuum increases to ~ 3.8 g-cm^{-3}. In the melt modeling calculations performed in chapter three, the composition of the melt and residuum at 1150 ˚C were used in separate cooling calculations that produced compositions and textures that emulate the natural samples. The density of only the residuum at 1150 ˚C is ~ 3.8 g-cm^{-3}, as indicated by the blue star in **Figure 4.1**.

Typical crustal density values range from 2.2–2.9 g-cm^{-3}, whereas upper mantle densities range from 3.4–4.4 g-cm^{-3} (Anderson, 1989). The density of the predicted emery residuum is closer to (and possibly higher than) typical upper mantle values, implying that during heating, the residual material most likely descended through the magma until it was prevented from moving any deeper. This "response to gravity", as termed by Bowen (1928), is why we believe emery is rare at the surface but possibly very common in the lower crust or upper mantle.

4.4. Emery Exposure at the Cortlandt Complex

If pelitic residuum material has densities comparable to the upper mantle, then why is it exposed at the present-day surface at Salt Hill? A simplified geologic map of the Cortlandt Complex (**Fig 4.2**) shows that the Salt Hill xenoliths are located at the very southeasternmost edge of the complex, in pluton VI. In addition to the xenoliths, the area is also host to hybrid igneous rocks along the contact between the mafic pluton and the country rock and cumulate olivine-pyroxenite layers within the pluton. Thermobarometric studies in contact aureoles around plutons contemporaneous to the Cortlandt Complex indicate that the pressure at the current level of erosion was ~ 0.9 GPa at the time of pluton emplacement, or about 30 km depth (Dorfler et al., 2014). Therefore rocks exposed at the surface formed at ultrahigh temperatures in middle to lower crustal depths and probably reflect the deepest parts of the magma chamber.

Many studies on the structure of the Cortlandt and gravity and magnetic surveys conducted in the mid-to-late-20th century were used to produce cross sections of the series (Ratcliffe et al., 1982; Steenland and Woollard, 1952). A NW-SE trending cross section across pluton VI and Salt Hill (**Fig 4.2**) shows that the pluton is a lopolithic mass and that the emeries are located near the chamber floor (Ratcliffe et al., 1983). Therefore, the present-day erosional surface represents the deepest portions of the magma chamber where the emeries settled among fractionally crystallized olivine cumulates of the mantle-derived magma. Furthermore, we believe that additional residual material similar to the emery xenoliths may be located within unexposed parts of the pluton near the contact between the magma chamber and country rock (see **Fig. 4.2**).

4.5 Conclusions

A significant amount of work has been conducted on understanding magma hybridization and its connection with partially melted crust, but there is a significant lack of documentation ofn residual crustal material. The reason is because there is very little exposure of the crustal (Al-Fe-rich) residuum due to its high density. However, if crustal melting and assimilation are widespread in the lower crust, then the presence of the residuum would be expected to be common. Therefore, although the products and compositions used in this study are from a relatively small-scale example of pelite–mafic magma interaction, it has serious implications for processes ongoing at the lower crust–upper mantle boundary.

The UHT processes that occurred at the Cortlandt Complex may be analogous to the processes associated with magmatic underplating or crustal delamination into the mantle. Although exposure of emery is rare at the surface, it may be more common at depths of 30–40 km. Hybrid rocks like norite have been associated with mixing mafic (mantle-derived) magma by partial melting of pelitic rocks and therefore are possible indicators of UHT metamorphic processes. Furthermore, the link between hybrid igneous rocks and UHT refractory materials may be an economically important connection. PGM (platinum-group metals) mining is prominent in locations of well-documented exposure of hybrid igneous rocks and extensive crustal assimilation such as the Bushveld and Duluth Complexes.

4.6 References

Alasino, P. H., Casquet, C., Larrovere, M. A., Pankhurst, R. J., Galindo, C., Dahlquist, J. A., Baldo, E. G., and Rapela, C. W., 2014, The evolution of a mid-crustal thermal aureole at Cerro Toro, Sierra de Famatina, NW Argentina: Lithos, v. 190-191, p. 154-172.

Anderson, D. L., 1989, Theory of the Earth, Boston, Blackwell Publications, 366 p.:

Bowen, N. L., 1928, The evolution of the igneous rocks, Princeton, Princeton University Press.

Caricchi, L., Burlini, L., Ulmer, P., Gerya, T., Vassalli, M., and Papale, P., 2007, Non-Newtonian rheology of crystal-bearing magmas and implications for magma ascent dynamics: Earth and Planetary Science Letters, v. 264, p. 402-419.

Connolly, J. A. D., 2005, Computation of phase equilibria by linear programming: a tool for geodynamic modeling and its application to subduction zone decarbonation: Earth and Planetary Science Letters, v. 236, p. 524-541.

Diaz-Alvarado, J., Castro, A., Fernandez, C., and Ignacio Moreno-Ventas, I., 2011, Assessing bulk assimilation in cordierite-bearing granitoids from the Central System Batholith,

Spain; experimental, geochemical and geochronological constraints: Journal of Petrology, v. 52, no. 2, p. 223-256.

Dorfler, K. M., Tracy, R. J., and Caddick, M. J., 2014, Late-stage orogenic loading revealed by contact metamorphism in the northern Appalachians, New York: Journal of Metamorphic Geology, v. 32, p. 113-132.

Duchesne, J. C., Wilmart, E., Demaiffe, D., and Hertogen, J., 1989, Monzonorites from Rogaland (Southwest Norway): a series of rocks coevl but not comagmatic with massif-type anorthosites: Precambrian Research, v. 45, p. 111-128.

Johnson, T. E., Brown, M., and White, R. W., 2010, Petrogenetic modelling of strongly residual metapelitic xenoliths within the southern Platreef, Bushveld Complex, South Africa: Journal of Metamorphic Geology, v. 28, p. 269-291.

Lee, C.-T. A., and Bachmann, O., 2014, How important is the role of crystal fractionation in making intermediate magmas? Insights from Zr and P systematics: Earth and Planetary Science Letters, v. 393, p. 266-274.

Preston, R. J., Dempster, T. J., Bell, B. R., and Rogers, G., 1999, The petrology of mullite-bearing peraluminous xenoliths: Implications for contamination processes in basaltic magmas: Journal of Petrology, v. 40, no. 4, p. 549-573.

Ratcliffe, N. M., Armstrong, R. L., Mose, D. G., Seneschal, R., Williams, N., and Baiamonte, M. J., 1982, Emplacement history and tectonic significance of the Cortlandt Complex, related plutons, and dike swarms in the Taconide Zone of southeastern New York based on K-Ar and Rb-Sr investigations: American Journal of Science (1880), v. 282, no. 3, p. 358-390.

Ratcliffe, N. M., Bender, J. F., and Tracy, R. J., 1983, Tectonic setting, chemical petrology and petrogenesis of the Cortlandt Complex and realted rocks of southeastern New York State, Guidebook for field trip 1, Northeastern Section, Geological Society of America Meeting, Kiamesha Lake, New York, 101 p.:

Sparks, R. S. J., and Marshall, L. A., 1986, Thermal and mechanical constraints on mixing between mafic and silicic magmas: Journal of Volcanology and Geothermal Research, v. 29, no. 1-4, p. 99-124.

Steenland, N. C., and Woollard, G. P., 1952, Gravity and magnetic investigation of the structure of the Cortlandt Complex, New York: Geological Society of America Bulletin, v. 63, p. 1075-1104.

Theriault, R. D., Barnes, S.-J., and Severson, M. J., 1997, The influence of country-rock assimilation and silicate to sulfide ratios (*R* factor) on the genesis of the Dunka Road Cu–Ni–platinumn-group element deposit, Duluth Complex, Minnesota: Canadian Journal of Earth Sciences, v. 34, no. 375-389.

4.7 Figures

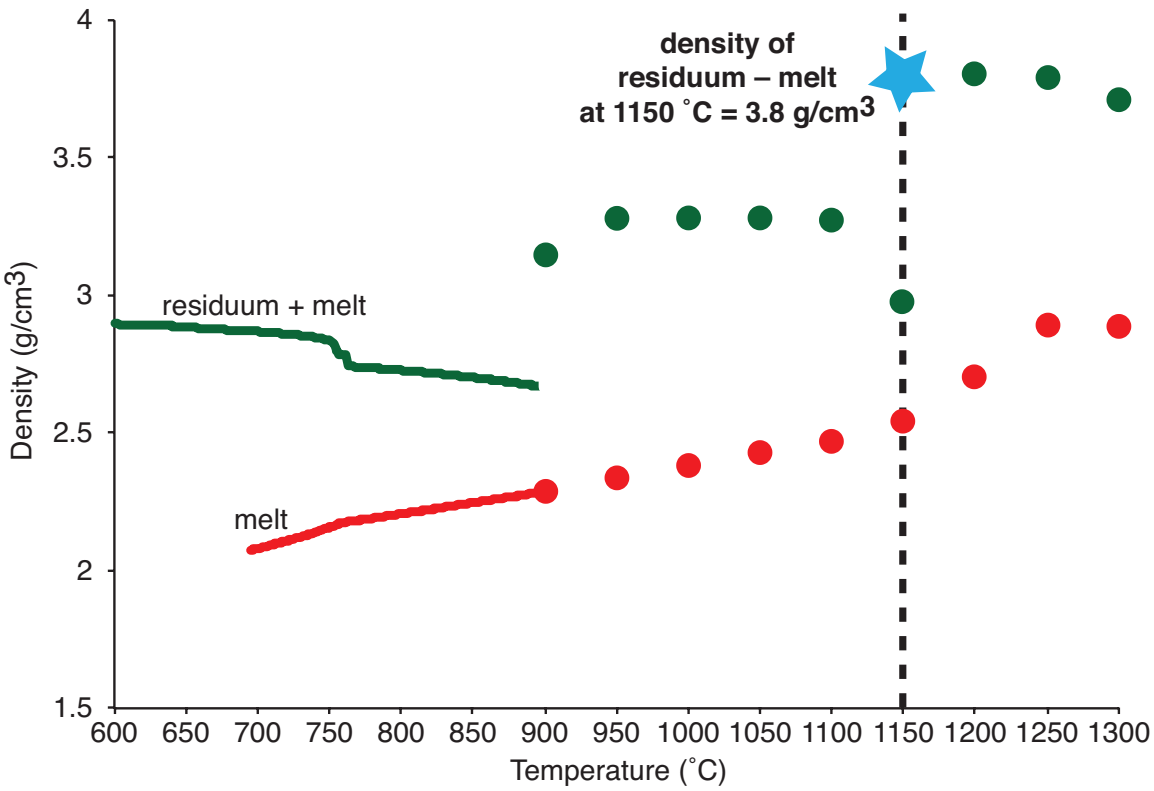

Figure 4.1. Change in density of the residuum and melt *vs.* temperature. Red line denotes only the density of the calculated melt; green line represents the entire system (residuum and melt). Dots from 900 – 1300 ˚C represent phase equilibria calculated every 50 ˚C, as described in chapter three. Blue star at 1150 ˚C, denotes the density of only the residuum composition, which was used in cooling and oxidation calculations that matched well with the residuum composition and phase proportions (see chapter three for details).

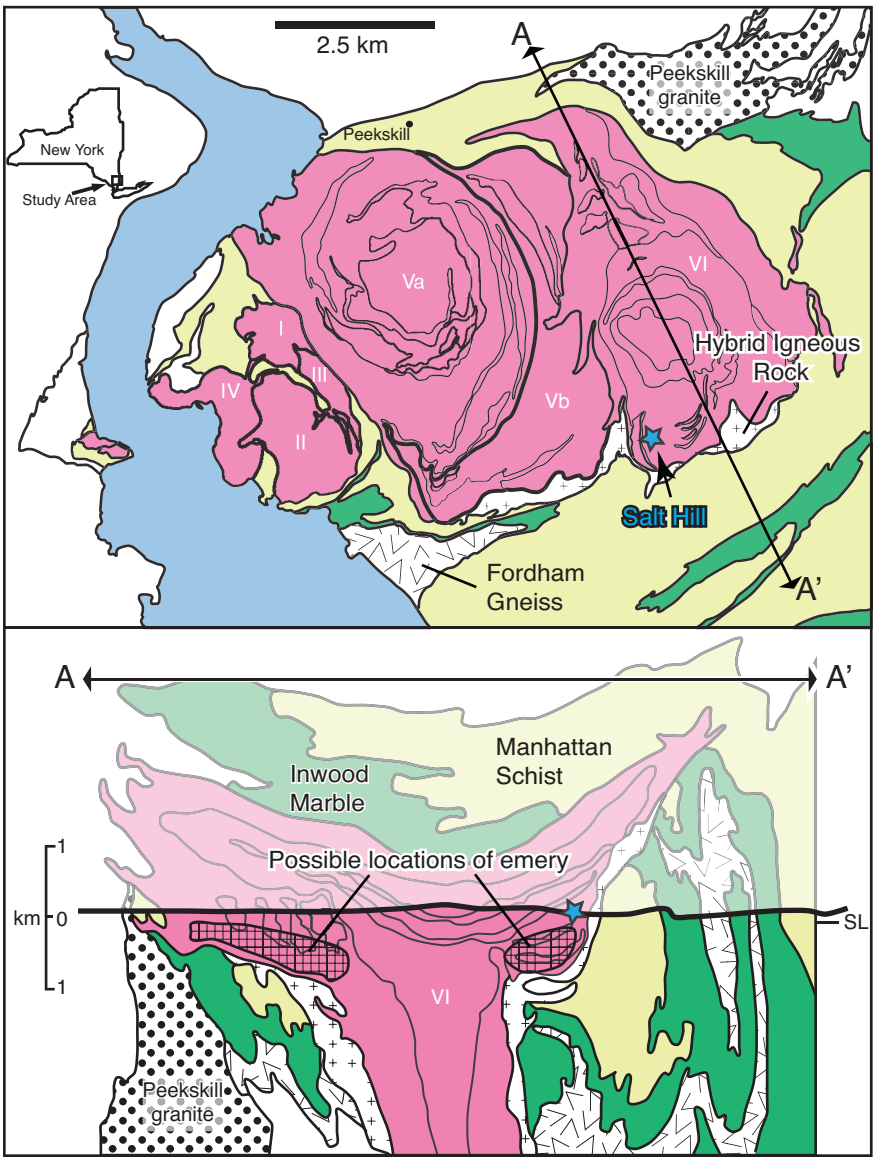

Figure 4.2. Simplified geologic maps of the Cortlandt Complex after (Ratcliffe et al., 1983). Top map is the areal view of the entire series with transect A-A' across the easternmost (youngest) pluton VI. Bottom map is a cross section based on gravity and magnetic surveys of the Cortlandt Complex. Due to placement of the dense Salt Hill xenoliths at the edge of the complex, we infer that ledges of country rock and fractionally crystallized magma prevented the xenoliths from descending to deeper parts of the pluton. Crosshatched areas indicate where we believe unexposed emery deposits may be located.

Appendix A.

Supplementary Information to Chapter 2

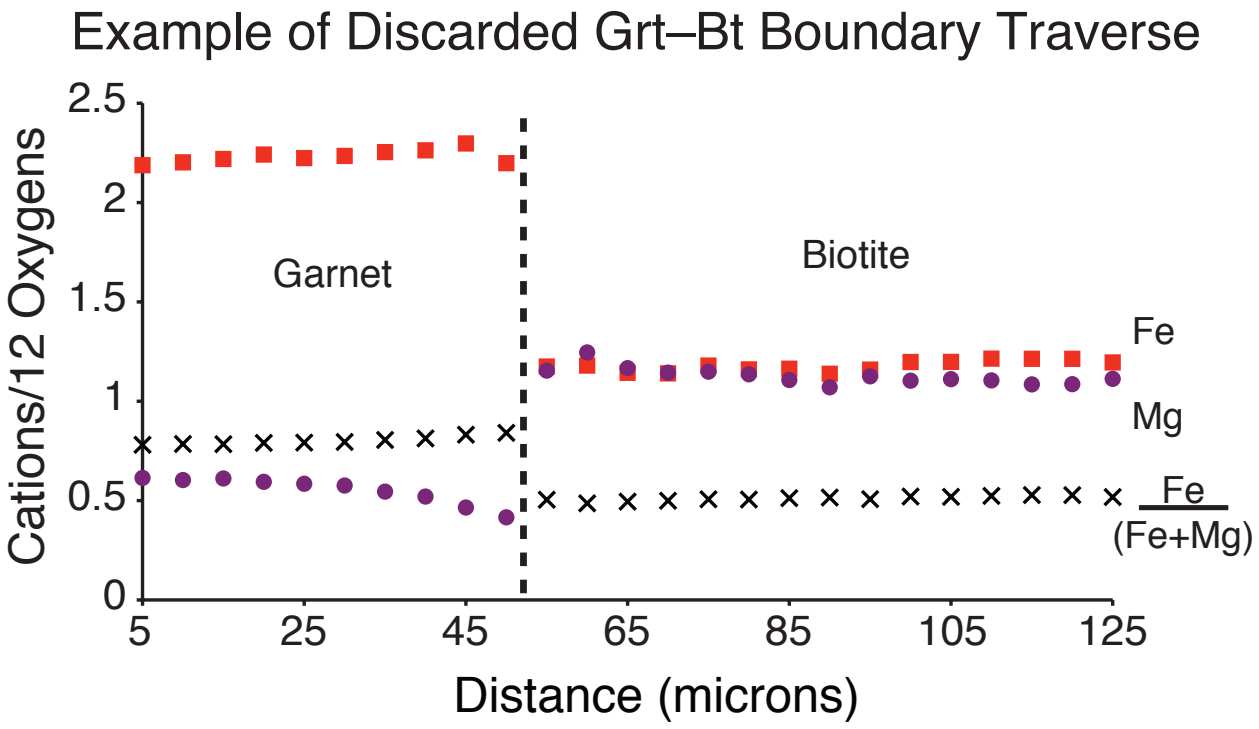

Figure A1. Example of a discarded traverse across a garnet–biotite boundary (discarded because of excessive modification of garnet composition).

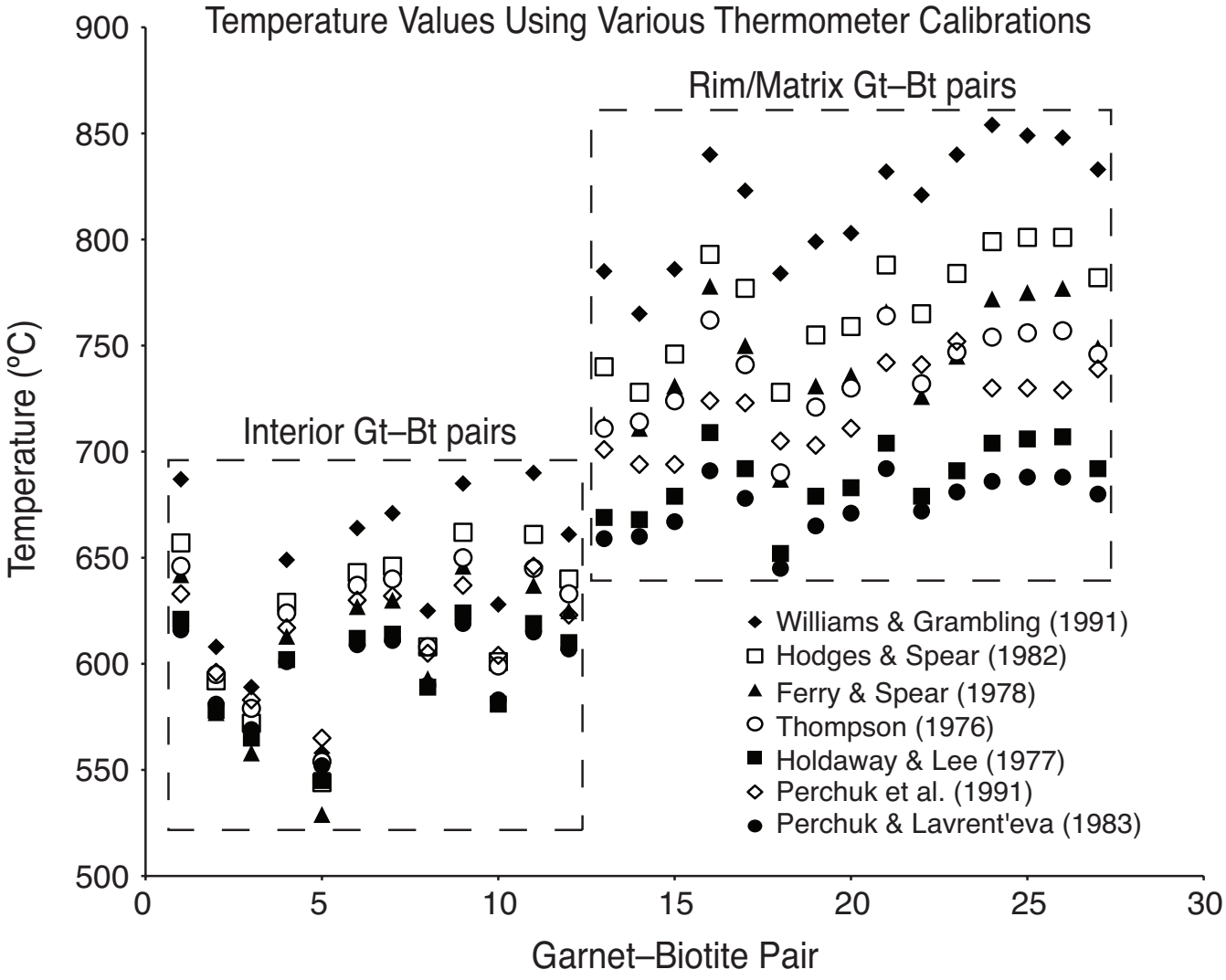

Figure A2. Direct comparison of various garnet–biotite thermometer calibrations for each analysis listed in Table A1.1. The Hodges & Spear (1982) calculation was used in this study.

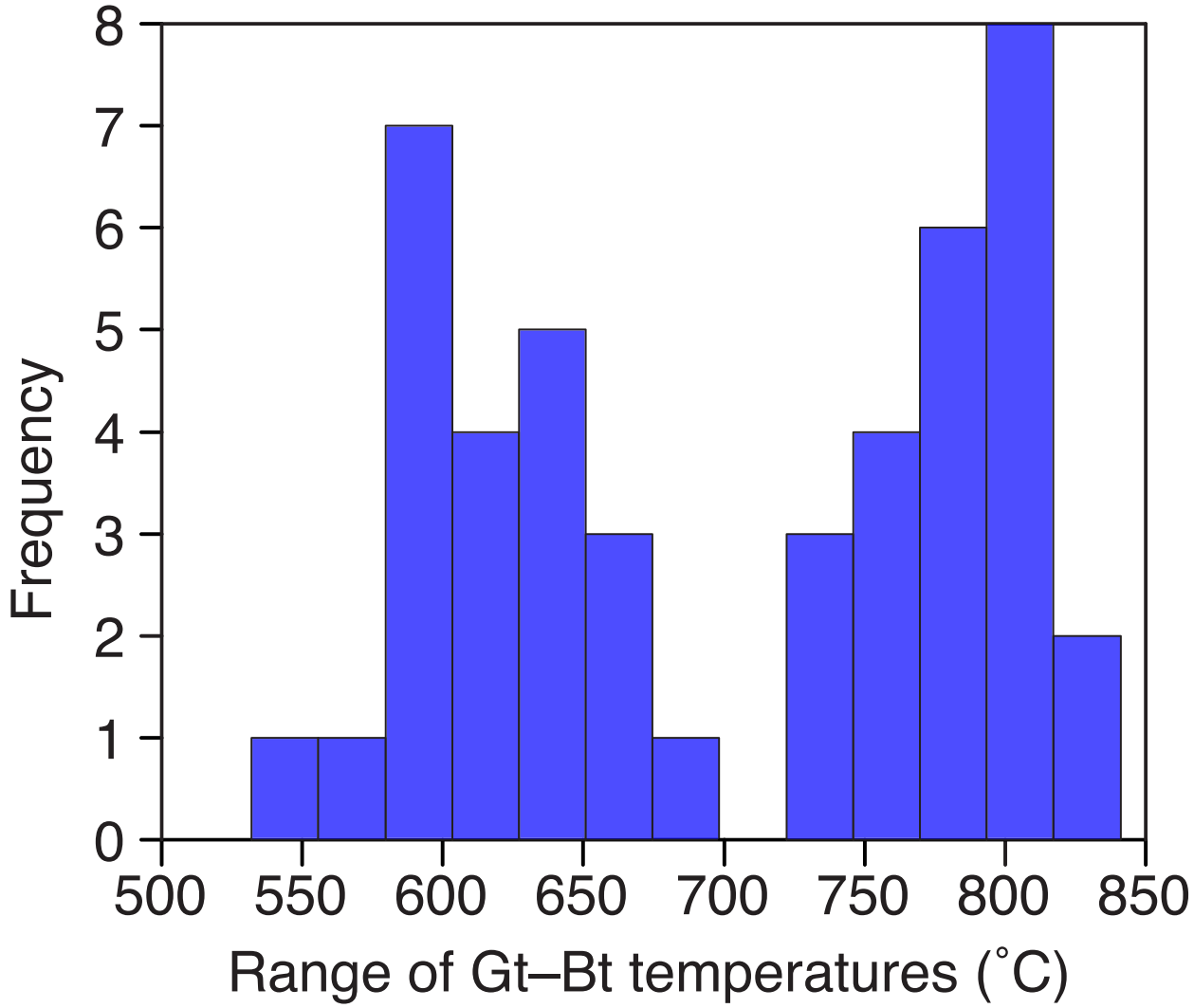

Figure A3. Temperature results from all individual garnet–biotite pairs examined in this study reveal a bimodal pattern, with peaks at ~600 and 800 ˚C.

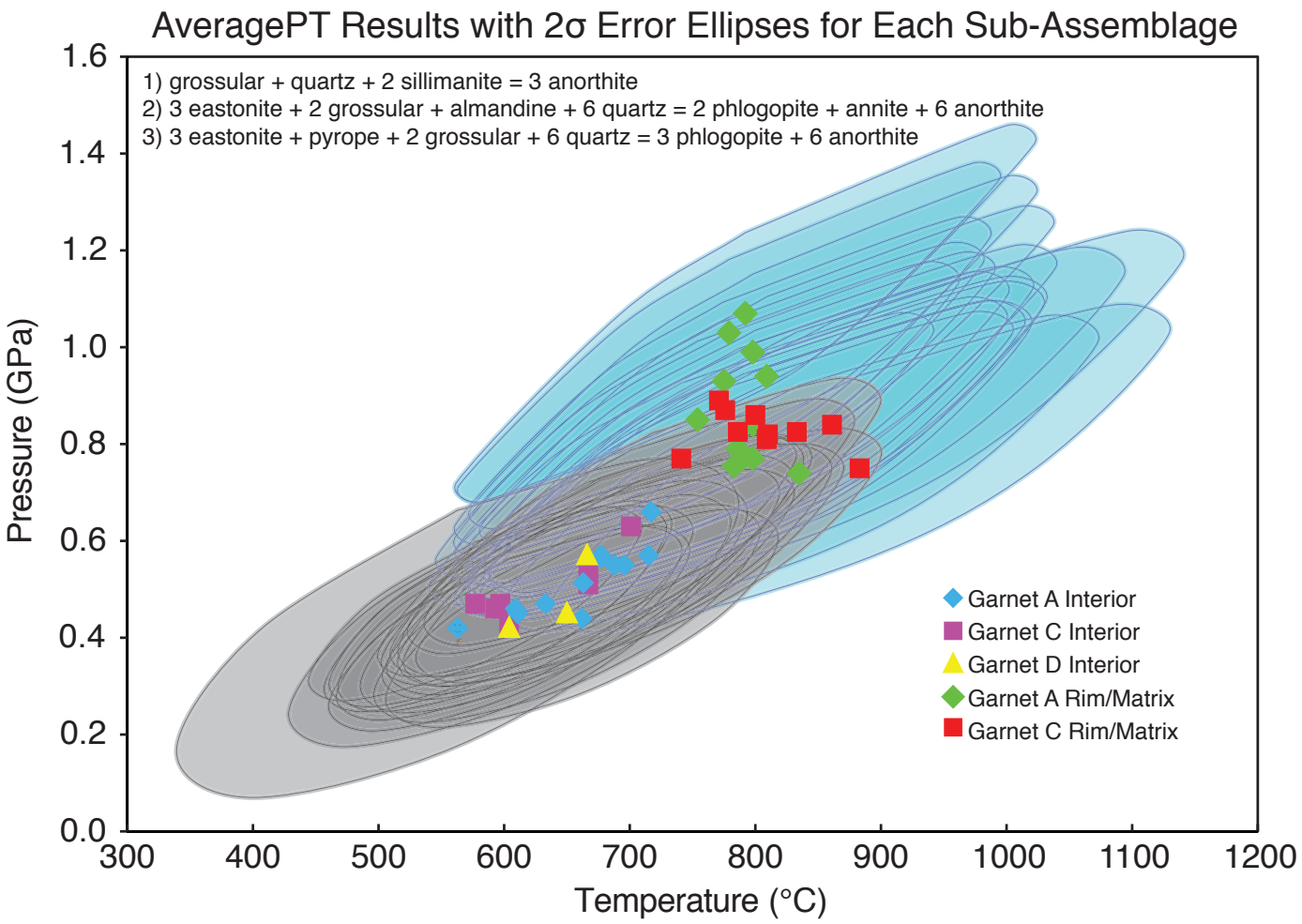

Figure A4. Average*PT* results for each sub-assemblage showing a 2σ error ellipse for each best fit *P–T*.

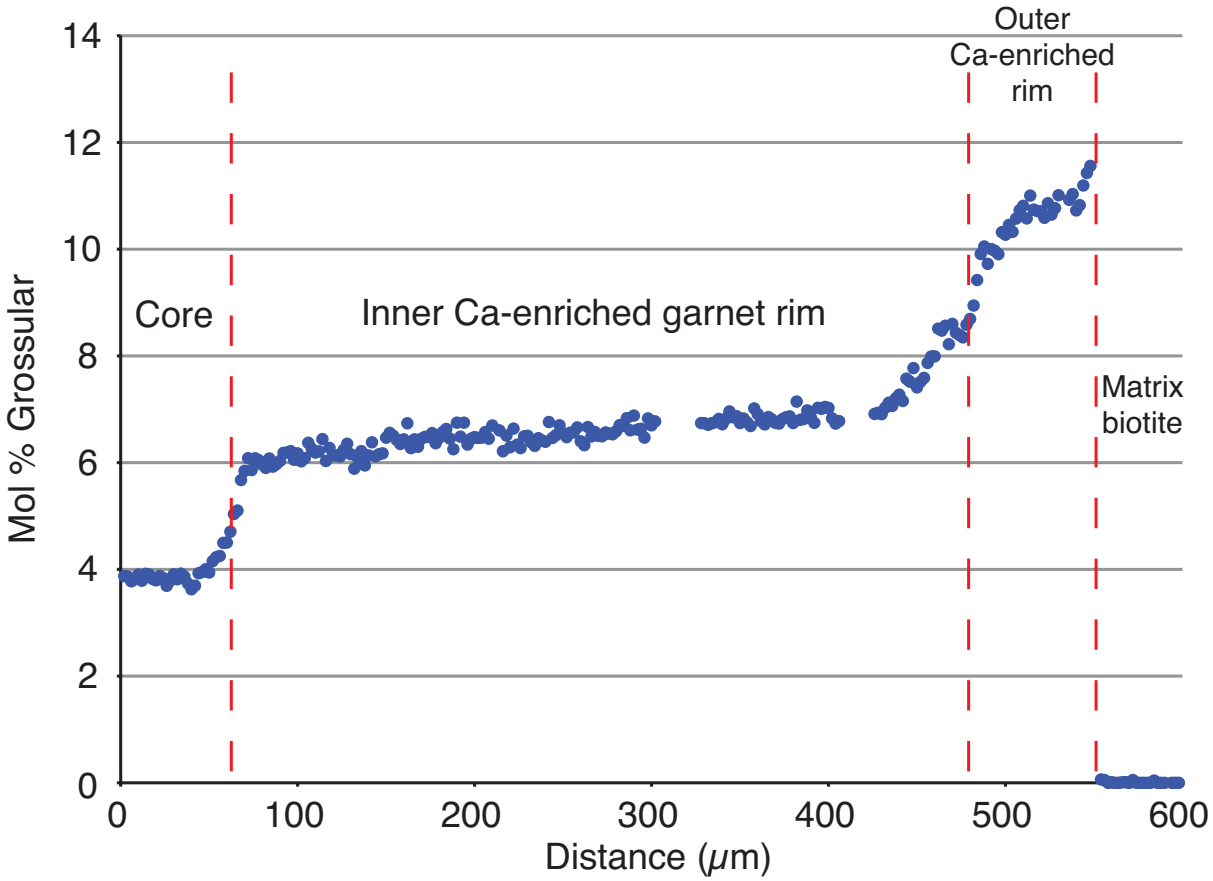

Figure A5. Detailed microprobe traverse (only Ca shown) through the outer core and rims of garnet crystal shown in Figure 2.4. Note that inner rim has a sharp boundary with crystal core buy is effectively unzoned until its outermost contact with the outer rim (which contains the highest grossular content found in this study).

Table A1. Non-averaged compositions of each garnet, bioite and plagioclase analysis used for thermobarometric calculations and the Average*PT* results.

Garnet A Garnet-Biotite-Plagioclase Pairs Compositions — Rim/Matrix pairs

Biotite	2	14	15	"22"	23	26	27	28	32	34	35	35	23
SiO2	36.12	36.19	36.00	35.83	36.24	36.03	36.09	36.64	36.46	36.26	35.98	35.98	36.24
TiO2	3.82	3.15	2.55	3.68	3.54	3.62	3.73	3.38	3.23	2.95	3.13	3.13	3.54
Al2O3	18.31	18.74	18.77	18.14	18.09	18.28	17.84	18.44	18.15	18.55	18.69	18.69	18.09
FeO*	18.81	18.84	20.09	18.75	18.78	18.85	19.08	18.56	19.33	18.90	19.99	19.99	18.78
MnO	0.03	0.03	0.01	0.02	0.03	0.05	0.04	0.03	0.04	0.02	0.03	0.03	0.03
MgO	10.09	9.39	8.72	9.69	9.62	9.86	10.09	10.08	9.99	9.93	8.92	8.92	9.62
CaO	0.00	0.00	0.00	0.00	0.00	0.01	0.00	0.00	0.01	0.01	0.03	0.03	0.00
Na2O	0.13	0.13	0.16	0.08	0.10	0.15	0.11	0.11	0.08	0.08	0.18	0.18	0.10
K2O	8.84	9.48	9.38	8.46	9.64	9.33	9.38	9.55	9.46	9.53	9.10	9.10	9.64
TOTAL	96.15	95.95	95.69	94.67	96.03	96.17	96.36	96.79	96.76	96.23	96.05	96.05	96.03
Formulas on the basis of 11 oxygens													
Si	2.704	2.723	2.732	2.720	2.728	2.707	2.711	2.728	2.727	2.722	2.715	2.715	2.728
Al	1.296	1.277	1.268	1.280	1.272	1.293	1.289	1.272	1.273	1.278	1.285	1.285	1.272
	4.000	4.000	4.000	4.000	4.000	4.000	4.000	4.000	4.000	4.000	4.000	4.000	4.000
Al	0.320	0.385	0.410	0.343	0.334	0.326	0.290	0.346	0.326	0.363	0.378	0.378	0.334
Ti	0.215	0.178	0.145	0.210	0.201	0.204	0.211	0.189	0.182	0.166	0.178	0.178	0.201
Fe2+	1.178	1.185	1.275	1.190	1.182	1.184	1.198	1.155	1.209	1.187	1.262	1.262	1.182
Mn	0.002	0.002	0.001	0.001	0.002	0.003	0.003	0.002	0.003	0.001	0.002	0.002	0.002
Mg	1.127	1.054	0.986	1.097	1.079	1.104	1.130	1.119	1.114	1.111	1.003	1.003	1.079
Oct Total	2.841	2.804	2.818	2.842	2.798	2.821	2.832	2.812	2.833	2.828	2.822	2.822	2.798
Ca	0.000	0.000	0.000	0.000	0.000	0.000	0.000	0.000	0.001	0.001	0.003	0.003	0.000
Na	0.018	0.019	0.024	0.012	0.014	0.021	0.015	0.016	0.012	0.012	0.026	0.026	0.014
K	0.844	0.910	0.908	0.819	0.926	0.895	0.899	0.907	0.903	0.912	0.876	0.876	0.926
A total	0.863	0.928	0.932	0.831	0.940	0.916	0.914	0.923	0.916	0.925	0.905	0.905	0.940
F	0.000	0.000	0.000	0.000	0.000	0.000	0.000	0.000	0.000	0.000	0.000	0.000	0.000
Cl	0.000	0.000	0.000	0.000	0.000	0.000	0.000	0.000	0.000	0.000	0.000	0.000	0.000
Fe/Fe+Mg	0.511	0.529	0.564	0.520	0.523	0.517	0.515	0.508	0.520	0.516	0.557	0.557	0.523

Garnet A Garnet-Biotite-Plagioclase Pairs Compositions — Interior Pairs

Biotite	4	6	7	8	9	10	11	13	25	29	30	36
SiO2	36.23	37.03	37.18	36.68	37.18	36.52	36.54	36.99	36.85	36.37	36.26	36.48
TiO2	3.97	3.90	2.79	2.43	2.15	2.77	3.88	2.64	3.73	3.21	3.91	2.58
Al2O3	18.29	17.72	19.94	19.24	19.13	18.68	18.44	18.95	18.59	18.57	18.36	18.60
FeO*	17.17	14.06	13.08	15.27	12.84	15.14	15.66	14.53	16.15	16.25	16.21	16.08
MnO	0.03	0.02	0.01	0.04	0.05	0.04	0.03	0.06	0.03	0.03	0.03	0.08
MgO	11.17	13.84	13.50	13.12	15.35	12.79	11.93	13.44	11.88	12.20	12.16	12.90
CaO	0.00	0.00	0.00	0.00	0.00	0.00	0.00	0.00	0.01	0.00	0.04	0.00
Na2O	0.24	0.33	0.23	0.29	0.37	0.16	0.29	0.31	0.17	0.20	0.22	0.28
K2O	8.65	8.34	9.15	9.00	8.97	9.53	9.22	9.01	9.50	9.49	8.93	8.98
TOTAL	95.75	95.24	95.90	96.07	96.05	95.62	96.00	95.94	96.91	96.31	96.11	95.98
Si	2.701	2.729	2.709	2.700	2.705	2.710	2.705	2.717	2.708	2.696	2.686	2.703
Al	1.299	1.271	1.291	1.300	1.295	1.290	1.295	1.283	1.292	1.304	1.314	1.297
	4.000	4.000	4.000	4.000	4.000	4.000	4.000	4.000	4.000	4.000	4.000	4.000
Al	0.308	0.267	0.422	0.369	0.346	0.344	0.314	0.358	0.319	0.317	0.288	0.327
Ti	0.222	0.216	0.153	0.135	0.118	0.155	0.216	0.146	0.206	0.179	0.218	0.144
Fe2+	1.071	0.866	0.797	0.940	0.782	0.939	0.969	0.893	0.993	1.007	1.004	0.996
Mn	0.002	0.001	0.001	0.002	0.003	0.003	0.002	0.004	0.002	0.002	0.002	0.005
Mg	1.241	1.520	1.467	1.441	1.666	1.415	1.317	1.472	1.302	1.348	1.343	1.425
Oct Total	2.844	2.870	2.840	2.887	2.914	2.856	2.818	2.872	2.822	2.852	2.854	2.897
Ca	0.000	0.000	0.000	0.000	0.000	0.000	0.000	0.000	0.001	0.000	0.003	0.000
Na	0.035	0.047	0.033	0.041	0.052	0.023	0.042	0.044	0.024	0.029	0.032	0.040
K	0.823	0.784	0.851	0.845	0.833	0.902	0.871	0.844	0.891	0.897	0.844	0.849
A total	0.858	0.832	0.884	0.887	0.885	0.925	0.913	0.888	0.916	0.926	0.879	0.889
F	0.000	0.000	0.000	0.000	0.000	0.000	0.000	0.000	0.000	0.000	0.000	0.000
Cl	0.000	0.000	0.000	0.000	0.000	0.000	0.000	0.000	0.000	0.000	0.000	0.000
Fe/Fe+Mg	0.463	0.363	0.352	0.395	0.319	0.399	0.424	0.377	0.433	0.428	0.428	0.412

Garnet C Garnet-Biotite-Plagioclase Pairs Compositions — Rim/Matrix pairs

Biotite	1	2	3	11	12	14	16A	16B	20	23
SiO2	35.92	36.00	35.75	35.93	36.20	36.10	36.10	35.74	35.93	35.72
TiO2	3.24	3.63	3.49	3.22	3.14	3.59	2.88	3.32	3.26	3.33
Al2O3	18.43	17.93	18.03	18.34	18.43	18.24	19.56	18.25	17.97	18.07
FeO*	19.12	19.08	19.48	20.86	19.28	18.69	18.09	19.20	19.52	19.04
MnO	0.03	0.03	0.04	0.06	0.04	0.03	0.00	0.00	0.03	0.02
MgO	9.75	10.09	9.88	9.24	10.00	10.23	10.01	10.04	9.80	9.91
CaO	0.00	0.01	0.00	0.02	0.00	0.00	0.02	0.00	0.01	0.01
Na2O	0.10	0.11	0.10	0.22	0.11	0.14	0.09	0.12	0.09	0.13
K2O	9.65	9.52	9.69	9.06	9.56	9.58	9.63	9.75	9.60	9.68
TOTAL	96.24	96.39	96.46	96.95	96.76	96.59	96.38	96.42	96.19	95.90
Si	2.705	2.706	2.694	2.700	2.710	2.701	2.694	2.691	2.713	2.702
Al	1.295	1.294	1.306	1.300	1.290	1.299	1.306	1.309	1.287	1.298
	4.000	4.000	4.000	4.000	4.000	4.000	4.000	4.000	4.000	4.000
Al	0.340	0.294	0.296	0.324	0.335	0.310	0.414	0.311	0.312	0.313
Ti	0.183	0.205	0.198	0.182	0.177	0.202	0.161	0.188	0.185	0.190
Fe2+	1.204	1.199	1.228	1.310	1.206	1.169	1.129	1.209	1.232	1.204
Mn	0.002	0.002	0.002	0.004	0.002	0.002	0.000	0.000	0.002	0.001
Mg	1.095	1.130	1.110	1.035	1.116	1.141	1.114	1.127	1.103	1.117
Oct Total	2.823	2.830	2.833	2.855	2.837	2.825	2.818	2.834	2.834	2.826
Ca	0.000	0.000	0.000	0.002	0.000	0.000	0.002	0.000	0.000	0.001
Na	0.015	0.016	0.015	0.031	0.016	0.020	0.014	0.017	0.013	0.018
K	0.927	0.913	0.932	0.868	0.913	0.914	0.916	0.937	0.924	0.934
A total	0.942	0.929	0.947	0.902	0.929	0.935	0.932	0.953	0.938	0.953
F	0.000	0.000	0.000	0.000	0.000	0.000	0.000	0.000	0.000	0.000
Cl	0.000	0.000	0.000	0.000	0.000	0.000	0.000	0.000	0.000	0.000
Fe/Fe+Mg	0.524	0.515	0.525	0.559	0.519	0.506	0.503	0.518	0.528	0.519

Garnet C Garnet-Biotite-Plagioclase Pairs Compositions — Interior Pairs; Garnet D — Interior Pairs

Biotite	4	5	7	7	5	7	7	Garnet D 3	Garnet D 5	Garnet D 7
SiO2	35.95	36.50	37.08	37.08	36.50	37.08	37.08	36.54	36.92	35.74
TiO2	3.75	3.71	2.39	2.39	3.71	2.39	2.39	3.03	3.07	3.91
Al2O3	18.10	18.28	19.34	19.34	18.28	19.34	19.34	18.74	18.92	18.23
FeO*	16.94	15.98	13.49	13.49	15.98	13.49	13.49	15.15	15.25	15.71
MnO	0.03	0.05	0.03	0.03	0.05	0.03	0.03	0.02	0.04	0.04
MgO	11.48	12.44	13.06	13.06	12.44	13.06	13.06	12.90	12.76	12.06
CaO	0.00	0.00	0.05	0.05	0.00	0.05	0.05	0.00	0.00	0.02
Na2O	0.20	0.27	0.04	0.04	0.27	0.04	0.04	0.32	0.25	0.24
K2O	9.41	9.42	10.05	10.05	9.42	10.05	10.05	9.00	9.29	9.08
TOTAL	95.85	96.64	95.54	95.54	96.64	95.54	95.54	95.86	96.68	95.04
Si	2.689	2.693	2.733	2.733	2.693	2.733	2.733	2.709	2.718	2.686
Al	1.311	1.307	1.267	1.267	1.307	1.267	1.267	1.291	1.282	1.314
	4.000	4.000	4.000	4.000	4.000	4.000	4.000	4.000	4.000	4.000
Al	0.285	0.282	0.413	0.413	0.282	0.413	0.413	0.346	0.360	0.301
Ti	0.211	0.206	0.133	0.133	0.206	0.133	0.133	0.169	0.170	0.221
Fe2+	1.060	0.986	0.831	0.831	0.986	0.831	0.831	0.939	0.939	0.988
Mn	0.002	0.003	0.002	0.002	0.003	0.002	0.002	0.001	0.003	0.002
Mg	1.280	1.368	1.435	1.435	1.368	1.435	1.435	1.426	1.400	1.352
Oct Total	2.838	2.844	2.814	2.814	2.844	2.814	2.814	2.882	2.872	2.864
Ca	0.000	0.000	0.004	0.004	0.000	0.004	0.004	0.000	0.000	0.001
Na	0.029	0.039	0.006	0.006	0.039	0.006	0.006	0.047	0.036	0.036
K	0.898	0.887	0.945	0.945	0.887	0.945	0.945	0.851	0.872	0.871
A total	0.927	0.926	0.955	0.955	0.926	0.955	0.955	0.898	0.908	0.908
F	0.000	0.000	0.000	0.000	0.000	0.000	0.000	0.113	0.148	0.140
Cl	0.000	0.000	0.000	0.000	0.000	0.000	0.000	0.000	0.000	0.000
Fe/Fe+Mg	0.453	0.419	0.367	0.367	0.419	0.367	0.367	0.397	0.401	0.422

Garnet A Garnet-Biotite-Plagioclase Pairs Compositions — Rim/Matrix pairs

Plagioclase	31	Matrix	16	16	17	20	16	31	31	34	35	21	24
SiO2	60.52	58.78	59.46	59.46	58.57	60.35	59.46	60.52	60.52	59.60	57.74	60.01	59.43
Al2O3	26.27	26.74	26.43	26.43	26.85	25.80	26.43	26.27	26.27	26.11	27.66	25.83	26.54
FeO*	0.38	0.00	0.12	0.12	1.12	0.49	0.12	0.38	0.38	0.20	0.33	0.46	0.36
CaO	7.27	8.58	7.91	7.91	7.78	7.60	7.91	7.27	7.27	8.16	9.71	7.84	8.41
Na2O	7.27	6.63	6.83	6.83	6.41	7.19	6.83	7.27	7.27	6.85	6.00	7.08	6.73
K2O	0.10	0.14	0.18	0.18	0.15	0.10	0.18	0.10	0.10	0.14	0.09	0.10	0.10
TOTAL	101.82	100.51	100.93	100.93	100.88	101.52	100.93	101.82	101.82	101.05	101.53	101.32	101.58
Formulas on the basis of 8 oxygens													
Si	2.650	2.601	2.629	2.629	2.600	2.654	2.629	2.650	2.650	2.634	2.553	2.647	2.617
Al	1.356	5.399	1.377	1.377	1.405	1.337	1.377	1.356	1.356	1.360	1.441	1.342	1.377
Fe2+	0.014	0.000	0.005	0.005	0.042	0.018	0.005	0.014	0.014	0.007	0.012	0.017	0.013
Mg	0.000	0.000	0.000	0.000	0.000	0.000	0.000	0.000	0.000	0.000	0.000	0.000	0.000
Ca	0.341	0.413	0.374	0.374	0.370	0.358	0.374	0.341	0.341	0.386	0.460	0.370	0.397
Na	0.617	0.563	0.586	0.586	0.551	0.613	0.586	0.617	0.617	0.587	0.514	0.605	0.575
K	0.006	0.008	0.010	0.010	0.009	0.006	0.010	0.006	0.006	0.008	0.005	0.006	0.006
% Or	0.58	0.76	1.03	1.03	0.92	0.56	1.03	0.58	0.58	0.79	0.53	0.58	0.57
% Ab	64.03	57.24	60.37	60.37	59.31	62.77	60.37	64.03	64.03	59.82	52.52	61.68	58.83
%An	35.40	41.99	38.60	38.60	39.78	36.67	38.60	35.40	35.40	39.39	46.95	37.75	40.60
An/(An+Ab)	35.60	42.32	39.00	39.00	40.14	36.88	39.00	35.60	35.60	39.70	47.20	37.96	40.83

Garnet A Garnet-Biotite-Plagioclase Pairs Compositions — Interior Pairs

Plagioclase	33	3	3	5	12	12	18	3	33	3	19	37
SiO2	60.75	60.94	60.94	61.65	61.20	61.20	61.26	60.94	60.75	60.94	60.97	59.35
Al2O3	25.41	25.07	25.07	24.54	24.91	24.91	25.33	25.07	25.41	25.07	25.19	25.78
FeO*	0.77	0.00	0.00	0.00	0.28	0.28	0.30	0.00	0.77	0.00	0.51	0.91
CaO	7.10	7.00	7.00	6.51	6.74	6.74	6.98	7.00	7.10	7.00	7.07	7.92
Na2O	7.19	7.26	7.26	7.52	7.54	7.54	6.46	7.26	7.19	7.26	7.27	6.80
K2O	0.43	0.44	0.44	0.31	0.23	0.23	0.50	0.44	0.43	0.44	0.40	0.32
TOTAL	101.65	100.72	100.72	100.53	100.90	100.90	100.83	100.72	101.65	100.72	101.41	101.08
Si	2.672	2.693	2.693	2.723	2.700	2.700	2.699	2.693	2.672	2.693	2.683	2.633
Al	1.317	1.306	1.306	1.277	1.295	1.295	1.315	1.306	1.317	1.306	1.307	1.348
Fe2+	0.028	0.000	0.000	0.000	0.010	0.010	0.011	0.000	0.028	0.000	0.019	0.034
Mg	0.000	0.000	0.000	0.000	0.000	0.000	0.000	0.000	0.000	0.000	0.000	0.000
Ca	0.335	0.331	0.331	0.308	0.319	0.319	0.329	0.331	0.335	0.331	0.333	0.376
Na	0.613	0.622	0.622	0.644	0.645	0.645	0.552	0.622	0.613	0.622	0.621	0.585
K	0.024	0.025	0.025	0.018	0.013	0.013	0.028	0.025	0.024	0.025	0.022	0.018
% Or	2.48	2.55	2.55	1.82	1.34	1.34	3.09	2.55	2.48	2.55	2.29	1.85
% Ab	63.10	63.58	63.58	66.42	66.03	66.03	60.70	63.58	63.10	63.58	63.58	59.74
%An	34.42	33.87	33.87	31.76	32.62	32.62	36.21	33.87	34.42	33.87	34.13	38.41
An/(An+Ab)	35.30	34.76	34.76	32.35	33.07	33.07	37.36	34.76	35.30	34.76	34.93	39.13

Garnet C Garnet-Biotite-Plagioclase Pairs Compositions — Rim/Matrix pairs

Plagioclase	22*	1	19*	19*	19*	18	22*	19*	22*	22*
SiO2	57.51	59.86	59.85	59.85	59.85	58.33	57.51	59.85	57.51	57.51
Al2O3	26.84	25.70	25.80	25.80	25.80	26.51	26.84	25.80	26.84	26.84
FeO*	1.05	0.15	0.26	0.26	0.26	0.37	1.05	0.26	1.05	1.05
CaO	8.61	7.81	7.66	7.66	7.66	8.51	8.61	7.66	8.61	8.61
Na2O	6.11	6.91	7.10	7.10	7.10	6.37	6.11	7.10	6.11	6.11
K2O	0.24	0.17	0.13	0.13	0.13	0.20	0.24	0.13	0.24	0.24
TOTAL	100.37	100.75	100.81	100.81	100.81	100.28	100.37	100.81	100.37	100.37
Si	2.575	2.632	2.650	2.650	2.650	2.603	2.575	2.650	2.575	2.575
Al	1.417	5.368	1.346	1.346	1.346	1.394	1.417	1.346	1.417	1.417
Fe2+	0.039	0.000	0.010	0.010	0.010	0.014	0.039	0.010	0.039	0.039
Mg	0.000	0.000	0.000	0.000	0.000	0.000	0.000	0.000	0.000	0.000
Ca	0.413	0.382	0.364	0.364	0.364	0.407	0.413	0.364	0.413	0.413
Na	0.531	0.593	0.609	0.609	0.609	0.551	0.531	0.609	0.531	0.531
K	0.014	0.006	0.008	0.008	0.008	0.012	0.014	0.008	0.014	0.014
% Or	1.46	0.63	0.77	0.77	0.77	1.19	1.46	0.77	1.46	1.46
% Ab	55.41	60.43	62.14	62.14	62.14	56.87	55.41	62.14	55.41	55.41
%An	43.14	38.94	37.08	37.08	37.08	41.95	43.14	37.08	43.14	43.14
An/(An+Ab)	43.77	39.19	37.37	37.37	37.37	42.45	43.77	37.37	43.77	43.77

Garnet C Garnet-Biotite-Plagioclase Pairs Compositions — Interior Pairs; Garnet D — Interior Pairs

Plagioclase	21*	6	8	9	10	13	17	Garnet D 4	Garnet D 6	Garnet D 14
SiO2	60.26	60.25	58.35	59.24	59.36	57.50	59.49	61.11	61.08	60.36
Al2O3	25.66	25.58	26.48	26.39	26.41	27.23	26.25	26.77	26.46	27.09
FeO*	0.50	0.40	0.61	0.25	0.23	0.27	0.30	0.41	0.54	0.45
CaO	7.42	7.29	8.68	8.23	8.27	9.38	8.05	8.10	7.93	8.48
Na2O	6.98	7.17	6.28	6.78	6.58	6.05	6.78	7.23	7.34	7.09
K2O	0.40	0.23	0.19	0.18	0.20	0.09	0.21	0.16	0.19	0.14
TOTAL	101.22	100.92	100.59	101.07	101.05	100.52	101.08	103.773	103.537	103.610
Si	2.659	2.664	2.600	2.620	2.624	2.565	2.630	2.633	2.640	2.610
Al	1.335	1.333	1.390	1.376	1.376	1.431	1.367	5.367	5.360	5.390
Fe2+	0.019	0.015	0.023	0.009	0.008	0.010	0.011	0.015	0.019	0.016
Mg	0.000	0.000	0.000	0.000	0.000	0.000	0.000	0.000	0.000	0.000
Ca	0.351	0.345	0.415	0.390	0.392	0.448	0.381	0.374	0.367	0.393
Na	0.597	0.615	0.542	0.582	0.564	0.523	0.581	0.604	0.615	0.594
K	0.022	0.013	0.011	0.010	0.012	0.005	0.012	0.009	0.010	0.008
% Or	2.31	1.36	1.13	1.05	1.19	0.54	1.23	0.891	1.050	0.785
% Ab	61.55	63.17	56.04	59.22	58.33	53.57	59.65	61.217	61.958	59.728
%An	36.14	35.48	42.83	39.73	40.48	45.89	39.12	37.892	36.993	39.487
An/(An+Ab)	36.99	35.97	43.32	40.15	40.97	46.14	39.61	38.232	37.385	39.795

Table A1 continued. Non-averaged compositions of each garnet, bioite and plagioclase analysis used for thermobarometric calculations and the Average*PT* results.

Garnet A Garnet-Biotite-Plagioclase Pairs Compositions

Rim/Matrix pairs

Garnet	2 & 31	14 & Matrix	15 & 16	22 & 16	23 & 17	26 & 20	27 & 16	28 & 31	32 & 31	34	35	35 & 21	23 & 24
SiO_2	38.94	38.56	38.79	38.66	39.09	38.94	38.81	39.27	39.30	39.31	38.71	38.67	39.13
TiO_2	0.03	0.03	0.03	0.02	0.03	0.02	0.02	0.03	0.01	0.02	0.01	0.01	0.03
Al_2O_3	21.98	21.65	21.65	21.74	21.94	21.88	21.68	22.12	21.99	21.90	21.87	21.84	21.92
FeO	34.07	34.89	34.00	33.89	32.84	33.29	33.91	33.62	33.35	33.12	34.12	34.24	32.96
MnO	1.09	1.34	1.24	1.20	1.08	1.34	1.22	1.16	1.03	1.04	1.21	1.26	1.16
MgO	4.52	4.41	4.62	4.92	4.25	4.80	4.87	4.71	4.38	4.41	4.19	4.26	4.49
CaO	2.40	1.27	1.66	2.18	3.25	1.81	2.04	2.64	3.42	3.55	2.37	1.92	2.86
Na_2O													
K_2O													
Total	103.03	102.14	101.99	102.59	102.49	102.08	102.52	103.55	103.49	103.34	102.48	102.20	102.54
Formulas on the basis of 12 oxygens													
Si	3.00	3.02	3.02	3.00	3.02	3.02	3.01	3.01	3.01	3.018	3.008	3.01	3.02
Ti	0.00	0.00	0.00	0.00	0.00	0.00	0.00	0.00	0.00	0.001	0.001	0.00	0.00
Al	2.00	1.98	1.99	1.99	2.00	2.00	1.98	2.00	1.99	1.981	2.002	2.00	2.00
	2.00	1.98	1.99	1.99	2.00	2.00	1.98	2.00	1.99	1.982	2.003	2.01	2.00
Fe	2.20	2.17	2.22	2.20	2.12	2.16	2.20	2.15	2.14	2.126	2.217	2.23	2.13
Mn	0.07	0.09	0.08	0.08	0.07	0.09	0.08	0.08	0.07	0.068	0.080	0.08	0.08
Mg	0.52	0.61	0.54	0.57	0.49	0.55	0.56	0.54	0.50	0.505	0.485	0.50	0.52
Ca	0.20	0.12	0.14	0.18	0.27	0.15	0.17	0.22	0.28	0.292	0.197	0.16	0.24
	2.99	2.99	2.97	3.02	2.95	2.95	3.01	2.98	2.99	2.991	2.979	2.97	2.96
Mol% Alm	73.59	72.61	74.59	72.64	71.90	73.14	73.05	72.19	71.60	71.1	74.4	75.12	71.96
Mol% Pyr	17.39	20.33	18.02	18.78	16.59	18.79	18.68	18.03	16.75	16.9	16.3	16.68	17.51
Mol% Sps	2.39	3.02	2.75	2.60	2.40	2.98	2.65	2.52	2.23	2.3	2.7	2.80	2.56
Mol% Gro	6.62	4.03	4.64	5.98	9.11	5.09	5.62	7.26	9.42	9.8	6.6	5.40	7.98
Fe/(Fe+Mg)	0.81	0.78	0.81	0.79	0.81	0.80	0.80	0.80	0.81	0.808	0.821	0.82	0.80
Mg/(Mg+Fe)	0.19	0.22	0.19	0.21	0.19	0.20	0.20	0.20	0.19	0.192	0.179	0.18	0.20
Temperature	754	702	835	798	798	798	786	774	792	779	783	790	809
2 sigma stdev	130	127	165	75	65	79	76	68	165	62	76	79	140
Pressure	8.5	4.4	7.4	8.4	9.9	7.7	7.9	9.3	10.7	10.3	7.6	7.7	9.4
2 sigma st dev	1.3	1.29	1.4	1.35	1.27	1.4	1.35	1.3	1.26	1.23	1.3	1.39	1.31

Interior Pairs

Garnet	4 & 33	3 & 6	7 & 3	8 & 5	9 & 12	10 & 12	11 & 18	13 & 3	25 & 33	29 & 3	30 & 19	36 & 37
SiO_2	39.02	39.2885	39.10	39.05	39.13	39.08	39.01	39.26	39.36	38.84	39.22	39.22
TiO_2	0.03	0.0285	0.02	0.04	0.02	0.02	0.01	0.01	0.03	0.02	0.02	0.03
Al_2O_3	21.75	22.0845	22.00	22.07	21.90	21.89	21.71	21.94	21.92	21.89	21.95	21.89
FeO	33.55	32.7395	32.38	32.30	31.97	31.73	32.01	32.25	33.31	33.06	32.41	33.02
MnO	1.38	1.4935	1.51	1.40	1.41	1.33	1.36	1.45	1.26	1.43	1.34	1.36
MgO	5.27	5.9155	5.84	5.77	5.84	5.79	5.36	5.79	5.57	5.31	5.58	5.76
CaO	1.46	1.401	1.38	1.30	1.37	1.42	1.50	1.36	1.48	1.57	1.73	1.38
Na_2O												
K_2O												
Total	102.47	102.951	102.23	101.94	101.65	101.26	100.96	102.06	102.92	102.12	102.25	102.66
Si	3.02	3.01	3.01	3.02	3.03	3.03	3.04	3.03	3.02	3.01	3.02	3.02
Ti	0.00	0.00	0.00	0.00	0.00	0.00	0.00	0.00	0.00	0.00	0.00	0.00
Al	1.98	1.99	2.00	2.01	2.00	2.00	1.99	1.99	1.98	2.00	1.99	1.98
	1.98	2.00	2.00	2.01	2.00	2.00	2.00	1.99	1.98	2.00	1.99	1.99
Fe	2.17	2.10	2.09	2.09	2.07	2.06	2.09	2.08	2.14	2.14	2.09	2.12
Mn	0.09	0.10	0.10	0.09	0.09	0.09	0.09	0.09	0.08	0.09	0.09	0.09
Mg	0.61	0.68	0.67	0.66	0.67	0.67	0.62	0.66	0.64	0.61	0.64	0.66
Ca	0.12	0.12	0.11	0.11	0.11	0.12	0.12	0.11	0.12	0.13	0.14	0.11
	2.99	2.99	2.97	2.95	2.95	2.93	2.92	2.95	2.98	2.98	2.96	2.99
Mol% Alm	72.61	70.27	70.27	70.74	70.15	70.17	71.33	70.47	71.78	71.93	70.55	71.13
Mol% Pyr	20.33	22.63	22.59	22.50	22.85	22.83	21.32	22.51	21.39	20.55	21.67	22.08
Mol% Sps	3.02	3.25	3.31	3.11	3.14	2.97	3.07	3.20	2.75	3.14	2.96	2.97
Mol% Gro	4.03	3.85	3.84	3.65	3.86	4.03	4.27	3.81	4.07	4.37	4.83	3.82
Fe/(Fe+Mg)	0.78	0.76	0.76	0.76	0.75	0.75	0.77	0.76	0.77	0.78	0.77	0.76
Mg/(Mg+Fe)	0.22	0.24	0.24	0.24	0.25	0.25	0.23	0.24	0.23	0.22	0.23	0.24
Temperature	715	611	603	663	552	677	695	633	688	677	718	662
2 sigma stdev	82	75	75	77	88	76	79	76	80	76	76	85
Pressure	5.7	4.6	4.5	5.2	4.2	5.7	5.5	4.7	5.5	5.7	6.6	4.4
2 sigma st dev	1.31	1.15	1.14	1.25	1.39	1.26	1.25	1.19	1.27	1.24	1.28	1.21

Garnet C Garnet-Biotite-Plagioclase Pairs Compositions

Rim/Matrix pairs

Garnet	1 & 22	2 & 1	3 & 19	11 & 19	12 & 19	18.000	16A & 22*	16B & 19*	20 & 22*	23 & 22*
SiO_2	38.82	38.71	38.47	38.33	38.65	38.86	39.05	38.48	38.85	38.64
TiO_2	0.01	0.00	0.00	0.01	0.01	0.02	0.02	0.00	0.06	0.02
Al_2O_3	21.59	21.68	21.51	21.53	21.65	21.92	21.75	21.61	21.72	21.64
FeO	33.54	34.03	33.86	34.11	33.44	32.46	33.30	33.44	33.34	33.16
MnO	1.05	1.09	1.08	1.03	1.04	1.34	1.10	1.09	1.04	1.07
MgO	4.51	4.67	5.08	4.74	4.98	5.76	4.64	5.05	4.56	4.67
CaO	2.91	2.58	1.84	1.78	1.93	1.58	2.56	1.90	2.63	2.53
Na_2O										
K_2O										
Total	102.43	102.76	101.85	101.53	101.69	101.94	102.42	101.58	102.20	101.73
Si	3.01	3.00	3.00	3.00	3.01	3.007	3.02	3.01	3.02	3.01
Ti	0.00	0.00	0.00	0.00	0.00	0.001	0.00	0.00	0.00	0.00
Al	1.98	1.98	1.98	1.99	1.99	1.999	1.98	1.99	1.99	1.99
	1.98	1.98	1.98	1.99	1.99	2.001	1.99	1.99	1.99	1.99
Fe	2.18	2.21	2.21	2.24	2.18	2.101	2.16	2.18	2.16	2.16
Mn	0.07	0.07	0.07	0.07	0.07	0.088	0.07	0.07	0.07	0.07
Mg	0.52	0.54	0.59	0.55	0.58	0.665	0.54	0.59	0.53	0.54
Ca	0.24	0.21	0.15	0.15	0.16	0.131	0.21	0.16	0.22	0.21
	3.01	3.03	3.03	3.01	2.99	2.984	2.98	3.00	2.98	2.99
Mol% Alm	72.32	72.77	73.02	74.34	72.94	70.4	72.44	72.71	72.64	72.37
Mol% Pyr	17.34	17.80	19.52	18.42	19.38	22.3	18.00	19.58	17.72	18.18
Mol% Sps	2.29	2.36	2.36	2.27	2.29	2.9	2.42	2.40	2.30	2.36
Mol% Gro	8.05	7.07	5.09	4.98	5.39	4.4	7.14	5.31	7.33	7.08
Fe/(Fe+Mg)	0.81	0.80	0.79	0.80	0.79	0.760	0.80	0.79	0.80	0.80
Mg/(Mg+Fe)	0.19	0.20	0.21	0.20	0.21	0.240	0.20	0.21	0.20	0.20
Temperature	776	771	833	856	810	873	741	809	800	786
2 sigma stdev	69	69	79	81	77	85	72	78	72	73
Pressure	8.7	8.9	8.3	8.4	8.2	7.5	7.7	8.1	8.6	8.3
2 sigma st dev	1.27	1.3	1.46	1.5	1.41	1.51	1.24	1.42	1.32	1.3

Interior Pairs

Garnet	4 & 21	5 & 6	7 & 8	7 & 9	5 & 10	7 & 13	7 & 17
SiO_2	38.55	38.83	38.80	38.88	38.85	38.67	38.89
TiO_2	0.02	0.01	0.01	0.01	0.01	0.01	0.01
Al_2O_3	21.99	21.77	22.07	22.05	21.91	21.95	22.19
FeO	33.77	33.43	33.04	32.84	33.27	33.06	32.82
MnO	1.28	1.36	1.40	1.32	1.34	1.26	1.31
MgO	5.31	5.59	5.68	5.47	5.53	5.23	5.53
CaO	1.68	1.56	1.68	1.75	1.61	2.11	1.75
Na_2O							
K_2O							
Total	102.59	102.55	102.69	102.32	102.51	102.29	102.49
Si	2.98	3.00	2.99	3.00	3.00	3.00	3.00
Ti	0.00	0.00	0.00	0.00	0.00	0.00	0.00
Al	2.01	1.98	2.00	2.01	1.99	2.00	2.02
	2.01	1.98	2.01	2.01	1.99	2.00	2.02
Fe	2.19	2.16	2.13	2.12	2.15	2.14	2.12
Mn	0.08	0.09	0.09	0.09	0.09	0.08	0.09
Mg	0.61	0.64	0.65	0.63	0.64	0.60	0.64
Ca	0.14	0.13	0.14	0.15	0.13	0.18	0.14
	3.02	3.02	3.01	2.98	3.01	3.00	2.98
Mol% Alm	72.34	71.48	70.68	71.14	71.48	71.30	70.97
Mol% Pyr	20.29	21.30	21.67	21.11	21.18	20.12	21.33
Mol% Sps	2.77	2.95	3.03	2.88	2.91	2.74	2.86
Mol% Gro	4.60	4.28	4.62	4.87	4.43	5.84	4.84
Fe/(Fe+Mg)	0.78	0.77	0.77	0.77	0.77	0.78	0.77
Mg/(Mg+Fe)	0.22	0.23	0.23	0.23	0.23	0.22	0.23
Temperature	701	666	604	593	667	577	597
2 sigma stdev	76	77	73	71	78	69	71
Pressure	6.3	5.4	4.3	4.6	5.1	4.7	4.7
2 sigma st dev	1.26	1.2	1.1	1.08	1.2	1.04	1.09

Garnet D

Interior Pairs

Garnet	3 & 4	5 & 6	7 & 8
SiO_2	38.45	38.61	38.56
TiO_2	0.04	0.01	0.01
Al_2O_3	21.80	21.83	21.91
FeO	33.76	33.13	33.59
MnO	1.17	1.31	1.11
MgO	5.17	5.79	5.35
CaO	1.48	1.31	1.84
Na_2O			
K_2O			
Total	101.86	102.00	102.35
Si	2.9957	3.00	2.99
Ti	0.0026	0.00	0.00
Al	2.0018	2.00	2.00
	2.0043	2.00	2.00
Fe	2.1997	2.15	2.18
Mn	0.0772	0.09	0.07
Mg	0.6005	0.67	0.62
Ca	0.1233	0.11	0.15
	3.0007	3.01	3.02
Mol% Alm	73.309	71.31	72.07
Mol% Pyr	20.011	22.20	20.45
Mol% Sps	2.5737	2.86	2.41
Mol% Gro	4.107	3.63	5.07
Fe/(Fe+Mg)	0.7856	0.76	0.78
Mg/(Mg+Fe)	0.2144	0.24	0.22
Temperature	604	650	666
2 sigma stdev	76	79	74
Pressure	4.2	4.5	5.7
2 sigma st dev	1.12	1.21	1.17

Appendix B.

Supplementary Information to Chapter 3

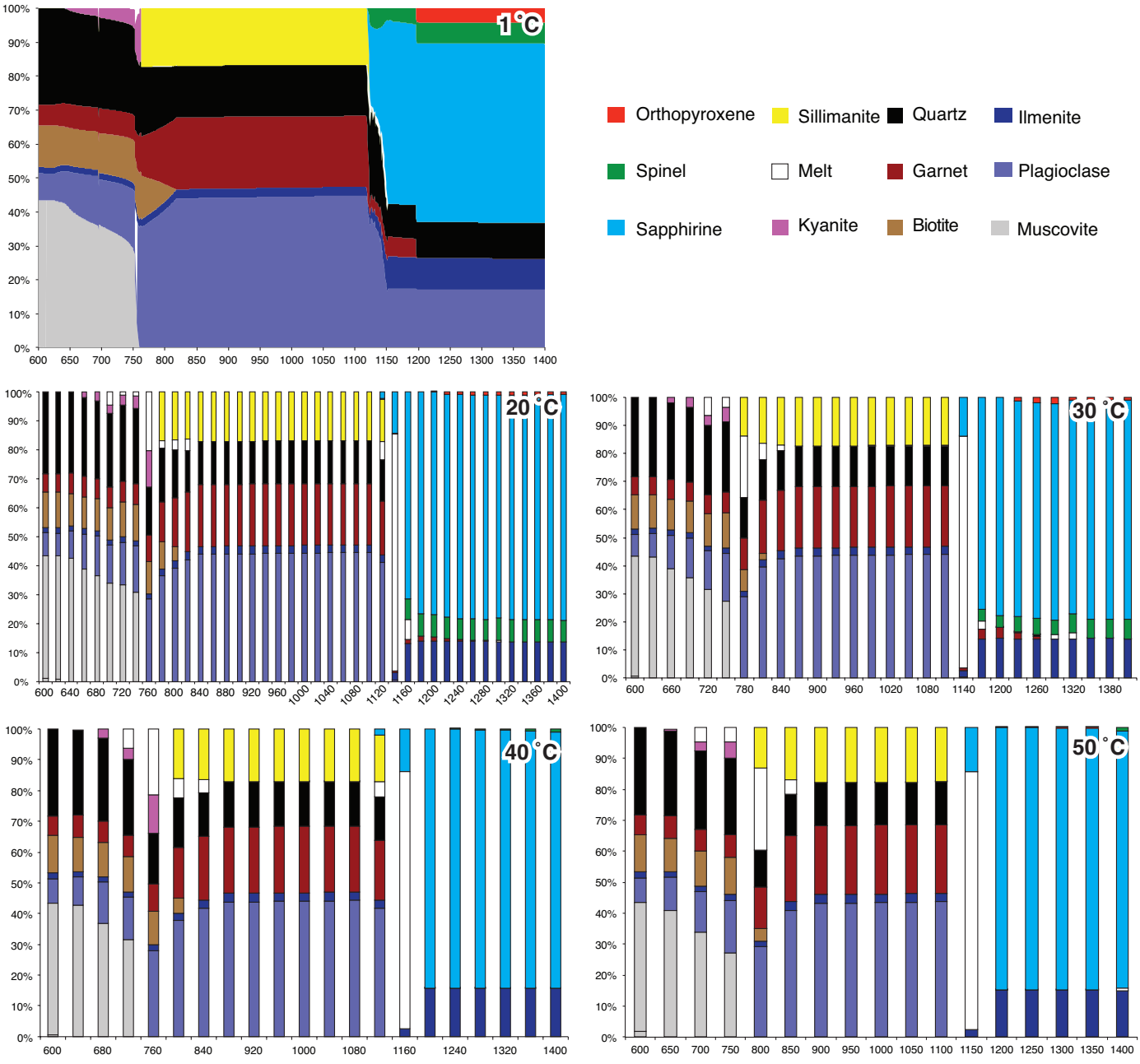

Figure B1. 1 ˚C, 20 ˚C, 30˚C, 40 ˚C and 50 ˚C batch-melting model

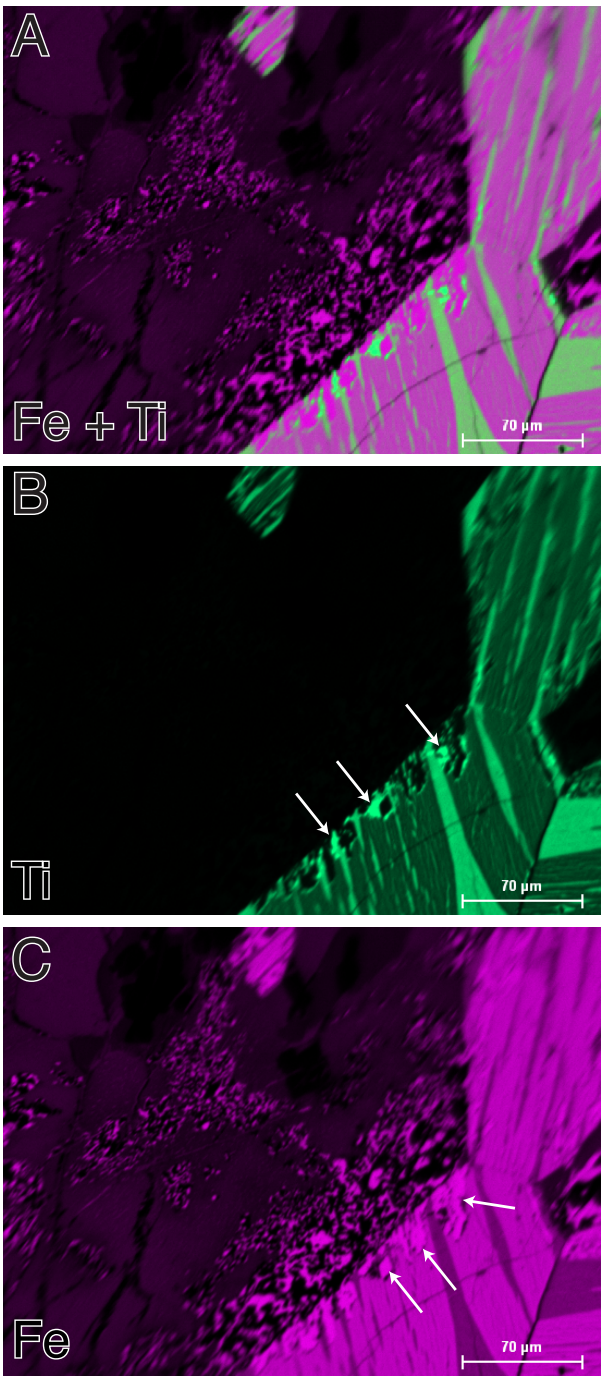

Figure B2. Three panels of an area in SH24 showing the symplectites (middle of the image) and adjacent ilmeno-hematite exsolving to rutile + magnetite. Panel (a) is an EDS chemical map overlay of Fe (pink) and Ti (green). Arrows in panel (b) indicate areas of pure TiO_2. Arrows in panel (c) point to areas of pure Fe_3O_4 in the ilmeno-hematite.